Numerical and Experimental Studies of Available Energy Losses in Laminar and Turbulent Flows

by

Olusola Babatunde Adeyinka

A thesis presented to

The University of Manitoba

in partial fulfillment of the requirement for the degree of

Doctor of Philosophy

in Mechanical Engineering

Department of Mechanical and Manufacturing Engineering

Winnipeg, Manitoba, Canada

THE UNIVERSITY OF MANITOBA

FACULTY OF GRADUATE STUDIES

*****

COPYRIGHT PERMISSION

"Numerical and Experimental Studies of Available Energy Losses in Laminar and Turbulent Flows"

BY

Olusola Babatunde Adeyinka

A Thesis/Practicum submitted to the Faculty of Graduate Studies of The University of Manitoba in partial fulfillment of the requirement of the degree

Of

DOCTOR OF PHILOSOPHY

Acknowledgements

I am indebted to many people who have contributed and made this thesis possible.

My supervisor, Dr. G. F Naterer, for his support, constant encouragement and guidance. His expert advice on the Second Law greatly benefited me in the course of this study.

The members of my advisory committee, Dr. D. Fraser and Dr. D. Svecova for their useful feedback in the course of this work. Also, Dr. LoVetri for serving on my examination committee.

My friends and colleagues, Emmanuel Ogedengbe and Stephen Glockner for their helpful discussion throughout my studies.

This work was partly supported by a research grant from the Natural Sciences and Engineering Research Council of Canada to my supervisor. The financial support of the University of Manitoba through the Graduate Fellowship, conference travel awards, and the Edward Toropek Scholarship is gratefully acknowledged.

Finally, my deepest appreciation and love is extended to my wife, Wuraola, for her love and support through another three years of university studies.

This thesis is dedicated to my daughter, Oreoluwa.

Abstract

A new experimental technique is developed for measuring the instantaneous entropy production using a non-intrusive laser based approach. The experimental procedure combines the method of Planar Laser Induced Fluorescence (PLIF) and Particle Image Velocimetry (PIV) for measured velocity and temperature fields in different applications. Unlike pointwise methods which yield a measured velocity at a single point in space, the method of PIV is used to derive velocity gradients over the entire problem domain. When combined with local temperatures and thermal irreversibilities, these velocity results can be used to determine the energy availability loss due to exergy destruction. The local entropy production data provides useful information regarding the spatial distribution of mechanical energy loss, which can be used to systematically optimize thermofluid systems. The measured data also provides validation for previous predictive models. Local entropy production rates due to fluid friction are determined from an experimental study of laminar and turbulent flow in a channel, as well as natural convection in an enclosure.

An entropy-based conversion algorithm in the measurement procedure is developed and compared with numerical predictions of free convection in a square cavity. The numerical predictions are obtained from a Control-Volume Based Finite Element Method (CVFEM) for the conservation equations and the Second Law. Analytical and direct numerical solutions are employed for a qualitative assessment of the experimental procedure in the channel flow problem. The predicted and measured results show close agreement. For the free convection problem, a measurement uncertainty analysis suggests that the algorithm post-processes velocity (accurate within $\pm$ 0.5%) to successfully give entropy production data, which is accurate within $\pm$ 9.34%. Extensions of the loss mapping technique to turbulent flow engendered a new model

for a turbulence correlation in the entropy transport equation of viscous, incompressible flow. Additional terms were introduced into the entropy production relation in the conversion algorithm, due to the dissipation of turbulent kinetic energy. Previous methods of measuring dissipation rate are outlined in the context of the PIV technique.

Contents

List of Figures

List of Tables

Nomenclature

A	cross-sectional area (m^2)
B	bias error
c_p, c_v	specific heats (J/kgK)
C	concentration (g/L)
f	friction factor
F	entropy flux (W/m^2K)
F_b	body force (N)
g	gravity acceleration (m/s^2)
h_l	head loss (m)
I	fluorescence intensity (cd)
k	thermal conductivity (W/mK)
L	length (m)
L_o	width of camera view (m)
L_I	width of digital image $(pixel)$
M	camera magnification
N	shape functions, number of images
p	pressure (Pa)
P	precision error
Pr	Prandtl Number (ν/α)
$\dot{P}_s$	entropy production rate (W/m^3K)
q	heat flux (W/m^2)

Ra	Rayleigh number ($g\beta\Delta TL^3/\nu\alpha$)
Re_τ	Reynolds number based on friction velocity
Re_D	Reynolds number based on hydraulic diameter
s	specific entropy (kJ/kg K)
S	control surface or source term
Δt	time step (s)
t	time (s), confidence coefficient
T	temperature (K)
u, v	components of velocity (m/s)
u_τ	friction velocity (m/s)
x, y	cartesian coordinates (m)
$\forall$, $\mathcal{V}$	volume

Greek Letters

α	thermal diffusivity (m^2/s)
β	expansion coefficient ($1/K$)
Δ	interrogation width (m)
γ	specific heat ratio
Γ	diffusion coefficient
δ	Kronecker delta
ϵ	turbulence dissipation rate $\times$ density ($\rho\varepsilon$, W/m^3)
ε	turbulence dissipation rate (m^2/s^2)
η	sensitivity coefficient or Kolmogorov length scale (m)
μ	dynamic viscosity (kg/ms)
ν	kinematic viscosity (m^2/s)
ρ	density (kg/m^3)
τ_{ij}	stress tensor
ϕ	general scalar quantity
Φ	integration point value of scalar
ω	vorticity

Subscripts

i, j, k	coordinate directions (tensor notation)
d	downstream point
SGS	sub-grid scale
u	upstream point

Superscripts

$(\,)^+$	normalized by the wall variables
$(\,)'$	fluctuating quantity (turbulence notation)
ip	integration point

Chapter 1

Introduction

Considerable recent attention to energy efficiency has been motivated by an increased awareness that the world's energy and environmental resources are limited. Major efforts have focused on the design of highly efficient energy devices and more environmentally friendly processes. Thermal and mechanical energy systems have been thoroughly scrutinized for possible design improvements. Past conventional technology has generally detected energy losses on a system-wide or global scale, such as a single loss coefficient (i.e., valve loss coefficient). With the current state of this technology, the margins of improving efficiency of existing devices can be relatively small. However, recent advances in entropy-based design with local loss mapping offer a useful new way of reaching higher levels of system efficiency, thereby leading to energy savings in various industrial applications.

1.1 Motivation

The fundamental principles governing the design of thermo - fluid systems are Newton's law of motion and the laws of thermodynamics. In fact, Newton's Second Law of motion and the First Law of Thermodynamics are the cornerstones upon which virtually all energy systems are built today. The other laws have a supporting role.

Unlike the First Law of Thermodynamics, which tracks only the quantity of energy, the Second Law of Thermodynamics tracks quality of energy or its work-producing potential. Thus, the Second Law has the unique advantage of offering an excellent guideline in the pursuit of optimal energy usage and choice of technologies. The unique capabilities of the Second Law in this thesis focus on measuring the flow irreversibilities locally, rather than globally. In this way, the problem region(s) can be clearly identified from the high entropy production rates, so designers could focus on those regions for improvements. A useful analogy is a sick patient telling a doctor that he / she is sick, without knowing the part of the body that is causing the ailment. Similarly for a complex engineering system, large rates of entropy production within a device would identify areas of concern, since a commonly desired goal of devices is improving efficiency through reduced entropy production. This goal is generally desired, regardless of application, flow conditions, system parameters, and so on.

Alternatively, local exergy or the work potential of a device can be more readily interpreted physically, as it contains the same dimensional units as energy. It can be related directly to economic indicators. For example, multiplying the local cost of electricity (per kWhr) by exergy destroyed in moving fluid through a valve over a year can indicate a yearly expense of wasted energy therein. This expense can be interpreted in terms of lost revenue. Thus, an economic framework can be based on the measurement of local entropy production.

Furthermore, there is a need for a standard metric, from which the energy efficiency of all devices is characterized. For example, fuel efficiency in a car is defined differently than a water heater's efficiency, while still different than how a diffuser's efficiency is defined, and so on. As a result, it is difficult for regulatory and government agencies to identify a standard way of identifying any device's energy wastefulness. Entropy production provides a single, measurable quantity that is directly related to

the efficiency of any energy consuming device, since it characterizes degradation of useful (mechanical) energy to less useful (internal) energy.

1.2 Literature Review

From engineering fluid mechanics, to information / coding theory, economics and biology, the various applications of entropy are widespread. Exergy serves as a key parameter in achieving the upper limits of performance and quality in many engineering technologies. It can shed new light on various flow processes, ranging from optimized flow configurations in an aircraft engine, to highly ordered crystal structures (low entropy) in a turbine blade, and other applications [1, 2]. It is likely not possible to find any other law of nature, whereby a proposed violation would bring more skepticism than violation of the Second Law.

An important application of entropy is the optimized flow design of aircraft sub-systems, involving work potential [3]. It appears that there is no systematic method for tracking work potential usage in the design of aircraft sub-systems [4]. Exergy and entropy calculations can identify the loss of work potential within each sub-system and fluid flow process during an aircraft's operation. This would provide the designer with a systematic way of identifying and targeting those areas incurring the most significant losses. In this way, economic considerations could be directly linked to work potential and flow irreversibilities. Moorhouse and Suchomel [5] suggest that flow exergy provides a unifying framework and a set of metrics to more effectively analyze aircraft sub-systems.

Another important application of flow irreversibilities arises with effective thermal management of electronic devices. Optimized convective cooling of microelectronic assemblies has received considerable past attention. The effects of component layout

on flow patterns in such assemblies were investigated in a water tunnel [6]. Entropy generation has been used to find the minimum power input for convective cooling of an electronic package [7]. The minimization is carried out with respect to the coolant flow rate and heat transfer contact area. Landauer [8] outlines how the ultimate physical limitations on faster and more compact microelectronic circuits are considered to be directly linked to the Second Law.

1.2.1 Analytical Methods

The past decade has seen important progress towards the optimization of fluid, thermal and energy systems using the Second Law of Thermodynamics. This progress includes an analytical approach, which has been performed previously with various techniques, i.e., (i) estimation of the theoretical ideal operating conditions of a proposed design (called EA; Exergy Analysis), (ii) minimization of the lost available work or entropy generation by design modifications (called EGM; Entropy Generation Minimization) [9]. Exergy is a thermodynamic property that quantifies the capacity of an energy source to perform useful work. It is a measure of the maximum capacity of an energy system to perform useful work as it proceeds to a specified final state in equilibrium with its surroundings. Exergy analysis focuses on closing the gap between exergy and the actual work being delivered by a device through a careful examination of the thermodynamic processes involved in a series of energy conversion steps. Subsequently, the exergy values at each point are used to evaluate Second Law efficiencies which quantify the magnitude of irreversibilities (or exergy destruction) associated with the energy conversion process [9, 10, 11]. EGM may require the use of fluid mechanics, heat transfer, material constraints and geometry in order to obtain relationships between entropy generation and the optimal configuration. Typically, a functional expression for the entropy production in a process is derived [2, 12, 13, 14].

Then, the turning point or extremum of the derived expression that guarantees a minimum entropy production is determined by differentiation. Since analytical methods are typically limited to simplified geometries, this thesis focuses on numerical and experimental methods.

1.2.2 Numerical Methods

Additional opportunities for design optimization using the Second Law can be realized by fully incorporating Computational Fluid Dynamics (CFD) as a design tool for more complex problems. Entropy production is then obtained by post-processing of the predicted flow fields [15]. Many industrial problems arising in metallurgy, power generation, energy storage, aerodynamics and other applications have been successfully solved by CFD. A designer can choose an optimum design from many possible alternatives at a remarkable speed using CFD. Local EGM with numerical methods provides extra flexibility, in terms of problem geometry.

For example, an application involving the design of air-cooled gas turbine blades is presented by Natalini and Sciubba [16]. The full Navier-Stokes equations of motion for turbulent viscous flow and the energy equations are solved with a finite element approach and $k-\epsilon$ closure. By identifying the entropy generation rates corresponding to the fluid friction and heat transfer effects, the authors provided useful information for the assessment of different blade configurations with minimal thermodynamic loss in a turbine cascade. The computed flow field produced by pitched turbine blades [17] could be post-processed to identify regions of high local losses, thereby guiding engineers in local re-design of the blade profile to reduce such losses. Predictions of entropy production have also been applied to find the optimal inclination angle for an application involving natural convection in inclined enclosures [18]. Other numerical procedures predicted entropy generation for mixed convection in a vertical channel

with transverse fin arrays [19], laminar and turbulent flow through a smooth duct [20, 21, 22], flow in concentric cylinder annuli with relative rotation [23] and diffuser geometries [24]. These represent examples of how entropy production computations can successfully complement standard CFD solvers.

1.2.3 Turbulent Flows

Turbulent flows are often more complex than applications mentioned previously. Numerical predictions of entropy production in a turbulent boundary layer were presented by Moore and Moore [25]. Moores' work appears to be the first documented effort to develop a numerical model for entropy production. The Moore model assumes that turbulent fluctuations of the heat flux and viscous dissipation in the positive definite entropy equation can be modelled by adding a turbulent conductivity and turbulent viscosity to the molecular conductivity and viscosity, respectively. The Moore model has been applied for the mean entropy production in a turbulent flow. In particular, the model has been used to predict the mean local entropy production in a bent elbow [26], turbulent plane oscillating jet [27], and a jet impinging on a wall [28]. A finite volume method for predicting the mean viscous dissipation and entropy production in turbulent flows, based on time-averaged turbulence equations was described by Kramer-Bevan [29]. The closure of the entropy equations was based on a small thermal turbulence model. Despite these advances, further work is needed to develop a generally accepted model for entropy production in turbulent flows.

1.2.4 Mathematical Entropy Analysis

The traditional physical characteristics of entropy production can also be interpreted alternatively in computational terms. In addition to physical processes of viscous dissipation and heat transfer, recent advances in Second Law analysis have identified

that numerical procedures may also produce or destroy entropy due to discretization errors, artificial dissipation and non-physical numerical results [30, 31]. Solutions of differential equations which do not satisfy an 'entropy condition' may be characterized by a lack of uniqueness, oscillations, and other unusual behaviour [32]. Thus, the Second Law offers a stability criterion in finite element methods [33]. Cox and Argrow [31] computed local entropy production with a finite difference method for compressible flow. Jansen [34] and Hauke [35] have extended entropy-based stability analysis to turbulent flows. Jansen showed that the exact Navier-Stokes equations for compressible flow could lead to an entropy inequality, through a linear combination of equations [34]. The study determined what constraints the Second Law places on the modeling of the averaged equations by linking entropy production to their solution variables. A detailed review of past advances regarding entropy and the Second Law in CFD has been presented by Naterer and Camberos [36].

1.2.5 Experimental Methods

For complex geometries, analytical results are generally not available, so numerical and experimental methods are needed. A major difficulty with numerical predictions can be the inability to ascertain error bounds. Solutions can be very sensitive to various parameters associated with the numerical algorithm [30]. This can make it difficult to judge the extent to which the computed results agree with reality. Thus, experimental data is generally required to validate the numerical codes and to ascertain that the physics of a problem has been modeled correctly.

In recent studies, Adeyinka and Naterer [32, 37] proposed that post-processing of the spatial velocity gradients characterizes the flow irreversibilities, while establishing entropy production as a derived experimental quantity. Past experimental Particle Image Velocimetry (PIV) and Planar Laser Induced Fluorescence (PLIF) studies have

been reported for whole-field measurements of velocity and temperature of water in free convection [38, 39]. Although PIV and PLIF techniques are conventional experimental techniques, their application to entropy production analysis has not been developed previously (to my knowledge). Unlike velocity or temperature, the measurement of entropy production cannot be performed directly, so new algorithms for experimental post-processing of measured quantities are needed. This thesis develops a new post-processing algorithm for these purposes.

1.3 Problem Definition and Objectives

The major results of the literature search that define the problems addressed in this thesis are summarized as follows:

- *There is need for a component level local design methodology based on the Second Law of Thermodynamics.* Traditionally, energy system designers evaluate performance and quality of a design by global loss parameters or efficiencies. This approach accounts for losses computed over an entire system. However, it is viewed that the information provided to the designer by local values of entropy production or energy availability loss is more valuable than examining the end-to-end loss, since the desired overall performance of engineering systems can be improved by modifying design variables locally.

- *An experimental technique for entropy production measurement has not been previously developed.* For complex geometries, analytical results are not generally available and we rely on numerical or experimental methods. A few past numerical studies have calculated entropy production for local loss predictions. But a literature search identified no previous documented effort regarding experimental local losses and entropy production.

- *There is no generally accepted model for turbulent entropy production.* As discussed previously, the Moore model is widely used in CFD [25]. However, Kramer-Bevan [29] has shown that the Moore model exhibits certain inconsistencies for confined flows with small temperature gradients close to the wall, where the production of turbulent kinetic energy is not equal to the dissipation of turbulent kinetic energy. Furthermore, other assumptions lead to difficulties when generalizing the formulation. For example, the model assumes that the production of temperature fluctuations is equal to their dissipation. Also, the viscous dissipation fluctuation is assumed to be equal to the production of turbulent kinetic energy. In this thesis, these shortcomings are addressed through revised modeling of the turbulence correlations in the entropy equations. The viscous dissipation term may be neglected in the energy equation when computing the mean entropy generation based on the Moore model [25], as the evaluation depends on the velocity and temperature fields. Under certain flow conditions, previous studies have shown that CFD codes can accurately predict velocity and temperature fields when viscous dissipation is neglected [1]. However, the viscous dissipation cannot be generally neglected when using the STTAss (Small Thermal Turbulence Assumption; [29]). In the STTAss model, it is assumed that the fluctuating component of temperature is small compared to the mean temperature, so the fluctuating temperature in the entropy transport equation can be simplified with Taylor series expansions. Those expansions are truncated after the linear terms, thereby yielding a reduced form of mean entropy production equation. But the spatial variation of fluctuating temperature is required to accurately account for the convection of entropy in the flow. It has been shown that the transport equation model becomes inaccurate for laminar flow in the center of an adiabatic duct, where small temperature

gradients may cause a cancellation [29].

Therefore, the objectives of this thesis are given as follows:

- *Demonstrate a new experimental technique for entropy production with heat transfer and laminar fluid flow.* In order to validate the experimental technique, two test problems will be studied. The first case involves flow in a parallel channel. A more complex flow involving internal flow in a cavity will be studied in the second case. The primary aim of the experimental study is to evaluate the feasibility of using PIV/PLIF for entropy production measurement. It is remarkable that the technique will be shown to give reliable results and an accurate distribution of flow losses throughout the range of test problems. In some cases, the results are supported by numerical simulations which compliment the experimental procedure. The numerical solution also serves as a qualitative reference for the measured entropy production fields.

- *Extend the new measurement technique to turbulent flows.* Application of the measurement technique in the experiments was initially limited to laminar flows. Many flows of interest to engineers contain regions where the effect of turbulence is quite significant. This objective engendered the extension of classical Reynolds averaging techniques for the momentum and scalar transport equations to the Second Law for turbulent flows. The extension of the measurement technique to turbulent flows introduces additional terms into the entropy production equation and conversion algorithm, due to the dissipation of turbulent kinetic energy.

- *Develop a working model of an entropy production conversion algorithm.* A working model of the conversion algorithm will be standardized by interactive

software incorporated into an existing industrial code (FlowManager; Dantec Dynamics [47]). Application of the proposed technique will be demonstrated for flows in ducts and cavities.

- *Extend past Reynolds averaging techniques for the conservation equations to the Second Law for turbulent flows.* The formulation requires instantaneous values of the velocity and temperature fields. In order to express the mean entropy generation explicitly in terms of other mean flow quantities, a closure problem is encountered, similarly as the evaluation of Reynolds stresses in the momentum equations. To my knowledge, there are no existing empirical / numerical Second Law closure models based fully on mean quantities from the conservation equations. This thesis addresses this shortcoming, while developing an alternative closure. In particular, a new entropy-temperature correlation will be developed that incorporates the effect of temperature fluctuating stress interactions in the modeling of the mean entropy production. New complete closure models will be formulated based on the new correlation and the STTAss. Furthermore, this thesis proposes an alternative interpretation and model for the dissipation of turbulent kinetic energy, based on the Second Law.

The entropy production results will be compared with analytical and numerical results where applicable. The uncertainty of measured data will be presented. The final results represent the first documented study (to my knowledge) of measured entropy production in fluid flow and heat transfer processes with non-intrusive laser based techniques.

For all the analyses in this thesis, it shall be assumed that the continuum assumption is valid, the mass of the system is conserved and does not change (no nuclear reactions), and radiative and magnetic effects are negligible.

1.4 Outline of Thesis

This thesis outlines new numerical and experimental methods for thermal design and loss analysis using the Second Law of Thermodynamics. Detailed numerical simulations of the fluid flow, energy and entropy transport equations will be performed with a Control-Volume Finite Element Method (CVFEM). Also, a new experimental technique based on combined Particle Image Velocimetry (PIV) and Planar Laser Induced Fluorescence (PLIF) will be presented for energy loss detection in energy systems. Applications to loss characterization in various applications will be presented, i.e., flow in parallel ducts and free convective heat transfer. In these applications and others, the technique will be shown to give promising performance, reliable new data and an accurate new description of flow losses and energy conversion through entropy production.

In Chapter 2, a generalized formulation for entropy production and its relation to losses of mechanical energy will be presented. Chapter 3 outlines the experimental technique and its underlying principle. Detailed information regarding the estimation of the dissipation of turbulent kinetic energy will be presented for turbulent flow applications. An application of the measurement technique to flow between parallel plates will be discussed in Chapter 4. Free convective heat transfer is examined in Chapter 5, with comparisons to previous numerical benchmark solutions, as well as new numerical results. Chapter 6 presents a measurement uncertainty analysis for the laminar flow cases. The last chapter concludes the thesis with a general discussion and suggestions for further research.

Chapter 2

Loss Characterization and Second Law Modelling

In this chapter, the equations describing the Second Law and its modelling in both laminar and turbulent flows will be discussed. The formulation specifically considers incompressible forced convection problems without a buoyancy term in the y-momentum equation, as density variations are neglected. A newtonian fluid with constant thermophysical properties is assumed in the modeling of the diffusion terms in the momentum equations while the Fourier law will be applied in the energy equations. In formulating the final turbulence closure models, a small thermal turbulence was assumption was used. This chapter will also present the numerical formulation with the geometrical discretization and the local-global coordinate transformation, which is required to apply the conservation laws to discrete control volumes and finite elements. The chapter concludes with an outline of the method used to express the discrete form of the Second Law.

2.1 General Scalar Conservation Equation

In tensor notation, the conservation form of the scalar equation in multi-dimensions can be written as [1]

$$\frac{\partial(\rho\phi)}{\partial t} + \frac{\partial}{\partial x_j}(\rho u_j \phi) = -\frac{\partial}{\partial x_j}(\Gamma \frac{\partial \phi}{\partial x_j}) + S_\phi \tag{2.1}$$

where $j = 1, 2, 3$ and ϕ is a general scalar quantity or dependent variable, such as concentration, temperature, velocity, etc., transported throughout the flow field by diffusion or convection. The terms on the left-hand side of Eq. (2.1) represent the transient storage term and the convective flux. The first term on the right hand side is the diffusive flux. The last term represents internal or external production / sources of ϕ in the volume. In the modelling of Eq. (2.1), Γ and S_ϕ are generalized properties representing the diffusion coefficient and source terms, respectively. For example, Γ may refer to conductivity, viscosity, eddy diffusivity, etc. depending on the conserved quantity under consideration. Also, terms that cannot be expressed through the convection and diffusion terms (such as the pressure gradient in the momentum equations) can be lumped into the source term.

Assuming incompressibility and constant thermophysical properties, the corresponding governing equations for the conservation of mass, momentum and energy can be written in a form similar to Eq. (2.1), i.e.

$$\frac{\partial}{\partial x_i}(\rho u_i) = 0 \tag{2.2}$$

$$\frac{\partial}{\partial t}(\rho u_i) + \frac{\partial}{\partial x_j}(\rho u_j u_i) = -\frac{\partial p}{\partial x_i} + \frac{\partial}{\partial x_j}\left[\mu\left(\frac{\partial u_i}{\partial x_j} + \frac{\partial u_j}{\partial x_i}\right)\right] + S_{u_i} \tag{2.3}$$

$$\frac{\partial}{\partial t}(\rho\phi) + \frac{\partial}{\partial x_j}(\rho u_j \phi) = \frac{\partial}{\partial x_j}\left(\Gamma \frac{\partial \phi}{\partial x_j}\right) + S_\phi \tag{2.4}$$

These conservation equations involve equalities, whereas the Second Law in the upcoming sections involves an inequality.

2.2 Formulation of Entropy Production

In tensor form, the entropy balance for an open system, subject to mass fluxes and energy transfer across a fixed control surface, may be written as

$$\frac{\partial S}{\partial t} + \frac{\partial F_i}{\partial x_i} \equiv \dot{P}_s \geq 0 \tag{2.5}$$

where $\dot{P}_s$ is the entropy production rate and $S = \rho s$ represents the entropy per unit volume. Also, the component of the entropy flux in the x_i direction, F_i, may be expressed in terms of the velocity component and heat flux in that direction, v_i and q_i, as follows,

$$F_i = \rho u_i s + \frac{q_i}{T} \tag{2.6}$$

Equation (2.5) represents the entropy transport equation. In this form, the rate of entropy accumulation in the control volume is balanced by the net convection of entropy, entropy transfer associated with heat flow and non-negative entropy production. Unlike the conservation of energy equation, the entropy transport equation involves an inequality, which stipulates that the rate of entropy generation must be non-negative in all thermodynamic systems.

The specific entropy, s, in the flux term of Eq. (2.5) can be obtained from the Gibbs equation as follows,

$$ds = \frac{1}{T} de + \frac{p}{\rho^2 T} d\rho \tag{2.7}$$

where e is the internal energy per unit mass, ρ represents density and p is pressure. Integration of the Gibbs equation gives

$$\Delta s = \int_{T_r}^{T_s} c_v \frac{dT}{T} + \int_{\rho_r}^{\rho_s} \frac{p}{\rho^2 T} d\rho \tag{2.8}$$

where the subscripts r and s denote a specified initial (or reference) state and the current state, respectively. The variable c_v represents the specific heat at constant

volume, which will be assumed to be constant. The impact of this constant specific volume assumption implies that the formulation is limited to liquid flows or incompressible gas flows over small to moderate temperature ranges [1]. This assumption applies to explicit evaluation of entropy in the entropy equation of state, but not upcoming transport equations for evaluating spatial variations of the entropy production rate.

For an incompressible fluid, Eq. (2.8) becomes

$$\Delta s = s - s_r = c_v ln\left(\frac{T_s}{T_r}\right) \tag{2.9}$$

For an ideal gas,

$$s = c_v ln\left(\frac{T_s}{T_r}\right) - Rln\left(\frac{\rho_s}{\rho_r}\right) + s_r \tag{2.10}$$

Substituting the ideal gas law into Eq. (2.10),

$$s = c_v ln\frac{(p_s/p_r)}{(\rho_s/\rho_r)^\gamma} + s_r = c_v ln\left(\frac{p^*}{\rho^{*\gamma}}\right) + s_r \tag{2.11}$$

where γ is the ratio of specific heats.

When combined with the Gibbs equation, the entropy transport equation provides a way of calculating the local entropy generation for an open system. Alternatively, $\dot{P}_s$ can be formulated as [2]

$$\dot{P}_s = \frac{k}{T^2}\left(\frac{\partial T}{\partial x_i}\right)^2 + \frac{\tau_{ij}}{T}\frac{\partial u_i}{\partial x_j} \geq 0 \tag{2.12}$$

where k is the thermal conductivity. Also, τ_{ij} is the viscous stress arising from velocity gradients in the fluid motion, i.e.,

$$\tau_{ij} = \mu\left[\left(\frac{\partial u_i}{\partial x_j} + \frac{\partial u_j}{\partial x_i}\right) - \frac{2}{3}\frac{\partial u_k}{\partial x_k}\delta_{ij}\right] \tag{2.13}$$

In Eq. (2.13), μ and δ_{ij} refer to dynamic viscosity and Kronecker delta, respectively. The divergence terms in Eq. (2.13) will vanish due to the assumption of flow incompressibility.

In Eq. (2.12), Fourier's Law has been used to represent heat conduction. Also, a Newtonian fluid is assumed for the viscous stress term. Based on these models, Eq. (2.12) becomes a positive definite expression for the entropy generation rate, since it represents a sum of squared terms [1]. Temperature, T, is expressed in absolute (Kelvin) units. The positive definite equation applies to both compressible and incompressible Newtonian fluids. In Eq. (2.12), the first term on the right side represents entropy generation due to heat transfer across a finite temperature difference, while the second term represents the local entropy generation due to viscous dissipation (i.e., degradation of mechanical energy into internal energy due to shear action).

2.3 Flow Loss Characterization and Exergy Destruction

Conventional loss parameters, such as a global head loss or pressure recovery coefficient, cannot identify specific locations and sources of flow losses in fluid systems. This section presents a formulation that allows local irreversibilities to be scrutinized and converted to local distributions of loss coefficient. In this way, a designer could use local loss mapping to detect locations of high entropy production (or flow irreversibility), thereby allowing local design changes of geometrical or other parameters. In this section, it will be shown that local rates of entropy production can be converted to local loss parameters, while providing a more generalized approach to loss analysis.

Consider incompressible viscous flow through a streamtube in the flow direction, between an inlet (subscript 1) and outlet (subscript 2; see Fig 2.1). The well-known Bernoulli's equation outlines the head loss along this flow path as follows,

$$\frac{p_1}{\rho_1} + gz_1 + \frac{1}{2}V_1^2 = \frac{p_2}{\rho_2} + gz_2 + \frac{1}{2}V_2^2 + h_l \tag{2.14}$$

where h_l is the head loss. Also, p, g, z and V refer to pressure, gravitational acceleration, elevation and total velocity, respectively. It can be shown that Bernoulli's equation represents an integrated form of the following differential mechanical energy equation [1],

$$\rho\frac{D}{Dt}\left(\frac{1}{2}V^2\right) = -\mathbf{v}\cdot\nabla p + \{\nabla\cdot\tau\cdot\mathbf{v} - \tau:\nabla\mathbf{v}\} + \mathbf{F_b}\cdot\mathbf{v} \tag{2.15}$$

where D/Dt, τ, $\mathbf{F}_b$ and $\mathbf{v}$ refer to total (substantial) derivative, shear stress tensor, body force and fluid velocity vector, respectively. The colon symbol (:) represents matrix contraction between the shear stress and velocity gradient matrices. The temporal portion of the substantial derivative on the left side vanishes for steady state conditions.

The previous equation requires that the net convection of kinetic energy (first term) balances the sum of flow work (second term), net work of viscous stresses (third term), plus the net work done by body forces to increase kinetic energy (fifth term), minus the viscous dissipation (fourth term). Re-writing the gravitational body force term, integrating over a streamtube control volume, $\mathcal{V}$, and expressing the vector gradient in the streamwise direction, s,

$$\int_{\mathcal{V}} \rho V\frac{\partial}{\partial s}\left(\frac{1}{2}V^2 + \frac{p}{\rho} + gz\right)d\mathcal{V} = \int_{\mathcal{V}} \nabla\cdot\tau\cdot\mathbf{v}\; d\mathcal{V} - \int_{\mathcal{V}} \tau:\nabla\mathbf{v}\; d\mathcal{V} \tag{2.16}$$

The net viscous work term (first term on right side) is the work done by viscous stresses in the fluid element against the surroundings to change the kinetic energy of the fluid.

More specifically, consider a control volume, $A(ds)$ of finite width in the cross-stream direction and differential length in the streamwise direction (see Fig 2.1).

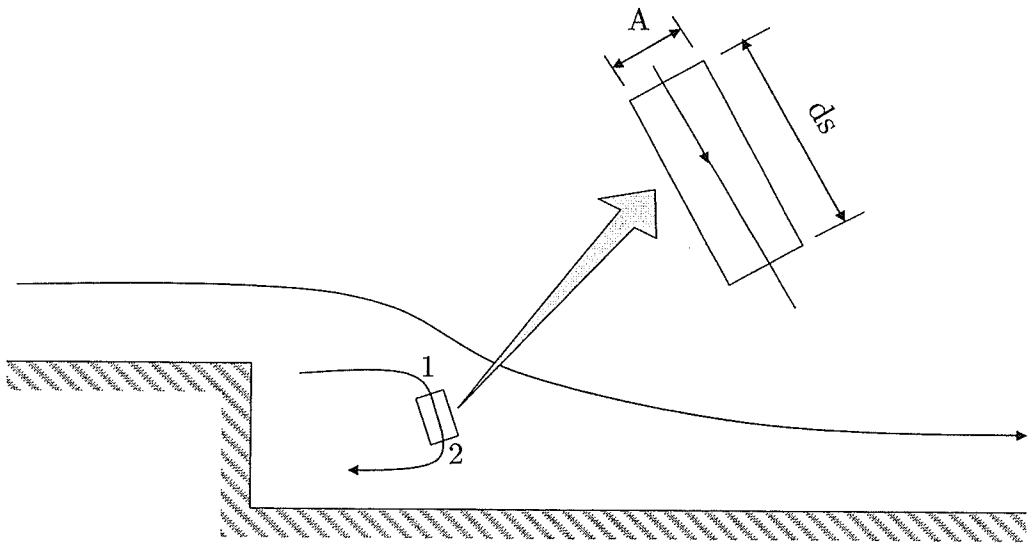

Figure 2.1: Loss in Fluid Flow

Integrating over this control volume and assuming a uniform mass flow rate through the streamtube encompassing the control volume, it can be shown that

$$\frac{\dot{m}}{\dot{m}_R}\int_1^2 d\left(\frac{1}{2}V^2+\frac{P}{\rho}+gz\right)=\frac{1}{\dot{m}_R}\left[\int_{\mathcal{V}}\nabla\cdot\tau\cdot\mathbf{v}\;d\mathcal{V}-\int_{\mathcal{V}}\tau:\nabla\mathbf{v}\;d\mathcal{V}\right] \tag{2.17}$$

where $\dot{m}_R$ is a reference global mass flow rate. The last term on the right hand side refers to viscous dissipation within the control volume. It reduces mechanical energy by dissipation of kinetic energy to internal energy. The viscous dissipation represents a loss term in Eq. (2.17), which can be directly related to the entropy generation, based on Eq. (2.12). Performing that substitution and comparing to Bernoulli's equation, the head loss becomes

$$H_l=\frac{1}{\dot{m}_R}\int_{\mathcal{V}}T\dot{P}_s\;d\mathcal{V} \tag{2.18}$$

Alternatively, this result can be expressed in terms of the local rate of exergy destruction, $\dot{X}_d$, due to friction irreversibilities of viscous dissipation at ambient tem-

perature, T_0, i.e.,

$$H_l = \frac{1}{\dot{m}_R} \int_{\mathcal{V}} \dot{X}_d \frac{T}{T_0} \, d\mathcal{V} \tag{2.19}$$

This result represents a useful alternative to conventional loss characterization. It can be seen that available energy loss is a local volumetric phenomenon involving exergy destruction. In contrast to past methods characterizing flow losses through global empirical coefficients, this approach allows local tracking of flow losses, since $\mathcal{V}$ can be taken as an arbitrarily located discrete volume. Entropy production encompasses all flow irreversibilities (thermal and friction), unlike pressure, which may be de-coupled from temperature under certain flow conditions. Reduced exergy destruction is a common objective, but changes of individual flow variables are generally problem dependent. For example, higher pressure losses with added baffles may be a desired way of increasing heat transfer rates in a heat exchanger. On the other hand, reduced pressure losses are needed in pipe flows, as they entail lower pumping input power. Thus, tracking local pressure changes does not generally identify problem areas. On the other hand, lower entropy production rates are considered to be a more robust and common objective. It can be more valuable than tracking end-to-end pressure losses, since the desired overall performance can be improved by re-designing locally.

In the next section, it will be shown that the previous results can be extended to turbulent flows. In particular, for near-isothermal incompressible turbulent flow, it will be shown that the mean turbulent entropy production reduces to an expression involving mean viscous dissipation and the dissipation of turbulent kinetic energy, i.e.,

$$\bar{T}\overline{\dot{P}_s} = \tau_{ij} \frac{\partial \bar{u}_i}{\partial x_j} + \bar{\varepsilon} \geq 0 \tag{2.20}$$

Equation (2.20) connects the magnitude of turbulent dissipation rate to the quality and efficiency of industrial processes [40]. Past studies have associated the dissipation of turbulent kinetic energy with other physical processes, such as the degree of segmentation, droplet and bubble breakdown, and chemical reaction [41]. A revised interpretation based on entropy production and the Second Law may provide a general framework for understanding the physical structures and processes leading to such breakdown.

In the following section, an overview of the turbulence formulation of the Second Law will be presented.

2.4 Reynolds Averaged Entropy Transport Equations

For turbulent flows, the Reynolds averaged entropy equation can be obtained after combining the positive definite and entropy transport equations. The resulting combined expression, called the Reynolds averaged Clausius-Duhem equality [34, 35] can be written as follows,

$$\frac{\partial}{\partial t}(\rho\bar{s}) + \frac{\partial}{\partial x_i}\left[\rho\bar{u}_i\bar{s} + \rho\overline{u_i's'} - \overline{\frac{k}{T}\frac{\partial T}{\partial x_i}}\right] = \overline{\frac{k}{T^2}\left(\frac{\partial T}{\partial x_i}\right)^2} + \overline{\frac{\tau_{ij}}{T}\frac{\partial u_i}{\partial x_j}} \tag{2.21}$$

were the overbar (i.e., $\overline{s}$) and prime (i.e., s') notations refer to mean and fluctuating components associated with the Reynolds averaging, respectively.

Since T and u_i (and consequently the viscous dissipation term) have mean and fluctuating components appearing in the denominator and numerator, modeling of Eq. (2.21) becomes highly complex. It becomes difficult to explicitly express the mean entropy production in terms of other mean flow variables alone. Two established approaches for expressing the mean entropy production are briefly addressed below.

2.4.1 Separate Time Averaging

In the first approach, the two sides of Eq. (2.21) are averaged seperately. For the entropy transport equation, Reynolds averaging yields

$$\overline{\dot{P}_s} = \frac{\partial}{\partial t}(\rho\bar{s}) + \frac{\partial}{\partial x_i}(\rho\bar{u}_i\bar{s} + \rho\overline{u_i's'}) + k\frac{\partial}{\partial x_i}\overline{ln\left[\bar{T}\left(1+\frac{T'}{\bar{T}}\right)\right]} \geq 0 \qquad (2.22)$$

The first term in Eq. (2.12) can be simplified by substituting $\partial(lnT)/\partial x_i$ for $(\partial T/\partial x_i)/T$ before time averaging. The time averaged positive definite entropy equation becomes

$$\begin{aligned}
\overline{\dot{P}_s} &= k\frac{\partial}{\partial x_i}(\overline{lnT})\frac{\partial}{\partial x_i}(\overline{lnT}) + k\overline{\frac{\partial}{\partial x_i}(lnT)'\frac{\partial}{\partial x_i}(lnT)'} + \mu\left[\overline{\left(\frac{1}{T}\right)}\left(\left(\frac{\partial\bar{u}_i}{\partial x_j}+\frac{\partial\bar{u}_j}{\partial x_i}\right)\frac{\partial\bar{u}_i}{\partial x_j}\right)\right] \\
&+ \mu\left[\overline{\left(\frac{1}{T}\right)}\left(\overline{\left(\frac{\partial u_i'}{\partial x_j}+\frac{\partial u_j'}{\partial x_i}\right)\frac{\partial u_i'}{\partial x_j}}\right)\right] + 2\mu\frac{\partial\bar{u}_i}{\partial x_j}\overline{\left(\frac{1}{T}\right)'\frac{\partial u_i'}{\partial x_j}} + \mu\frac{\partial\bar{u}_i}{\partial x_j}\overline{\left(\frac{1}{T}\right)'\frac{\partial u_j'}{\partial x_i}} \\
&+ \mu\frac{\partial\bar{u}_j}{\partial x_i}\overline{\left(\frac{1}{T}\right)'\frac{\partial u_i'}{\partial x_j}} + \mu\left[\overline{\left(\frac{1}{T}\right)'\left(\left(\frac{\partial u_i'}{\partial x_j}+\frac{\partial u_j'}{\partial x_i}\right)\frac{\partial u_i'}{\partial x_j}\right)}\right] \geq 0 \qquad (2.23)
\end{aligned}$$

A close examination of Eq. (2.23) reveals the physical processes leading to entropy production in turbulent flow. The first two terms on the right side are entropy production terms due to thermal fluctuations and transport. The terms in the first squared brackets represent the entropy production due to mean viscous effects. The terms in the second squared brackets represent entropy produced due to the dissipation of turbulent kinetic energy. The terms in the last squared brackets represent the mechanism of entropy produced by the interaction of fluctuating viscous effects and temperature fluctuations. The remaining terms represents the conversion of entropy production, due to mean viscous effects, to entropy production due to fluctuating viscous-temperature effects and back.

By defining the mean viscous stress and the fluctuating viscous stress, respectively,

as

$$\bar{\tau}_{ij} = \mu\left[\left(\frac{\partial \bar{u}_i}{\partial x_j} + \frac{\partial \bar{u}_j}{\partial x_i}\right)\right] \tag{2.24}$$

$$\tau'_{ij} = \mu\left[\left(\frac{\partial u'_i}{\partial x_j} + \frac{\partial u'_j}{\partial x_i}\right)\right] \tag{2.25}$$

then Eq. (2.23) becomes

$$\begin{aligned}\overline{\dot{P}_s} &= k\frac{\partial}{\partial x_i}(\overline{lnT})\frac{\partial}{\partial x_i}(\overline{lnT}) + k\overline{\frac{\partial}{\partial x_i}(lnT)'\frac{\partial}{\partial x_i}(lnT)'} + \overline{\left(\frac{1}{T}\right)}\bar{\tau}_{ij}\frac{\partial \bar{u}_i}{\partial x_j} + \overline{\left(\frac{1}{T}\right)\tau'_{ij}\frac{\partial u'_i}{\partial x_j}} \\ &+ \bar{\tau}_{ij}\overline{\left(\frac{1}{T}\right)'\frac{\partial u'_i}{\partial x_j}} + \frac{\partial \bar{u}_i}{\partial x_j}\overline{\left(\frac{1}{T}\right)'\tau'_{ij}} + \overline{\left(\frac{1}{T}\right)'\tau'_{ij}\frac{\partial u'_i}{\partial x_j}} \geq 0\end{aligned} \tag{2.26}$$

Modeling of this equation is considered to be more complicated than modeling of the standard turbulent kinetic energy equation. No models exist at the present time (to my knowledge) for the correlations involving the $(1/T)'$ terms. Any such correlations would be difficult to validate and/or measure with some degree of accuracy.

2.4.2 Combined Time Averaging

Modeling of the mean entropy generation can be simplified by the following approach, whereby the Clausius-Duhem equality is averaged. The left side of Eq. (2.12) is multiplied by temperature to give

$$T\dot{P}_s = \frac{k}{T}\left(\frac{\partial T}{\partial x_i}\right)^2 + \tau_{ij}\frac{\partial u_i}{\partial x_j} \tag{2.27}$$

Kramer-Bevan [29] presented a derivation of the time averaged form of Eq. (2.27), with the following result,

$$\bar{T}\bar{\dot{P}}_s + \overline{T'\dot{P}'_s} = k\frac{\partial}{\partial x_i}\overline{(lnT)}\frac{\partial \bar{T}}{\partial x_i} + k\overline{\frac{\partial}{\partial x_i}(lnT)'\frac{\partial T'}{\partial x_i}} + \bar{\tau}_{ij}\frac{\partial \bar{u}_i}{\partial x_j} + \overline{\tau'_{ij}\frac{\partial u'_i}{\partial x_j}} \tag{2.28}$$

In Eq. (2.28), the physical processes of conversion of entropy production, arising from mean viscous effects, to entropy production due to fluctuating viscous / temperature effects have been captured in the $\overline{T'\dot{P}'_s}$ correlation. Other terms remain as

previously described for Eq. (2.23). This equation seems to be more straightforward than Eqs. (2.22) - (2.23), provided that suitable empirical models can be developed for $\overline{T'\dot{P}'_s}$ and thermal gradient correlations. Kramer-Bevan [29] proposed a closure approximation for a subset of possible flow fields by using a Small Thermal Turbulence Assumption (STTAss). A detailed discussion of the STTAss will be given in an upcoming section. At this time, no model exists for the $\overline{T'\dot{P}'_s}$ correlation (to my knowledge). The following section attempts to provide such modeling.

2.4.3 Fluctuating Temperature and Entropy Production Correlation

In order to derive a general, combined time averaged equation for the mean entropy generation, the $T'\dot{P}'_s$ correlation was modeled after multiplying both sides of the entropy transport equation, Eq. (2.5), by T. Then, time averaging is performed to yield

$$\bar{T}\bar{\dot{P}}_s + \overline{T'\dot{P}'_s} = \bar{T}\left[\frac{\partial}{\partial t}(\rho\bar{s}) + \frac{\partial}{\partial x_i}(\rho\bar{u}_j\bar{s} + \rho\overline{u's'}) + k\frac{\partial}{\partial x_i}\overline{ln\left[\bar{T}\left(1+\frac{T'}{\bar{T}}\right)\right]}\right]$$
$$+\overline{T'\frac{\partial}{\partial x_i}(\rho u'_i\bar{s})} + \overline{T'\frac{\partial}{\partial x_i}(\rho\bar{u}_i s')} + \overline{T'\frac{\partial}{\partial x_i}(\rho u'_i s')} + \overline{kT'\frac{\partial}{\partial x_i}ln\left[\bar{T}\left(1+\frac{T'}{\bar{T}}\right)\right]} \quad (2.29)$$

By comparing Eq. (2.22) with Eq. (2.29), it can be shown that

$$\overline{T'\dot{P}'_s} = \overline{T'\frac{\partial}{\partial x_i}(\rho u'_i\bar{s})} + \overline{T'\frac{\partial}{\partial x_i}(\rho\bar{u}_i s')} + \overline{T'\frac{\partial}{\partial x_i}(\rho u'_i s')} + \overline{kT'\frac{\partial}{\partial x_i}ln\left[\bar{T}\left(1+\frac{T'}{\bar{T}}\right)\right]} \quad (2.30)$$

Using the chain rule of calculus,

$$\overline{T'\dot{P}'_s} = \rho\overline{T'u'_i}\frac{\partial\bar{s}}{\partial x_i} + \rho\bar{s}\overline{T'\frac{\partial u'_i}{\partial x_i}} + \rho\overline{T's'}\frac{\partial\bar{u}_i}{\partial x_i} + \rho\bar{u}_i\overline{T'\frac{\partial s'}{\partial x_i}} + +\overline{T'\frac{\partial}{\partial x_i}(\rho u'_i s')} \quad (2.31)$$
$$+\overline{kT'\frac{\partial}{\partial x_i}ln\left[\bar{T}\left(1+\frac{T'}{\bar{T}}\right)\right]} \quad (2.32)$$

By assuming incompressibility, the mean and instantaneous velocity fields are solenoidal and Eq. (2.32) reduces to

$$\overline{T'\dot{P}'_s} = \rho\overline{T'u'_i}\frac{\partial\bar{s}}{\partial x_i} + \rho\bar{u}_i\overline{T'\frac{\partial s'}{\partial x_i}} + \overline{T'\frac{\partial}{\partial x_i}(\rho u'_i s')} + \overline{kT'\frac{\partial}{\partial x_i}ln\left[\bar{T}\left(1+\frac{T'}{\bar{T}}\right)\right]} \quad (2.33)$$

This equation for the $\overline{T'\dot{P}'_s}$ correlation is a new result for turbulent incompressible flow. It is considered that all terms in this equation can be more readily determined than the past formulations. The following section considers modeling of individual terms in Eq. (2.33).

2.5 Eddy Viscosity Models of Mean Entropy Production

A few simplified models, based on the solution of the RANS equations and an eddy viscosity for mean entropy generation, have been documented in past literature [25, 25, 28, 29]. The linear eddy viscosity model assumes a Boussinesq relationship between the turbulent stresses (or second-moments) and the mean strain rate tensor through an isotropic eddy viscosity. Although these models attempt to minimize complexity, it is difficult to ascertain if the essence of relevant irreversibilities has been captured with sufficient accuracy, due to the lack of experimental data. It should be noted that no relevant experimental data regarding these turbulence correlations of entropy production has been measured or reported in the literature.

Moore and Moore [25] suggest the following correlations for mean entropy production, thermal diffusion and viscous dissipation, respectively,

$$\bar{T}\bar{\dot{P}}_s = \frac{k}{\bar{T}}\left[\left(\frac{\partial \bar{T}}{\partial x_i}\right)^2 + \overline{\left(\frac{\partial T'}{\partial x_i}\right)^2}\right] + \bar{\tau}_{ij}\frac{\partial \bar{u}_i}{\partial x_j} + \overline{\tau'_{ij}\frac{\partial u'_i}{\partial x_j}} \tag{2.34}$$

$$k\overline{\left(\frac{\partial T'}{\partial x_i}\right)^2} = k_t\left(\frac{\partial \bar{T}}{\partial x_i}\right)^2 \tag{2.35}$$

$$\overline{\tau'_{ij}\frac{\partial u'_i}{\partial x_j}} = \frac{\mu_t}{\mu}\bar{\tau}_{ij}\frac{\partial \bar{u}_i}{\partial x_j} \tag{2.36}$$

In Eqs. (2.35) and (2.36), k_t and μ_t denote turbulent molecular conductivity and the turbulent molecular viscosity, respectively. This model misses most of the

correlation in Eq. (2.28), due to the assumption that the temperature fluctuations are small compared to the mean temperature. Unfortunately, there is no experimental or theoretical evidence to verify that the missing terms are sufficiently small for all turbulent flows, over a range of flow conditions.

Due to these inconsistencies, particularly close to the wall, Kramer-Bevan proposed a different physically based model for the viscous dissipation correlation [29], i.e.,

$$\overline{\tau'_{ij}\frac{\partial u'_i}{\partial x_j}} = \tilde{\epsilon} \tag{2.37}$$

where $\tilde{\epsilon}$ is the "true" dissipation of turbulent kinetic energy. The definition of $\tilde{\epsilon}$ differs from the definition of dissipation of turbulent kinetic energy in the standard $k-\epsilon$ model (documented in Ref. [1]). The resulting model of entropy production becomes

$$\bar{T}\bar{\dot{P}}_s = \frac{k+k_t}{\bar{T}}\left(\frac{\partial \bar{T}}{\partial x_i}\right)^2 + \bar{\tau}_{ij}\frac{\partial \bar{u}_i}{\partial x_j} + \tilde{\epsilon} \tag{2.38}$$

In contrast to the Moore model, which uses the positive definite entropy equation, the small thermal turbulence model (STTAss) is based on time averaging of the entropy transport equation. It assumes that the fluctuating component of temperature is small compared to the mean temperature. In formulating this model, the fluctuating temperature in Eq. (2.22) is replaced by a Taylor series expansion of those functions. The expansions are truncated after the linear terms, thereby yielding the following equations for mean entropy production and mean specific entropy [29],

$$\overline{\dot{P}_s} = \frac{\partial}{\partial t}(\rho\bar{s}) + \frac{\partial}{\partial x_i}\left(\rho\bar{u}_i\bar{s} - \frac{1}{\bar{T}}\left(\frac{c_v\mu_t}{Pr_t}+k\right)\frac{\partial \bar{T}}{\partial x_i}\right) \geq 0 \tag{2.39}$$

$$\bar{s} = s_r + c_v ln\frac{\bar{T}_s}{T_r} - R\ ln\frac{\rho_s}{\rho_r} \tag{2.40}$$

The turbulent Prandtl number, Pr_t, arises in Eq. (2.39) because the entropy-velocity correlation has been modeled with a Reynolds analogy. Under the STTAss,

extra terms arise in the entropy transport equation, with an increase in the diffusion term. This is equivalent to adding an effective diffusivity, $c_v\mu_t/Pr_t$, to the thermal diffusivity in the laminar model.

2.6 Turbulence Modeling with the Second Law

The exact equation for the dissipation of turbulent kinetic energy (TKE) is useful to understand the meaning and importance of various terms, but usually it cannot be rigorously modeled in its full detailed form [42]. Modeling of the exact equation is traditionally carried out by drastic simplification and it usually involves a laborious empirical determination of five or more closure coefficients. This section attempts to obtain the dissipation of TKE using the Second Law under the STT Assumption. In this approach, the local entropy production in convection dominated flow can be computed based on mean quantities (velocity and temperature) obtained from the solution of the RANS equations, using both the transport and positive definite forms of the entropy equation. Since the dissipation of TKE (denoted by ϵ) appears in the positive definite mean entropy production equation, it is anticipated that its local value can be computed throughout the flow domain by the Clausius-Duhem equation, Eq. (2.21). A formulation for the proposed model is presented for the eddy viscosity and second moment turbulent closure.

Combining Eqs. (2.22), (2.28) and (2.33) we obtain the following combined entropy equation for turbulent flow,

$$\begin{aligned}
\bar{T}\overline{\dot{P}_s} &= \bar{T}\left[\frac{\partial}{\partial t}(\rho\bar{s}) + \frac{\partial}{\partial x_i}(\rho\bar{u}_i\bar{s} + \rho\overline{u's'}) + k\frac{\partial}{\partial x_i}\overline{ln\left[\bar{T}\left(1+\frac{T'}{\bar{T}}\right)\right]}\right] \\
&= k\frac{\partial}{\partial x_i}\overline{(lnT)}\frac{\partial\bar{T}}{\partial x_i} + k\overline{\frac{\partial}{\partial x_i}(lnT)'\frac{\partial T'}{\partial x_i}} + \bar{\tau}_{ij}\frac{\partial\bar{u}_i}{\partial x_j} + \overline{\tau'_{ij}\frac{\partial u'_i}{\partial x_j}} \\
&- \rho\overline{T'u'_i}\frac{\partial\bar{s}}{\partial x_i} - \rho\bar{u}_i\overline{T'\frac{\partial s'}{\partial x_i}} - \overline{T'\frac{\partial}{\partial x_i}(\rho u'_i s')} - k\overline{T'\frac{\partial}{\partial x_i}ln\left[\bar{T}\left(1+\frac{T'}{\bar{T}}\right)\right]} \quad (2.41)
\end{aligned}$$

The fourth term on the right side of Eq. (2.41) represents the dissipation of turbulent kinetic energy. This term, called ϵ, can be interpreted as a physical mechanism by which exergy ($T\dot{P}_s$) is destroyed in turbulent flow. This view agrees with the traditional interpretation that associates ϵ with the rate at which turbulent kinetic energy is converted to internal energy in the flow. The terms after the second equality in Eq. (2.41) reveal the physical processes leading to exergy destruction in turbulent flow. The total exergy destroyed in turbulent flow is the sum of the exergy destroyed due to irreversible heat transfer (terms 1, 2 and 8), viscous dissipation (terms 3 and 4), turbulent enthalpy transfer (term 5), and the work done by fluctuating temperature against turbulent entropy transfer by mass exchange (term 6 and 7). All of these irreversible processes dissipate useful mechanical energy into less useful internal energy.

It is important to note that Eq. (2.41) re-emphasizes the importance of maintaining the positivity of ϵ in numerical simulations. The time-averaged entropy equation does not shed much light, in regards to modeling of ϵ, except when simplified by the Small Thermal Turbulence Assumption. Complete modeling of the Clausius-Duhem equation can only be achieved through experiments for calibrating closure coefficients, when approximating the non-linear fluctuating terms. Two approaches (linear eddy viscosity and DSM closures) will be described for modeling and simplification of Eq. (2.41).

2.6.1 Linear Eddy Viscosity Closure

The terms in the time averaged entropy equation, Eq. (2.41), can be determined from a linear eddy viscosity model as follows (see appendix for derivation),

$$\frac{\partial}{\partial t}(\rho\bar{s}) \;+\; \frac{\partial}{\partial x_i}\left[\rho\bar{u}_i\bar{s} - \frac{1}{\bar{T}}\left(\frac{c_v\mu_t}{Pr_t}+k\right)\frac{\partial\bar{T}}{\partial x_i}\right] = \frac{1}{\bar{T}^2}\left[(k+\gamma k_t)\left(\frac{\partial\bar{T}}{\partial x_i}\right)^2\right] + \frac{\bar{\tau}_{ij}}{\bar{T}}\frac{\partial\bar{u}_i}{\partial x_j}$$

$$+ \quad \frac{\tilde{\epsilon}}{\bar{T}} + \left\{ \frac{k}{\bar{T}^2} \left(\frac{\partial T'}{\partial x_i} \right)^2 + \frac{k}{2} \frac{\partial}{\partial x_i} \left(\frac{1}{\bar{T}} \right) \frac{\partial}{\partial x_i} \overline{(T'^2)} \right.$$

$$- \quad \frac{\rho c_v}{\bar{T}} \left[\frac{\partial}{\partial x_i} \left(\frac{\overline{u_i' T'^2}}{\bar{T}} \right) + \bar{u}_i \frac{\partial}{\partial x_i} \left(\frac{\overline{T'^2}}{\bar{T}} \right) \right]$$

$$+ \quad \left. \frac{\rho c_v}{2\bar{T}^2} \left[\frac{\partial}{\partial x_i} \left(\overline{u_i' T'^2} \right) + \bar{u}_i \frac{\partial}{\partial x_i} \left(\overline{T'^2} \right) \right] \right\} \tag{2.42}$$

The left side of Eq. (2.42) was developed from the entropy transport equation on the left side of Eq. (2.5). That expression must equal the positive definite rate of entropy production from the Second Law in Eq. (2.12), which becomes the right side of Eq. (2.42). On the left side of Eq. (2.42), the terms represent the transient change of mean entropy (first term) and the transport of entropy by mass and heat flow (second term in square brackets). On the right side of Eq. (2.42), the terms refer to entropy production associated with thermal molecular and turbulent diffusion of the mean temperature field (first term in square brackets), viscous dissipation of the mean velocity field (second term) and irreversibilities in dissipation of turbulent kinetic energy (third term). Within the braces, the terms represent entropy production corresponding to irreversible temperature fluctuations (first and second terms) and irreversible interactions between fluctuating velocity and temperature fields (remaining terms). The individual terms in braces can be obtained through the following correlation governing the dynamics of T'^2 (Tennekes, Lumley [43]), i.e.,

$$\bar{u}_i \frac{\partial}{\partial x_i} \left(\frac{\overline{T'^2}}{2} \right) = \frac{\partial}{\partial x_i} \left(\frac{1}{2} \overline{u_i' T'^2} - \alpha \frac{\partial}{\partial x_i} \left(\frac{\overline{T'^2}}{2} \right) \right) - \overline{u_i' T'} \frac{\partial \bar{T}}{\partial x_i} - \alpha \overline{\left(\frac{\partial T'}{\partial x_i} \right)^2} \tag{2.43}$$

where α is the thermal diffusivity.

2.6.2 Differential Second Moment (DSM) Closure

The Differential Second Moment Closure directly solves the transport equations for the Reynolds stresses in the momentum equation. This approach is used to obtain

the scalar fluxes in turbulent flow, involving the transport of passive scalars. The computed turbulent heat flux, $\overline{T'u'}$ and Eq. (A.1) can then be used directly in Eq. (2.41) to give

$$\begin{aligned}\frac{\partial}{\partial t}(\rho\bar{s}) \;+\; & \frac{\partial}{\partial x_i}\left[\rho\bar{u}_i\bar{s} + \frac{\rho c_v}{\bar{T}}\overline{u_i'T'} - \frac{k}{\bar{T}}\frac{\partial\bar{T}}{\partial x_i}\right] = \frac{k}{\bar{T}^2}\left(\frac{\partial\bar{T}}{\partial x_i}\right)^2 + \rho\overline{T'u_i'}\frac{\partial\bar{s}}{\partial x_i} + \frac{\bar{\tau}_{ij}}{\bar{T}}\frac{\partial\bar{u}_i}{\partial x_j} \\ & + \frac{\tilde{\epsilon}}{\bar{T}} + \left\{\frac{k}{\bar{T}^2}\left(\frac{\partial T'}{\partial x_i}\right)^2 + \frac{k}{2}\frac{\partial}{\partial x_i}\left(\frac{1}{\bar{T}}\right)\frac{\partial}{\partial x_i}\overline{(T'^2)}\right. \\ & - \frac{\rho c_v}{\bar{T}}\left[\frac{\partial}{\partial x_i}\left(\frac{\overline{u_i'T'^2}}{\bar{T}}\right)\bar{u}_i\frac{\partial}{\partial x_i}\left(\frac{\overline{T'^2}}{\bar{T}}\right)\right] \\ & \left. + \frac{\rho c_v}{2\bar{T}^2}\left[\frac{\partial}{\partial x_i}\left(\overline{u_i'T'^2}\right) + \bar{u}_i\frac{\partial}{\partial x_i}\left(\overline{T'^2}\right)\right]\right\} \qquad (2.44)\end{aligned}$$

This approach dispenses with the eddy viscosity to express the turbulent shear stress in terms of mean flow quantities.

Similarities in turbulent irreversibilities can be observed in Eqs. (2.42) and (2.44). From left to right on the left side of Eq. (2.44), the terms represent the transient change of mean entropy (first term) and the transport of entropy by mass and heat flow (second term in square brackets). Unlike Eq. (2.42), the heat flow is not modeled with a turbulent conductivity in this case. On the right side of Eq. (2.44), the terms refer to entropy production corresponding to thermal molecular diffusion of the mean temperature field (first term), diffusive entropy transport in the mean flow field due to velocity fluctuations (second term), viscous dissipation of the mean velocity field (third term) and dissipation of turbulent kinetic energy (fourth term). In a similar way as previously described, the terms within braces represent entropy production corresponding to irreversible temperature fluctuations (first and second terms) and irreversible interactions between fluctuating velocity and temperature fields (remaining terms).

In the following section, an overview of the numerical Second Law formulation will be presented.

2.7 Numerical Solution Procedure

The discrete equations for velocity, pressure, temperature and entropy production are obtained by integration of the governing equations, Eqs. (2.2), (2.3), (2.4) and (2.12), over finite control volumes and time intervals. The solution of the discrete equations is obtained with a Control-Volume Finite Element Method (CVFEM). A schematic of the finite element and control volume discretization is illustrated in Fig. 2.2. The domain is subdivided into linear, quadrilateral finite elements. The grid is arranged in a collocated manner, so that velocity components, pressure, temperature and entropy production are obtained at nodes located at every element corner. The finite element model uses a local (s,t) coordinate system, when calculating shape functions and other element properties (see Fig. 2.2). Each element is subdivided into four sub-control volumes, with internal sub-control-volume (SCV) boundaries coincident with the local coordinate surfaces defined by $s = 0$ and $t = 0$. An 'effective' control volume is defined by all sub-volumes from elements surrounding a particular node in the mesh.

The global Cartesian coordinates and scalar values, ϕ, are related to local element values using bilinear shape functions, N,

$$\phi(s,t) = \sum_{i=1}^{4} N_i(s,t)\Phi_i \tag{2.45}$$

where

$$N_1(s,t) = \frac{1}{4}(1+s)(1+t) \tag{2.46}$$

$$N_2(s,t) = \frac{1}{4}(1-s)(1+t) \tag{2.47}$$

$$N_3(s,t) = \frac{1}{4}(1-s)(1-t) \tag{2.48}$$

$$N_4(s,t) = \frac{1}{4}(1+s)(1-t) \tag{2.49}$$

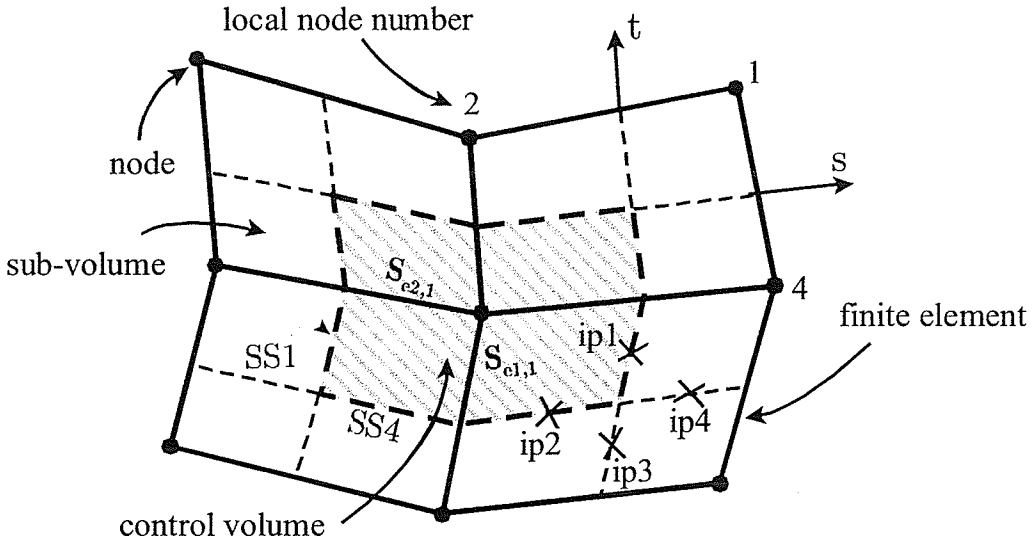

Figure 2.2: Element and Control Volume

and Φ_i refer to values of ϕ at local nodes $i = 1, 2, 3, 4$.

The spatial derivatives of the scalar are evaluated according to

$$\left.\frac{\partial \phi}{\partial \vec{x}}\right|_{(s,t)} = \sum_{i=1}^{4} \left.\frac{\partial N_i}{\partial \vec{x}}\right|_{(s,t)} \Phi_i \tag{2.50}$$

To obtain the shape function derivatives in Eq.(2.50), we apply the chain rule, to obtain

$$\begin{bmatrix} \frac{\partial N_i}{\partial x} \\ \frac{\partial N_i}{\partial y} \end{bmatrix} = \frac{1}{|J|} \begin{bmatrix} \frac{\partial y}{\partial t} & \frac{-\partial y}{\partial s} \\ \frac{-\partial x}{\partial t} & \frac{\partial x}{\partial s} \end{bmatrix} \begin{bmatrix} \frac{\partial N_i}{\partial s} \\ \frac{\partial N_i}{\partial t} \end{bmatrix} \tag{2.51}$$

where J is the determinant of the Jacobian of transformation given by

$$|J| = \frac{\partial x}{\partial s}\frac{\partial y}{\partial t} - \frac{\partial y}{\partial s}\frac{\partial x}{\partial t} \tag{2.52}$$

Also,

$$\frac{\partial x}{\partial s} = \sum_{i=1}^{4} \frac{\partial N_i}{\partial s} x_i \tag{2.53}$$

$$\frac{\partial x}{\partial t} = \sum_{i=1}^{4} \frac{\partial N_i}{\partial t} x_i \tag{2.54}$$

$$\frac{\partial y}{\partial s} = \sum_{i=1}^{4} \frac{\partial N_i}{\partial s} y_i \tag{2.55}$$

$$\frac{\partial y}{\partial t} = \sum_{i=1}^{4} \frac{\partial N_i}{\partial t} y_i \tag{2.56}$$

In order to enable the algebraic representation of transient and source terms, the sub-element area bounded by a specific range of $0 \leq s \leq s'$ and $0 \leq t \leq t'$ is given by

$$A = \int_0^{t'} \int_0^{s'} |J| ds dt \approx |J|_{(\frac{s'}{2}, \frac{t'}{2})} \tag{2.57}$$

The outward normal, $\vec{\Delta n}$, to any sub-control volume surface is evaluated at the midpoint (or integration point, ip), between any point 1 and 2 on a sub-surface, and it is expressed in the form

$$\vec{\Delta n} = \Delta y \; \hat{i} - \Delta x \; \hat{j} \tag{2.58}$$

where $\hat{i}$ and $\hat{j}$ are unit vectors and

$$\Delta x = \left.\frac{\partial x}{\partial s}\right|_{ip} (s_2 - s_1) + \left.\frac{\partial x}{\partial t}\right|_{ip} (t_2 - t_1) \tag{2.59}$$

$$\Delta y = \left.\frac{\partial y}{\partial s}\right|_{ip} (s_2 - s_1) + \left.\frac{\partial y}{\partial t}\right|_{ip} (t_2 - t_1) \tag{2.60}$$

Integral conservation equations were obtained by integrating the differential coordinate - independent form of the conservation equations over a discrete control volume, SCV1, in Figure 2.2, i.e.,

$$\int_V \frac{\partial(\rho\phi)}{\partial t} dV + \int_S (\rho \vec{v} \phi) \cdot \vec{dn} - \int_S (\Gamma \nabla \phi) \cdot \vec{dn} = \int_V S_\phi dV \tag{2.61}$$

where $\vec{v}$ and $\vec{dn}$ refer to the velocity and the unit normal vector at the surface, respectively. The surface, S, represents a union of $S_{e1,1}$, $S_{e2,1}$, $SS1$ and $SS4$ in Figure 2.2.

Based on the definitions in Fig. 2.2, the diffusive and convective fluxes through SS1, for example, were computed as follows,

$$\int_{SS1} (\Gamma \nabla \phi) \cdot \vec{dn} = \sum_{j=1}^{4} \left(\Gamma_x \left. \frac{\partial N_i}{\partial x} \right|_{ip1} \Delta y_{SS1} - \Gamma_y \left. \frac{\partial N_i}{\partial y} \right|_{ip1} \Delta x_{SS1} \right) \Phi_j \tag{2.62}$$

$$\int_{SS1} (\rho \vec{v} \phi) \cdot \vec{dn} = \rho \left(v^{ip1} \Delta x_{SS1} - u^{ip1} \Delta y_{SS1} \right) \phi^{ip1} \tag{2.63}$$

The lower case variables, ϕ^{ip} and u^{ip}, denote the integration point value and Δx_4 and Δy_4 are respective changes in x and y, as the sub - surface is traversed counter-clockwise. The Physical Influence Scheme (PINS) of convective upwinding was employed in this study [30]. PINS obtains the integration point value of the scalar by a local approximation of the governing equation at the integration point. The procedure accounts for transient, pressure and source terms, when calculating the convected variable at the integration point. A detailed procedure for the construction of these integration point operators and equations and the closure of the mass - momentum equations can be found in Ref. [30].

For the transient storage term, a lumped mass approach is adopted over a time interval $\Delta t = t^{n+1} - t^n$, such that

$$\frac{\partial}{\partial t} \int_{scv1} \rho \phi \, dV = \rho J \frac{(\Phi_1^{n+1} - \Phi_1^n)}{\Delta t} \tag{2.64}$$

where J is the area of SCV1.

The source term is relatively straightforward to evaluate. For a given source term, which includes the pressure gradient, the body force and contribution from the viscous stress terms in the momentum equations, the integral is evaluated as

$$\int_{scv1} S_\phi \, dV = S_\phi|_{\frac{1}{2},\frac{1}{2}} J \tag{2.65}$$

where a midpoint approximation has been used in evaluating P at $(\frac{1}{2}, \frac{1}{2})$. The above relations will be used to derive the control volume conservation equations and entropy production in the upcoming section.

A local numbering scheme (ranging from 1 to 4) within each element allows the finite element equations to be developed locally and independently of the mesh configuration. The resulting element stiffness equations apply to all elements, irrespective of distortion or skewing of the solution domain. Following a conventional assembly procedure for the finite elements, the local node equations are assembled into the global system of equations involving global nodes. This assembly procedure yields a banded matrix of coefficients. A direct banded solver is used to solve this algebraic set of equations.

The final step requires discretization of the Second Law, based on post-processing of the computed temperature and velocity fields. Using Fourier's Law of Conduction in Eq. (2.5), letting k denote the thermal conductivity, and expressing the absolute entropy in terms of temperature using the Gibbs equation, we obtain

$$\dot{P}_s = \frac{\rho c_p}{T}\frac{\partial T}{\partial t} + \nabla \cdot \left(\rho \mathbf{v} s - \frac{k \nabla T}{T} \right) \tag{2.66}$$

For the purpose of our analysis, we will discretize the terms in the entropy transport equation with the same temporal and spatial approximations as adopted earlier in the energy equation. Thus,

$$\begin{aligned} \dot{P}_s &= \frac{\rho c_p}{T_i} J \left(\frac{T_i^{n+1} - T_i^n}{\Delta t} \right) + \rho c_p u^{ip} s^{ip} \Delta y - \rho c_p v^{ip} s^{ip} \Delta x \\ &+ \frac{1}{T_{ip}} \left(k \Delta x \sum_{i=1}^{4} \frac{\partial N_i}{\partial y} T_i - k \Delta y \sum_{i=1}^{4} \frac{\partial N_i}{\partial x} T_i \right) \end{aligned} \tag{2.67}$$

where J refers to Jacobian of the transformation and it represents the area of the sub-control volume (i.e. dashed sub-quadrant of element depicted in Fig. 2).

For an incompressible substance in single-phase flow, the absolute entropy at the integration points, s^{ip}, is obtained by a linear interpolation involving nodal values of entropy and the shape functions. The absolute entropy is found at the node from a piecewise logarithmic equation of state, based on integration of the Gibbs equation (Eq.(2.9)) for incompressible fluids.

We will assume a piecewise constant distribution for the temperature gradient within a sub-control-volume. The local entropy generation at a node is then approximated by the average local entropy generated in the control volume. The positive-definite equation is discretized as follows,

$$\dot{P}_s = \frac{k}{T_i^2}\left[\left(\sum_{i=1}^{4}\frac{\partial N_i}{\partial x}T_i\right)^2 + \left(\sum_{i=1}^{4}\frac{\partial N_i}{\partial y}T_i\right)^2\right] + \frac{\mu}{T_i}\Phi_i \tag{2.68}$$

where

$$\Phi_i = 2\left[\left(\frac{\partial u}{\partial x}\right)_m^2 + \left(\frac{\partial v}{\partial y}\right)_m^2\right] + \left(\frac{\partial v}{\partial x} + \frac{\partial u}{\partial y}\right)_m^2 \tag{2.69}$$

and m refers to the discretized forms of the bracketed terms based on the local derivatives for the bilinear element using Eqs. (2.46) - (2.49). In both cases, the values of the scalar variables (velocity and temperature) are obtained directly from the solution of the appropriate governing equation.

The boundary entropy production rate is calculated directly from Eq. (2.12) to ensure non-negative values in conjuction with the specification of boundary conditions. In this approach, only the spatial derivatives of the velocity and temperature are computed at the boundaries for the corresponding boundary value of entropy production. Alternatively, entropy fluxes across the control volume boundaries can be computed through Eq. (2.5) to provide closure of the entropy production at the boundaries.

Chapter 3

Experimental Techniques for Entropy Production Mapping

In this chapter, new experimental techniques based on the combined use of Particle Image Velocimetry (PIV) and Planar Laser Induced Fluorescence (PLIF) will be developed. PIV measures the spatial distribution of fluid velocity, while PLIF is used to acquire temperature data in a flow field. The PIV/PLIF method offers certain advantages over standard methods of anemometry for entropy related experimental analysis. Previous methods, limited by single-point measurement techniques, can only focus on measuring single-point entropy production or an averaged entropy production over a finite volume. On the other hand, PIV /PLIF methods provide a whole-field method, while allowing non-intrusive and time-varying measurements of the instantaneous velocity and temperature distribution at a specific cross-section of a flow field. This thesis addresses a need to gain physical data regarding the detailed structure of available energy losses throughout a flow field. Since the PIV and PLIF techniques provide multi-point instantaneous data, these methods can address the objective by measuring local variations of the entropy production rates. Thus, the new experimental technique yields whole-field measurements of instantaneous entropy production with a non-intrusive, optical method.

3.1 Operating Principle of the PIV/PLIF System

PIV is based on imaging light scattered by small particles in a flow illuminated by two laser light pulses at very short intervals, which are characterized by the flow velocity. The scattered light has the same frequency as the incident laser light at low wavelengths. On the other hand, Laser Induced Fluorescence (LIF) does not result from a scattering process, but rather an absorption and wavelength conversion process. The light emitted by molecules and atoms in a de-excitation process, induced by absorption of a photon of higher energy (from a laser source), is red-shifted to longer wavelength. These combined features of the PIV /PLIF allow synchronization of the two measurement techniques without much duplication of the hardware system.

The optical configuration for the PIV / PLIF setup consists of a light source, light sheet optics, fluorescent dye for PLIF, tracer particles for PIV and CCD / CMOS cameras (see Figure 3.1). In conjunction with the experimental facility, a complete PIV/PLIF system also consists of a processor unit and analysis software.

In Particle Image Velocimetry (PIV), the pulsed laser illuminates a planar cross-section in the center of the flow region of interest, parallel to the flow and perpendicular to the camera. The camera captures the image of the illuminated particles in successive frames at each instant when the light sheet is pulsed. The two successive images were processed, subdivided into small interrogation regions, and matched based on a correlation analysis to determine the displacement of a group of particles, elapsed time and the local fluid velocity. When M is the magnification of the camera, the velocity is given by a first order estimate, i.e.,

$$\vec{U} = \frac{M\Delta\vec{s}}{\Delta t} \tag{3.1}$$

where $\Delta\vec{s}$ is a displacement vector in the image plane and Δt is the pulse time interval [44].

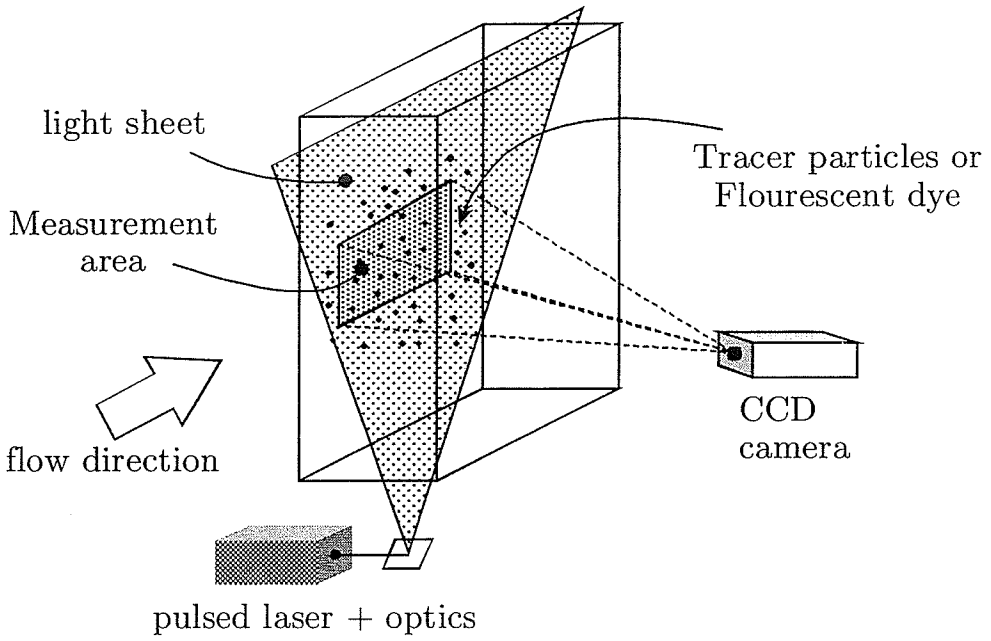

Figure 3.1: Experimental Setup of PIV/PLIF

In Planar Laser Induced Fluorescence, molecules and atoms of a fluorescent dye are excited to a higher electronic energy state via a pulsed laser absorption and subsequently fluoresce. The local fluorescence intensity, I, varies with intensity of excitation light, I_e, concentration of the fluorescent dye, C, quantum efficiency as a function of temperature, ϕ, and the molar absorptivity, ϵ, i.e.,

$$I = f I_e \epsilon C \phi(T) \tag{3.2}$$

where f is a factor corresponding to the optical setup [39, 47]. For a known concentration and excitation energy, the quantum energy decreases with higher temperatures. This dependence constitutes the basis for PLIF temperature measurements. The temperature is determined from Eq. (3.2) as follows,

$$T - T_{ref} = \frac{\Delta I}{f I_e \epsilon C \Delta \phi} \tag{3.3}$$

Thus, quantitative analysis is based on temperature calibration images that correlate the variation of intensity of the image with the local temperature and laser energy.

3.2 PIV Interrogation Analysis and the Dynamic Range of Velocity

Interrogation analysis is a major conceptual element in the PIV technique, whereby the spatial velocity distribution is obtained over a regular grid of small subregions using statistical methods. In particular, the recorded image frame is divided into small areas, called *interrogation areas.* Correlation based techniques are used within each interrogation region to produce a vector representing the average particle displacement. Auto-correlation and cross correlation techniques are used for high particle density image analysis, while other methods like particle tracking and particle pairing are limited to relatively low density images. A high density image arises when the number of particles is between 7 - 10 image pairs per interrogation area. In auto correlation, an interrogation area is correlated with itself. Cross-correlation analysis, used in this study, correlates an interrogation area with a second area, which is offset in the mean flow direction. The cross-correlation employed within each interrogation area allows an unambiguous determination of the direction of displacement to give instantaneous values of both components of fluid velocity (u and v) in two dimensions. The hydrodynamic properties of the tracer particles are very important in PIV because the particle velocity, and not the fluid velocity, is determined. The particles used for PIV study should be neutrally buoyant (have approximately the same density as water in the water tunnel) in the fluid to eliminate possible error in the measurement due to particle settling as they transverse the flow field [32]. Other details describing an interrogation analysis are available in the literature [45, 46, 47].

The PIV resolution becomes very important for high Reynolds number experi-

ments that attempt to resolve small-scale variations embedded in large-scale motion. Such scenarios exist in turbulence measurements and cases where it is necessary to resolve small-scale flow structures around large objects. Two velocity resolution issues arise, i.e., [47]

- the dynamic velocity range, which relates to the ability to resolve very small velocity displacements between particle image pairs, and
- the dynamic spatial range, which relates to the size of the smallest velocity structure that can be resolved in the flow field.

The dynamic spatial range is defined as "the field of view in the object space divided by the smallest resolvable spatial variation" [48]. This range coincides with the number of independent vectors obtained from the interrogation analysis (without overlapping). The smallest length scale that can be resolved is given by

$$\lambda_{min} = \frac{N_I d_p}{M} = \frac{L_o}{L_I} N_I \tag{3.4}$$

where L_o is the physical dimension of the field of view in the x_1 direction, L_I is the corresponding pixel dimension of the camera, N_I is the number of interrogation areas, and d_p is the pixel pitch of the CCD array (9μm for the Kodak ES1.0)

For all cases tested in this thesis, the 32 $\times$ 32 pixel interrogation gives vector maps with the lowest noise. For this interrogation area, each flow field is resolved to a factor of approximately 32 in the field of view with the Kodak ES1.0 CCD camera ($L_I \simeq 1024$). This dynamic spatial range is rather low for turbulence measurements. Equation (3.4) shows that a decrease in the resolved length scale, λ_{min}, will require the reduction of the view area size at a fixed number of interrogation cells. Thus, higher resolution (dynamic spatial range of approximately 76) can be achieved by a higher magnification of the measurement area with extension rings between the

lens and the camera. However, higher magnification of the image may lead to higher velocity bias errors. Better modifications include higher resolution CCD (e.g. 2k $\times$ 2k pixel) or higher format recording mediums with physical dimensions in the order of 1cm.

The dynamic range is the ratio of the maximum velocity to the minimum velocity resolvable by a particular PIV system. The minimum resolvable velocity occurs in the order of the rms error, when determining the displacement of the particle image. The accuracy of the velocity measurement is approximately 1% of the full scale velocity for the PIV system (DANTEC) used in this thesis, giving a dynamic velocity range of at least 100 for the 32 $\times$ 32 pixel interrogation. This value applies to both positive and negative ranges of velocities. It is viewed that this dynamic range is suitable for fluid mechanics phenomena investigated in this thesis and other applications.

3.3 PLIF Calibration and Signal Processing

The first step in the PLIF calibration procedure is to find the optimum concentration resulting in the maximum temperature resolution with low absorption phenomena. The corresponding absorption, A, is calculated from

$$A = e^{-l\eta_{Rhod}C} \tag{3.5}$$

where η_{Rhod} is the extinction coefficient of Rhodamine B in water and l is the optical path length. A general procedure involves running a series of trials at a fixed energy level to determine the optimum concentration at which the temperature resolution is maximum, while maintaining linearity between the gray level and temperature. The measurement precision at a concentration value is indicated by the slope of the curve obtained in the preliminary experiment. Typically, the temperature resolution ap-

proaches an asymptotic minimum at an optimum concentration and then it increases thereafter.

Signal processing consists of a final translation of the recorded images to temperatures via the calibration maps. The final calibration relates the response of every pixel of the CCD camera to varying temperature, laser energy levels and concentration. A precise analysis of the instant temperature at discrete locations in an actual measurement region is determined from

$$T - T_{ref} = \frac{I - I_{ref}}{\beta} \tag{3.6}$$

where I_{ref} is the intensity of the fluorescent signal at the reference temperature, T_{ref}. The denominator is statistically determined during calibration.

3.4 Combined PIV / PLIF Measurement

The wavelength of the fluorescence emitted from PLIF is longer than the wavelength of the reflected laser light, thereby making simultaneous measurements of both velocity and temperature possible. An orange optical filter is attached to the front of the camera for the fluorescent image to cut off reflected light from the PIV particles. A green (narrow band) optical filter allows a second camera to detect laser light scattered by the particles.

In this thesis, the camera and image capturing systems detect particle images and fluorescent images successively at two different instants. Combining velocity and temperature measurements allows the estimation of entropy production. In addition, the temperatures can be re-sampled with spatial resolution of the PIV vectors, ensuring maximum correlation between the heat transfer irreversibility and the fluid friction irreversibility in every interrogation area. Experimental correlations between velocity and temperature will provide useful information to address unresolved modelling

issues regarding fluctuating velocity / temperature terms in the turbulent entropy production equation (Eq. 2.12) in heat transfer applications.

3.5 Conversion Algorithm and Implementation

3.5.1 Entropy Production with FlowManager

Unlike velocity or temperature, the measurement of entropy cannot be performed directly. However, Eq. (2.12) can be used in an indirect way to characterize the flow irreversibility. The measured velocities and temperatures are displayed over a discrete grid by the PIV software. The velocity and temperature components at grid position (i, j) are denoted by $u(i, j)$, $v(i, j)$, and $T(i, j)$. Thus, Eq. (2.12) yields the following expression for the entropy production rate for 2-D, laminar flows.

$$\begin{aligned}
\dot{P}_s &= \frac{k}{T(i,j)^2}\left[\frac{T(i+1,j)-T(i-1,j)}{2\Delta x}\right]^2 + \frac{k}{T(i,j)^2}\left[\frac{T(i,j+1)-T(i,j-1)}{2\Delta y}\right]^2 \\
&+ \frac{\mu}{T(i,j)}\left[\frac{u(i,j+1)-u(i,j-1)}{2\Delta y} + \frac{v(i+1,j)-v(i-1,j)}{2\Delta x}\right]^2 \\
&+ 2\frac{\mu}{T(i,j)}\left[\left(\frac{u(i+1,j)-u(i-1,j)}{2\Delta x}\right)^2 + \left(\frac{v(i,j+1)-v(i,j-1)}{2\Delta y}\right)^2\right] \qquad (3.7)
\end{aligned}$$

where Δx and Δy refer to the grid spacing in the x and y directions.

The entropy production and loss coefficient algorithms are implemented through MatLab scripts and other externally developed C++ functions linked to Dantec Dynamics' FlowManager software. The user could select the data input (i.e., vector map) and choose the newly developed scripts to determine the output (entropy production and loss coefficient contours). FlowManager would transfer data to MatLab and receive results back from the computed entropy production results. Firstly, the acquired image would be selected. Then, a new calculation based on the selection is added, and the MatLab command window is started. The selected data can now

be accessed inside the command window. The calculations defined by the MatLab script may be executed. Upon return to FlowManager, the results of the calculations may be stored in the database as data sets and/or graphical displays. The numerical entropy analysis requires a gateway to C++ functions developed externally, which were accessed through the MatLab environment in FlowManager. Since the entropy analysis is computationally intensive, an add-on to MatLab can allow compilation of the scripts into executable codes, which could improve the calculation speeds.

3.5.2 Data Post-Processing for Spatial Derivatives

Errors in spatial derivatives of velocity can be decomposed into two components: (i) bias error associated with the displacement measurement and (ii) the propagated uncertainty due to the spatial differentiation of the velocity field. For a smaller grid size, the bias error decreases. The bias error associated with the Fast Fourier transform-based cross correlation algorithm in the commercial software (FlowManager; Dantec Dynamics) has been minimized by a sub-pixel resolution of the PIV images. As stated earlier, the displacement error is approximately 0.1 pixels over 8 pixels for our present configuration, based on a 32×32 interrogation size.

The entropy production algorithm contains multiple products of velocity derivatives. Hence, it is imperative to reduce the error associated with the determination of spatial derivatives. Two approaches are suggested. A twice differentiable empirical function could be fitted to the data. The spatial derivative is then obtained directly by the differential of the empirical function. This approach requires an elaborate, often difficult interpolation routine for multi-dimensional output of PIV. A better approach is a local piecewise smoothing of the experimental data followed by the application of forward differences, central differences or a Richardson central difference scheme over an adaptive window to calculate the derivatives.

Smoothing or filtering the experimental data discards the noise in terms of experimental scatter and it performs a least-squares approximation through a path that minimizes error for all data points in the field. In FlowManager, an average filter on a 2-D field is implemented in the form of a top-hat Gaussian filter with uniform weighting. The size of vectors in the neighborhood of a position (i, j) is specified by odd numbers, m and n. The filter calculates an average of vectors in a rectangular domain of size $m \times n$ surrounding a vector. The average value is substituted for all entries in the initial matrix. The average is calculated by the following formula,

$$\bar{u}(x,y) = \frac{1}{mn} \sum_{i=x-\frac{n-1}{2}}^{x+\frac{n-1}{2}} \sum_{j=y-\frac{n-1}{2}}^{y+\frac{n-1}{2}} u(i,j) \tag{3.8}$$

In addition to the average filter, a spline fit based on a second order polynomial least squares algorithm was also used in this thesis for data smoothing. The cubic spline was applied in commercial software (OriginLab), while the average filter was implemented in MatLab. The derivatives of velocity and the entropy analysis were implemented using MatLab scripts and other DLLs based on C++.

Smoothing algorithms mitigate against error in the calculation of derivatives and they provide better approximations to an actual flow distribution. However, the interpretation of smooth curves or surfaces must be limited to flow structures present in the raw data from which they were obtained.

3.5.3 Loss Mapping in Turbulent Flows

Unlike near-isothermal laminar flows (such as unheated pipe flows) where the only physical process producing entropy is the mean viscous dissipation, the rate of dissipation of turbulent kinetic energy is needed to compute entropy production in turbulent flows. Also, it is desirable to determine the relationship between entropy production and fundamental turbulence, such as the kinetic energy. Thus, a segment for ex-

tracting mean and turbulent quantities from the velocity data was incorporated in the conversion algorithm. Since entropy production in turbulent flows involves the turbulent kinetic energy dissipation rate, a segment of the conversion algorithm was devoted to its estimation. Details regarding the estimation method for ε will be discussed in Section 3.6

3.5.4 Temperature Field Post-Processing

The average temperature map obtained from PLIF can show scattering in the data from pixel to pixel. Normally, a validation technique will be applied to the acquired image in a fashion similar to PIV images before translation to temperature. However, the commercial software does not allow such flexibility. Therefore, a surface smoothing filter was applied to the final temperature map in the conversion algorithm to enhance the quality of the data.

3.6 On the Estimation of the Dissipation Rate, ε

The general expression for the balance of mechanical energy in fluid flow is given by Eq. (2.15). The effect of the mean and fluctuating quantities on the total mechanical energy of a turbulent flow can be separated by the Reynolds averaging procedure. By subtracting the balance equation for the kinetic energy of the mean motion from Eq. (2.15), an expression for the balance of kinetic energy of turbulence is obtained, i.e.,

$$\begin{aligned}\frac{D}{Dt}\frac{\overline{k^2}}{2} &= -\frac{\partial}{\partial x_i}\overline{u_i'\left(\frac{p}{\rho}+\frac{k^2}{2}\right)} - \overline{u_i'u_j'}\frac{\partial \bar{u}_j}{\partial x_i} + \nu\frac{\partial}{\partial x_i}\overline{u_j'\left(\frac{\partial u_i'}{\partial x_j}+\frac{\partial u_j'}{\partial x_i}\right)} \\ &\quad - \nu\overline{\frac{\partial u_j'}{\partial x_i}\left(\frac{\partial u_i'}{\partial x_j}+\frac{\partial u_j'}{\partial x_i}\right)} \end{aligned} \tag{3.9}$$

Equation (3.9) requires that the net convection of turbulent kinetic energy (term 1) balances the flow work or work done by the total dynamic pressure of turbulence

(term 2), net work of turbulent stresses (term 3 - term 4), minus the dissipation of turbulent kinetic energy (last term). In the absence of periodic oscillation in the flow, the total dissipation in turbulent flows is a sum of a mean (viscous shear stress) and a random (dissipation of turbulent kinetic energy) part. It should be noted that the viscous shear stress performs deformation work, which increases the internal energy of the fluid at the expense of the turbulent kinetic energy [43]. Since turbulence consists of a continuous spectrum of scales ranging from more energetic large scales to essentially dissipative small scales, a continuous supply of energy from the large scales or 'eddies' is required to maintain turbulence. Otherwise, turbulence decays rapidly and loss analysis of the fluid system reduces to an analysis involving only the mean viscous dissipation, as in laminar flows.

By expansion, the 12-term dissipation of turbulent kinetic energy tensor, ε, in equation (3.9) can be expressed as

$$\varepsilon = \nu \overline{\frac{\partial u_i'}{\partial x_j}\frac{\partial u_j'}{\partial x_i}} + \overline{\frac{\partial u_j'}{\partial x_i}\frac{\partial u_j'}{\partial x_i}} \tag{3.10}$$

Measurement of all terms in Eq. (3.10) is difficult. A simplified form is assumed based on the theory of homogenous turbulence and isotropy [49]. In homogeneous turbulence, the first term in Eq. (3.10) vanishes due to incompressibility, i.e, $\overline{u_j' \partial^2 u_i'/\partial x_i \partial x_j} = 0$, resulting in a 9-term tensor for ε, as in

$$\varepsilon = \nu \overline{\frac{\partial u_j'}{\partial x_i}\frac{\partial u_j'}{\partial x_i}} \tag{3.11}$$

The essence of homogeneous turbulence, namely that the mean properties of turbulence including the mean velocity are independent of translations of the coordinate axis, is idealized. However, it provides a reasonable basis for estimating experimental turbulence quantities [50]. The assumption of homogeneous turbulence also implies a relationship between the viscosity and the mean square vorticity through Eq. (3.11),

i.e.,

$$\varepsilon = \nu\overline{\omega_k\omega_k} \tag{3.12}$$

where ω_k is the vorticity. Equation (3.12) is the enstrophy - based dissipation described by Tennekes and Lumley [43].

Isotropic turbulence is based on the premise that small turbulent scales are statistically independent of rotation and reflection of the coordinate axis at sufficiently high Reynolds numbers. A further simplification with the isotropic turbulence assumption can be obtained from Eq. (3.11) in the following two-dimensional form,

$$\varepsilon = 6\nu\left[\overline{\left(\frac{\partial u_1'}{\partial x_1}\right)^2} + \overline{\left(\frac{\partial u_1'}{\partial x_2}\right)^2} + \overline{\frac{\partial u_1'}{\partial x_2}\frac{\partial u_2'}{\partial x_2}}\right] = 15\nu\overline{\left(\frac{\partial u_1'}{\partial x_1}\right)^2} \tag{3.13}$$

The Kolmogorov length scale represents the smallest length scale of turbulence, $\eta = (\nu^3/\varepsilon)^{1/4}$ [43]. Another length scale associated with the energy dissipated by turbulent eddies is the Taylor micro-scale, λ, i.e.,

$$\lambda^2 = \frac{\overline{u_1'^2}}{\overline{(\partial u_1'/\partial x_1)^2}} \tag{3.14}$$

Rearranging Eq. (3.13) in terms of Taylor micro scale leads to

$$\varepsilon = 15\nu\frac{u_1'^2}{\lambda^2} \tag{3.15}$$

A similar dimensional analysis based on the integral length scale, l, and a premise of mechanical equilibrium gives [43, 50]

$$\varepsilon = A\frac{u_1'^3}{l} \tag{3.16}$$

where A is a proportionality constant of the order of unity. Equation (3.16) can be used for the estimation of the dissipation rate when only one integral length scale characterizes the flow region. Also, it does not require the dissipation of turbulent kinetic energy to be equal to the production of turbulent kinetic energy, as its derivation is independent of the presence of turbulence production.

Another class of dissipation estimation methods (common with LDA practitioners) uses a time series analysis and the turbulence energy spectrum. The following homogeneous turbulence relation applies

$$\varepsilon = 2\nu \int_0^4 k^2 E(k,t) dk \tag{3.17}$$

with a corresponding isotropic version given by

$$\varepsilon = 15\nu \int_0^\infty k_1^2 E_1(k_1) dk_1 \tag{3.18}$$

where E refers to the power spectrum, k is the wavenumber, and the subscripts '1' denote the one-dimensional values.

There are similarities between the correlation analysis of PIV and Large Eddy Simulation (LES). LES computes the dynamics of the large energy containing scales of motion, up to a certain cut-off wavelength, while modelling only the effect of the small, unresolved flow structures on the larger resolved scales. The underlying principle is that the large-scale motions are affected by the geometry and they are not universal. The small-scale motions have a weaker influence on the Reynolds stress and they have a somewhat universal character represented by simple sub-grid scale (SGS) models. The approach in LES requires the solution of the Navier-Stokes equations for the filtered velocity field on a computational grid, with the objective of resolving the actual flow field with fewer discrete volumes. In the same way, the correlation techniques in PIV give velocities which are results of a spatial average over a discrete volume or interrogation area. In LES, the filter size is proportional to a cut-off wavelength in the inertial subrange of the turbulence energy spectrum, whereas the size of the interrogation area determines the filter width, which averages the smaller scales of motion in PIV. Since the spatial filtering properties of PIV are similar to LES, it is veiwed that benefits of the theory of sub-grid scale modelling in

LES will be helpful in the estimation of small-scale turbulence characteristics from PIV data.

With the filter in the inertia subrange, the turbulence dissipation rate in LES can be approximated by the SGS dissipation rate,

$$\varepsilon \simeq \varepsilon_{SGS} = -2\tau_{ij}\bar{S}_{ij}, \quad \bar{S}_{ij} = \frac{1}{2}\left(\frac{\partial \bar{u}_i}{\partial x_j} + \frac{\partial \bar{u}_j}{\partial x_i}\right) \tag{3.19}$$

where $\bar{S}_{ij}$ is the filtered rate of strain tensor and τ_{ij} is the SGS stress. Several SGS stress models have been applied in previous LES studies at high Reynolds numbers. The first sub-grid model to be widely used was reported by Smagorinsky [51]. Other models that have been developed with the goal of improving the Smagorinsky model include the dynamic model of Germano et al. [52, 53, 54], Bardina scale similarity model [55], Clark Gradient Model [56], structure function model of Métais et al.[57] and the transport equation model [58, 59]. The relevant expressions are provided for the Smagorinky model and the Gradient model in an upcoming section.

The experimental determination of the dissipation rate has depended on the simplified expression outlined previously, or their variants with associated limitations. The following section provides a brief review of the measuring techniques in past studies.

3.6.1 Total Dissipation Measurement

This approach considers all terms of the velocity gradient tensor in the total dissipation equation (Eq. 3.10) from measured values. Since the PIV technique permits the measurement of instantaneous velocity data in a whole-field space, the possibility exists for the direct calculation of the turbulence dissipation rate by spatial derivatives of velocity. However, the spatial range of PIV cannot usually be extended up to the required resolution for exact measurements, due to limitations imposed by the hard-

ware, such as the size of the recording medium and the maximum allowable sampling speed [48, 60]. Therefore, spatial limitations in LDA based dissipation measurements apply to PIV [40]. Generally, the wire separation in multi-point probes measuring all three velocity components and their derivatives at a point, should not exceed $\Delta x \approx 0.3\eta$ in LDA, in order to keep the error in velocity derivatives for isotropic flow below 5% [61]. Also, a wire length of $L < 5\eta$ keeps the error in the turbulence dissipation rate below 10 - 20 % [62]. Saarenrinne et al. [40] proposed an analogous restrictive requirement in PIV, where (depending on the flow) the size of the PIV interrogation window and the laser light thickness do not exceed 30% of the lateral Taylor's micro scale and 5 times the Kolmogorov length scales, respectively. Only a few papers have reported ε using the total dissipation method, e. g. Piirto et al. [63](PIV), Browne et al. [61] (LDA) and Kit et al. [64](LDA).

As stated earlier, the spatial resolution of the Kodak ES1.0 camera in this thesis is at least an order of magnitude higher than the Kolmogorov length scale in the turbulent flow, so that simplified expressions for ε are needed. Furthermore, only two components of velocity are available. Therefore, the computed dissipation rate will be reported with other methods described in an upcoming section.

3.6.2 Dimensional Analysis Based on Equilibrium Turbulence

This approach assumes local isotropy and it has been used to estimate the turbulence energy dissipation in stirred vessels [17, 65]. The method uses Eq. (3.16) and it has been shown to give reasonable qualitative results, despite implementation difficulties regarding the variation of length scales in certain flows. In flows where the Taylor micro scale can be estimated, dimensional analysis based on Eq. (3.15) has been used [40]. Estimates of ε based on Eq. (3.16) are reported in this thesis.

3.6.3 Turbulent Kinetic Energy Balance (TKEB)

The dissipation rate in the turbulent kinetic equation has been obtained as a closing term by measuring terms represented by mean flow convection, diffusion and production of turbulent energy and neglected terms of viscous diffusion. The applicability of this method is limited by an appropriate model for the pressure diffusion term, $\partial(u_j'p)/\partial x_j$, which is difficult to measure experimentally [66]. Although all other terms in the turbulent kinetic energy equation involve large-scale quantities, the limitation imposed by spatial resolution has limited the application of the method to simple geometries.

3.6.4 Space -Time Covariance and Energy Spectra

Taylor's Frozen Turbulence hypothesis allows Eq. (3.13) to be recast in terms of a time series differential of the velocity fluctuation, i.e.,

$$\varepsilon = 15\nu\overline{(\partial u_1'/\partial x_1)^2} = 15\nu\overline{(\partial u_1'/\partial t)^2}/\bar{u}^2 \tag{3.20}$$

In order to obtain a reliable value of ε, a calibration of the time derivative is necessary and it can be based on the energy spectrum function in Eq. (3.17). Turan and Azad [66] developed a 'zero-wire-length dissipation method', which defined the one-dimensional spectrum of the longitudinal velocity fluctuation by an integral,

$$\int_0^\infty E_1(k_1)dk_1 = \overline{u_1'}^2 \tag{3.21}$$

The sampling rate of the PIV system in this thesis is not high enough to allow this spectra analysis.

3.6.5 Large Eddy PIV Method

Sheng et al. [41] viewed the resolution of finite scales by the PIV method, much like the LES approach and they have devised a method to use full-field velocity data

to estimate dissipation rates. The large eddy PIV estimation method is based on a dynamic equilibrium assumption between the spatial scale that can be resolved by PIV and the sub-grid length scales. When the interrogation or filter size is much smaller than the integral length scale of the flow ($L_I/N \ll l$), the turbulence dissipation rate can be approximated by Eq. (3.19). In the current study, the Clark Gradient model and the Smagorinsky model were used for the SGS stress. For the Gradient model,

$$\tau_{ij} = \frac{1}{12}\Delta^2 \frac{\partial \bar{u}_i}{\partial u_k}\frac{\partial \bar{u}_j}{\partial u_k} \tag{3.22}$$

where Δ is the width of the interrogation area. The Smagorinsky model is given by

$$\tau_{ij} = -(C_s\Delta)^2|\bar{S}|\bar{S}_{ij} \tag{3.23}$$

where $|S|$ is the characteristic filtered rate of strain, $\sqrt{2\bar{S}_{ij}\bar{S}_{ij}}$, and C_s is the Smagorinsky coefficient (proportional to Δ), taken to be 0.07 in the present study.

The large eddy PIV method, as well as other simplified models based on the isotropic assumption in this thesis, do not preclude the possibility of obtaining high resolution measurements, where detailed turbulent structures are captured [67]. However, it provides a useful estimate of turbulence dissipation in whole-field regions where the dynamic range of the velocity measurements captured by PIV is limited by spatial resolution.

In the following chapters, three application problems are considered: (i) laminar channel flow between parallel plates, (ii) turbulent channel flow and (iii) free convection in a differentially heated cavity. In the first case, validation of the newly developed technique of flow irreversibility measurement is performed through comparisons with analytical solutions. The second problem outlines additional modelling issues that arise in turbulent flows. The experimental results are compared with DNS data for validation purposes. The third problem has a numerical complement, based on the CVFEM, for additional validation.

Chapter 4

Case Study 1: Flow Irreversibility in a Parallel Channel

Wall bounded turbulent flows have been extensively investigated because of their technological importance. Viscous dissipation is the main frictional irreversibility in laminar flows but other less understood irreversibilities arise with fluid turbulence. For example, energy costs to deliver oil through a pipeline or accelerate airplanes are considerably higher when the flow becomes turbulent.

4.1 Overview

Extensive past research effort has been devoted to the understanding of the physics of wall-bounded flows using single-point velocity measurement techniques. The earliest measurements by Nikuradse were limited to the mean velocity field [68]. Similar data acquired with rough walls provided information for the correlation of friction factors in the design formula for turbulent friction and head loss in circular ducts [69] and the Moody Chart [1]. Since that time, numerous studies have been conducted with data including the turbulent intensities, near-wall turbulence [70], and low to high order turbulent statistics for a wide range of Reynolds numbers [71, 72]. Particle Image Velocimetry, like other whole-field turbulence diagnostic methods such as Direct

Numerical Simulation (DNS), presents additional insight to address other less understood aspects of wall-bounded turbulent flows, regarding the nature of (coherent) structures in turbulent flows [73]. Turbulent structures play a significant role in the energy transfer and dynamics of turbulent flows.

This chapter describes PIV measurements and predictions of fully developed laminar and turbulent flows in a water channel. The study extends previous measurements to mapping the local distribution of irreversibilities in a channel at different Reynolds numbers. The principal objective is to document entropy production in a turbulent channel flow, which allows the examination of the new loss mapping technique with PIV. The long-term objective is a new design optimization technology based on local mapping of entropy production in internal and external flow engineering devices.

Consider incompressible flow in a parallel channel of length , L, width, D and spaced h apart. It is assumed that the width is much greater that the height. The head loss due to frictional effects in the channel is related to the Darcy's friction factor, f, as follows,

$$H_l = h_l g = f\frac{L\bar{u}^2}{4h} \tag{4.1}$$

where $\bar{u}$, h_l and g are the mean velocity, head loss, and acceleration due to gravity, respectively. As shown in section 2.3, the loss term due to viscous dissipation in the mechanical energy equation can be related to entropy production and head loss by

$$H_l = \frac{1}{\dot{m}}\int_{\forall} \tau : \nabla\vec{v}d\forall = \frac{1}{\dot{m}}\int_{\forall} T\dot{P}_s d\forall \tag{4.2}$$

where $\dot{m}$ and $\forall$ refer to the mass flow rate through the channel and differential control volume, respectively. By combining Eqs. (4.1) and (4.2) and substituting $d\forall = DLdy$ and $\dot{m} = \rho\bar{u}Dh$ in the resulting equation, the integral value of mean entropy production in an adiabatic channel can be related to Darcy's friction factor, i.e.,

$$f = \frac{4}{\rho \bar{u}^3} \int \bar{T} \bar{\dot{P}}_s dy \tag{4.3}$$

where ρ, $\bar{T}$, and $\dot{P}_s$ are the density, mean temperature and entropy production rate per unit volume, respectively. The integral value of the entropy production rate is obtained from the positive definite entropy equation, based on spatial gradients of velocity, dissipation of turbulent kinetic energy and temperature. The Reynolds number based on the friction velocity, Re_τ, is computed with the friction velocity, u_τ, half channel height, w, and the kinematic viscosity, ν. Similarly, the Reynolds number based on the bulk velocity, Re, is computed with the mean velocity, hydraulic diameter and the kinematic viscosity. Fluid properties are obtained at a temperature of 295 K. A useful observation is that Eq. (4.3) suggests that entropy production can be used as a standardized metric for loss characterization in duct flows. By using entropy production in this way, the equivalent friction factor becomes a product of the local exergy destruction integrated over the flow domain and a constant based on averaged values of the flow variables.

Darcy's friction factor is a dimensionless group defined as follows,

$$f = \frac{8\tau_w}{\rho \bar{u}^2} \tag{4.4}$$

The following computations with DNS data will show close agreement between friction factors calculated by Eqs. (4.3) and (4.4) with the Colebrook friction factor for channel flow. This close agreement will provide useful validation of the newly derived entropy production model for turbulent flows and the positive definite equation, which can be used for optimization studies.

4.2 Experimental Set-up and Procedure

Experimental studies of channel flow were performed in a water tunnel with PIV and 5 micron diameter polyamide seeding particles (see Figure 4.1). The test section of the water tunnel was 0.76m high, 0.7m wide and 1.82m long. An enclosed rectangular channel made from 18mm thick plexiglass, was set with a spacing of 30mm from the lower wall of the test section, in order to avoid flow interference with the boundary layer developing on the bottom wall. The test section and rectangular channels were made of plexiglass to permit illumination from all sides. For this particular set-up, the laser and its reflecting optics were placed such that the laser light sheet penetrates the plane of the flow from the bottom of the tunnel. The contraction section of the water tunnel was preceded by a honeycomb arrangement to reduce any large-scale turbulence in the flow so that the velocity in the test section is uniform. The laminar flow measurements were carried out in a channel (12.6 mm high, 60 cm wide and 1.6 m long). The height was increased to 18mm for turbulent flow measurements. The leading edge of the top and bottom plates of the channel were tapered. Also, 2mm high square rod trips were placed 2cm downstream of the leading edge for turbulent flow measurements. Measurements were recorded sufficiently downstream of the channel inlet, so that fully developed conditions were obtained.

A planar cross-section in the center of the channel, parallel to the flow and perpendicular to the wall, was illuminated by reflecting optics and a two-chamber Gemini PIN Nd:Yag pulsed laser. The interrogation region of the FlowMap software and camera is centered about the channel flow region within the water tunnel. The PIV images were recorded with a Dantec HiSence CCD camera for the laminar case and a Kodak ES1.0 for turbulent flows. The camera was placed on a traversing mechanism to facilitate repeatability of the measurements. Two measurement sets were taken

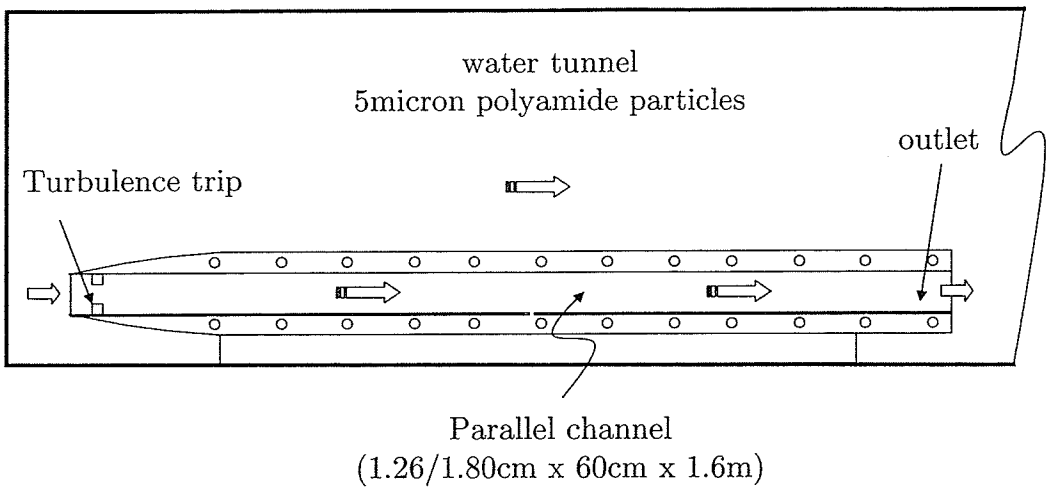

Figure 4.1: Channel Schematic

in a preliminary experiment at two locations downstream of the channel entrance to find the location where the flow is fully developed. The final velocity measurements were taken at a downstream position, $x \approx 160h$ for the turbulent flow and $x \approx 200h$ for the laminar flow case. The final measurement at each Reynolds number consist of full-field view ($0 < y \leq\sim h$) image maps of the channel and another view where the camera is focused to a region closer to the wall. In the latter case, the camera was focused on a smaller image area ($0 < y \leq\sim 0.5h$) to obtain a higher resolution, which is required in turbulence measurements. The full-field measurement confirmed symmetry of the mean velocity fields about the channel centerline, so half-channel measurements are reported.

The vector fields were validated with a moving average procedure. In the full field view, the velocity data exhibited very little noise. In fact, less than 0.4% of the vectors were rejected by an average of surrounding vectors. The number of particles per interrogation area was reduced in the half-channel image maps, but higher magnifica-

tions are needed to achieve a higher spatial dynamic range. Increased magnification will reduce the depth of camera focus. The $f-$number of the camera was also reduced to enlarge the camera aperture. Coupled with the increased magnification, the lower $f-$number leads to an even smaller depth of camera focus. Hence, the light thickness was set to the minimum, to enhance the quality of the image maps and correlated velocity field. A tighter tolerance in the moving average validation resulted in a correlated vector map with more spurious vectors. In all cases tested, about 10-12% of vectors were rejected and they were randomly located in the resolved velocity field.

A process for establishing the time between laser pulses was needed to optimize the seeding density. In these studies, the peak height ratio was set to 1 and the velocity length slider was set to 25%. This means that any vectors longer than 25% of the length of the interrogation area were highlighted in red and considered to be inaccurate. Starting with a very low time between pulses and gradually increasing the time for successive image captures, the velocities in the vector map become smoother and more continuous. The optimum time between pulses was selected. This time interval between pulses was kept constant, so consistent results were gathered throughout tests involving a particular flow configuration. In all cases tested, a 32×32 interrogation was used with 50% overlap in the horizontal and vertical directions. A Gaussian window function and a filter function were employed to suppress the error introduced by the FFT.

4.3 Results and Discussion

4.3.1 Laminar Flow

A total of 1500 statistically independent image maps was interrogated to generate the velocity vectors. The post-processed velocity results are used to find local rates of

entropy production. The conversion algorithm for measured entropy production and flow irreversibilities was validated against analytical entropy production results for laminar water flow between two parallel plates. The measured velocity and entropy production results are compared with the corresponding analytical solutions, at $Re_h = 518$, in Figures 4.2 (a) - (b), respectively.

The analytical solution for laminar flow between parallel plates is a well-known quadratic profile, which is analogous to the Pouiseille velocity profile in pipe flows. In Figure 4.2 (a), the deviations of measured velocities are within 1.2% of the analytical values. It can be observed in Fig. 4.2, that the entropy production rises in the cross-stream (y) direction to its peak value at the wall, but does not change noticeably in the streamwise (x) direction, due to fully developed conditions. The maximum difference between the measured entropy production and the analytical result is 6.6%. These results provide useful validation of the post-processing and conversion algorithm for entropy production due to friction irreversibilities. For this problem, thermal irreversibilities are neglected, since the flow is effectively isothermal. In Figure 4.2 (a) - (b), a reference point, $x(ref)$, designates a location where analytical solutions of laminar boundary layer development suggest fully developed conditions within the parallel plates. Measurements at two different locations downstream of this point (0.65 mm and 15.22 mm from the reference point) are taken, in order to confirm that both profile shape and magnitude are preserved. The measured results show close agreement between both downstream points, thereby providing evidence of fully developed conditions.

In many wall-bounded flows, including this channel flow problem, the highest entropy production is located at the wall, where the largest spatial gradients of velocity and temperature are encountered. Unfortunately, near-wall measurements of velocity and temperature are often most difficult. In particular, limitations of camera reso-

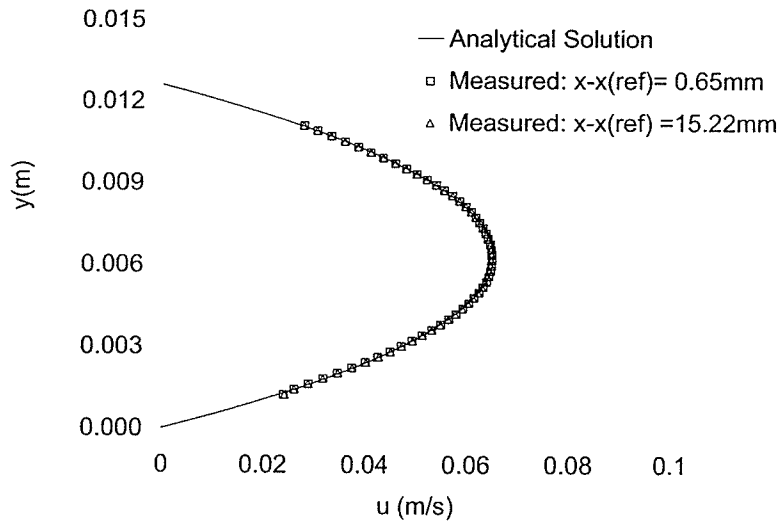

(a)

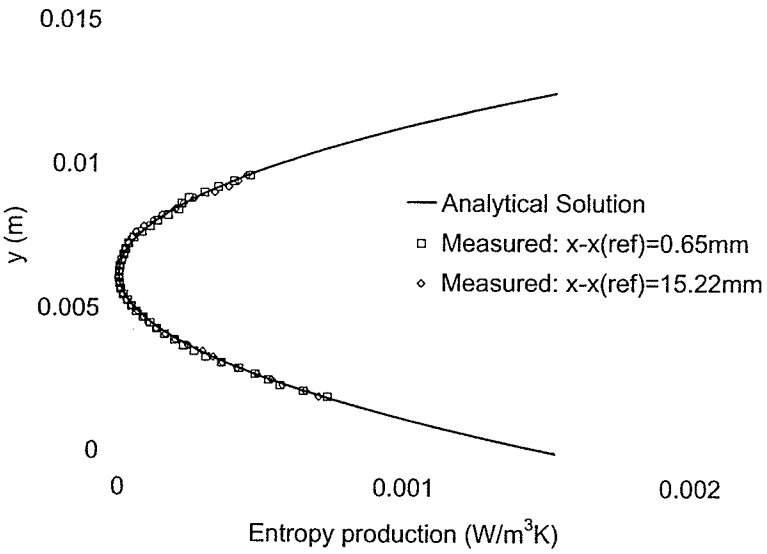

(b)

Figure 4.2: Laminar Channel Flow at $Re_h = 518$: (a) Velocity (b) Entropy Production

lution and particle tracking near the wall arise with PIV technology. Attempts were made to focus the particle tracking and image processing as close to the wall as possible. In Figure 4.3(a), measured velocities were obtained within a distance of 0.60 mm from the wall. It can be observed that close agreement between measured velocities and the analytical solution is obtained close to the wall. Both places at different stream-wise locations (i.e., 0.6 mm and 5.0 mm from the reference point) yielded close agreement, so near-wall measurements were considered to be independent of the x-position under fully developed conditions.

The PIV validation method rejected velocity vectors at locations $0 < y < 0.6$mm, thereby leaving a 'data hole' of a few interrogation cells wide in the near-wall region. Local data extrapolation, based on the previously mentioned second order polynomial fit, measured values in the vicinity of the data hole and the known velocities at the wall were applied and illustrated in Fig. 4.3. The regressed data was only substituted in the matrix location where invalid vectors had been located. The data extrapolation is justified in our near-wall laminar flow measurements because they are typically less than four interrogation sizes wide in the large scale flow fields. Issues involving the range of length scales resolved with the PIV technique arise in such turbulent flows.

In regards to entropy production, Figure 4.3(b) shows close agreement between the analytical solution and measured data. Closer agreement is observed than results predicted by a detailed measurement uncertainty analysis (see chapter 6). However, the error increases closer to the wall, so the reported experimental uncertainties give a maximum bound on expected errors of the measured entropy production close to the wall.

After multiplying entropy production by temperature in Figure 4.3(b), those results give the destruction of exergy (or energy availability in the flow stream). This conversion allows units to be expressed directly in terms of lost power per unit volume

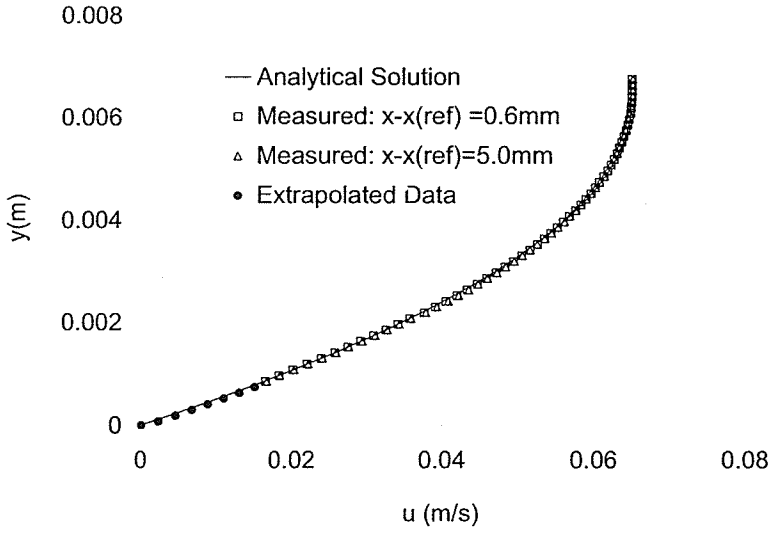

(a)

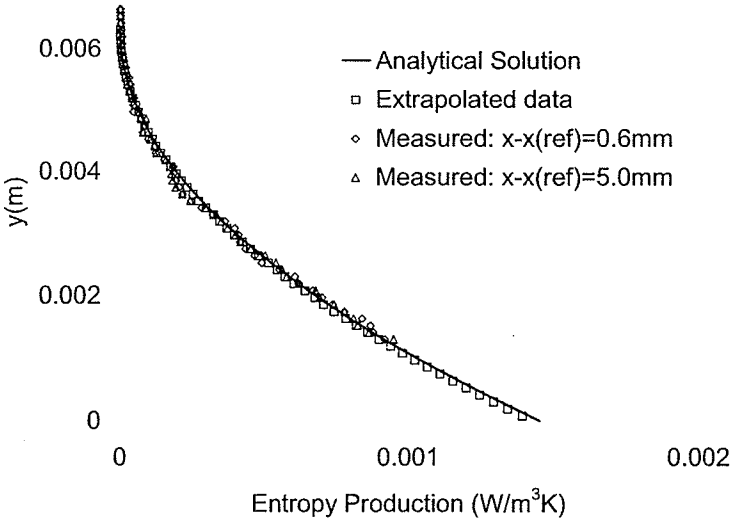

(b)

Figure 4.3: Half Channel Measurements at $Re_h = 518$: (a) Velocity (b) Entropy Production

of fluid, which can be more practically interpreted than units of lost power per degree Kelvin (units of entropy production). The local head loss coefficient can be derived from these results, after multiplying the local entropy production rate by the bulk temperature and volume size corresponding to the discrete PIV grid points, as well as dividing by the channel mass flow rate. This result represents the local exergy destruction per unit mass flow.

It is useful to verify that this loss coefficient yields the same result as the standard loss coefficient for channel flows. For incompressible, fully developed flow between parallel plates spaced $2w$ apart, the velocity profile can be expressed as

$$u(y) = u_c \left[2\left(\frac{y}{w}\right) - \left(\frac{y}{w}\right)^2 \right] \tag{4.5}$$

where u_c is the centerline velocity. Using Eqs. (2.12) and (4.5) to evaluate the entropy production rate, multiplying by temperature and integrating across the channel yields the following result,

$$\int_{-w}^{w} T\dot{P}_s dy = \frac{8\mu u_c^2}{3w} \tag{4.6}$$

Substituting Eq. (4.6) into Eq. (4.3) gives the analytical result of

$$f = \frac{96}{Re_D} \tag{4.7}$$

Thus, the entropy formulation of Eq. (4.3) for channel flow reduces to $f = 96/Re_D$, which is the expected friction factor in undergraduate textbooks for viscous flow between two wide flat plates [69].

Additional laminar flow measurements were performed at $Re_h = 314$ and 402 and the exergy based local friction factor is summed over the entire domain. Extrapolated data was used close to the wall. Computed friction factors from the experimental results based on Eq. (4.3) at all Reynolds numbers are illustrated in Fig. 4.4. The experimental results show excellent agreement with analytical friction factors computed from Eq. (4.7).

More generally, the exergy based loss coefficient becomes equivalent to the corresponding global loss parameter currently used in industry. For example, the loss coefficient for a tee junction in undergraduate textbooks would be equivalent to the summed exergy destruction per unit mass flow over the spatial domain encompassing the tee junction. A surface plot of measured entropy production in the channel is depicted in Fig. 4.5 ($Re_h = 518$) to show the quality of the experimental data. Clearly, the Second Law based loss mapping is feasible except close to the wall, where limitations imposed by the PIV system necessitates the use of extrapolation schemes to fill possible data holes.

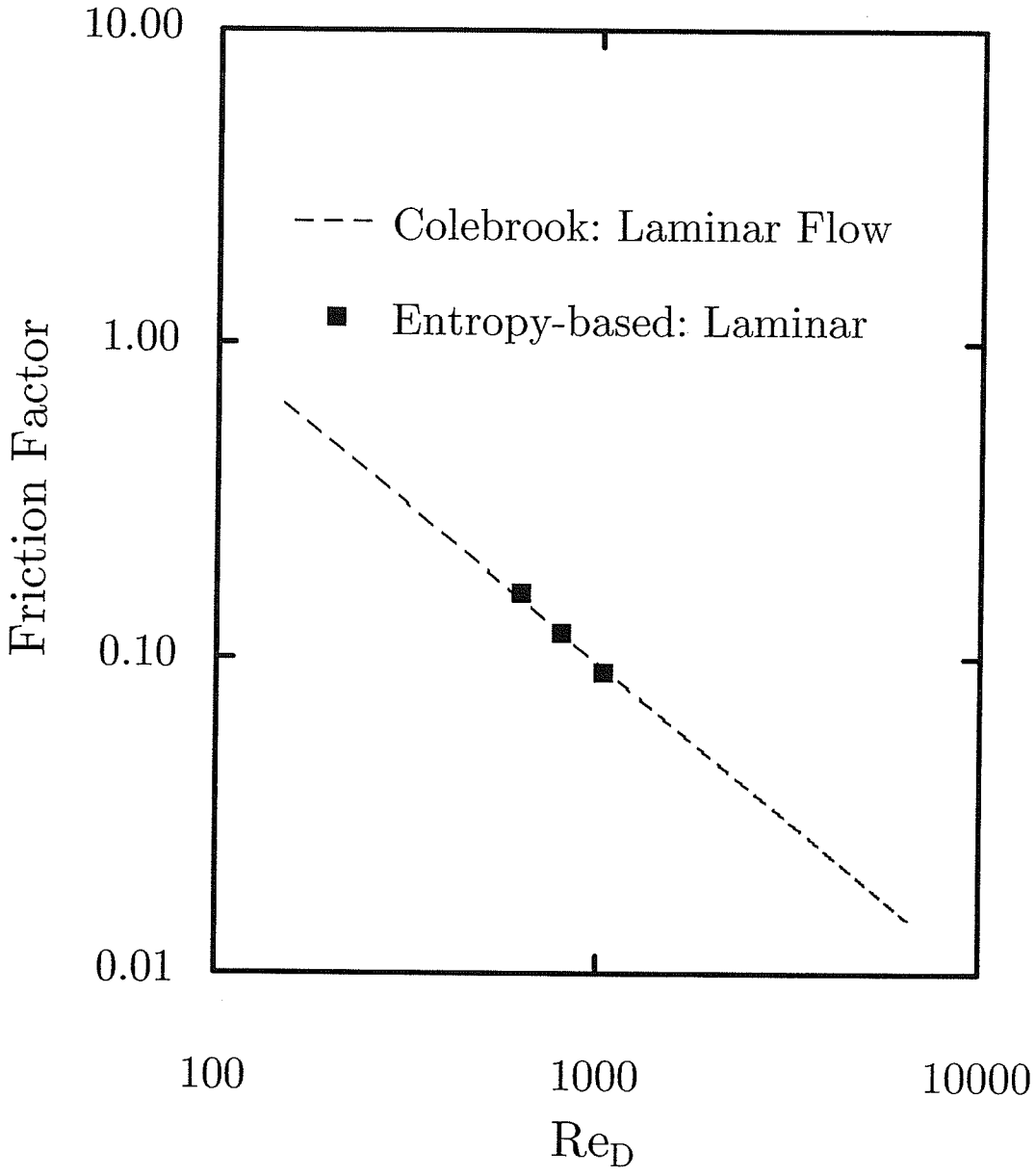

Figure 4.4: Laminar friction Factor

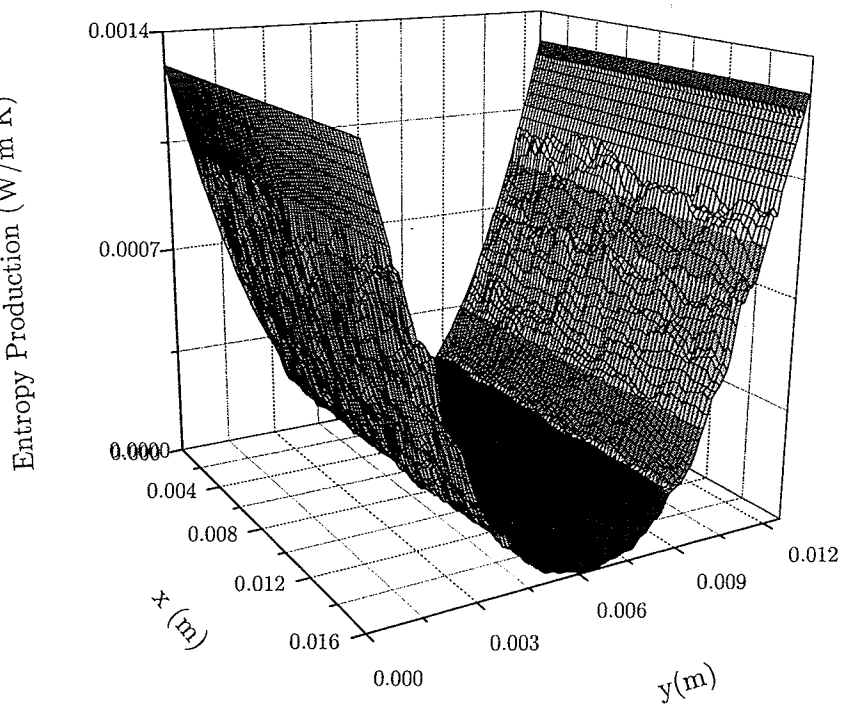

Figure 4.5: Surface plot of Entropy production at $Re_h = 518$

4.3.2 Turbulent Flow

I. Validation Problem

The newly derived formulation for mean turbulent entropy production will be validated against past DNS data. The DNS solution assumes negligible viscous dissipation in the energy equation. Therefore, attention is focused on the positive definite model involving the dissipation of turbulent kinetic energy (right side of Eq. (2.44)), since the entropy transport equation requires inclusion of the viscous dissipation in the energy equation for accurate modeling. The continuity, momentum and energy equations, with Eqs. (2.42) - (2.44), provide a complete set of relations required for a Second Law model of the dissipation of turbulent kinetic energy provided the temperature variation due to the viscous dissipation is included in the energy equation.

Turbulent flow between two parallel plates at four different Reynolds numbers, based on the friction velocity, is considered. Computations of f at $Re_\tau = 180$, 395, and 590 were based on direct numerical simulation (DNS) data of Moser et. al. [74]. The data of Kuroda et. al. [75] was used to compute f at $Re_\tau = 100$. The computed friction factors based on Eqs. (4.3) and (4.4) are compared in Table 4.1. The present results show excellent agreement with Darcy's friction factor computed from the Colebrook equation and Eqs. (4.3) and (4.4). The Colebrook equation is documented in Ref. [69]. The results are illustrated at various Reynolds numbers based on the bulk velocity in Figure 4.6. The results suggest that the present turbulence modeling of entropy production (particularly in terms of ϵ) has been accurately formulated.

Another useful validation of the new formulation is outlined in Fig. 4.7. A comparison with the Moore model is presented, in regards to the spatial distribution of entropy production in the channel. It is useful to observe that the integral value of entropy production computed from Moore's model in Eqs. (2.34) and (2.36), based

Table 4.1: Friction Factors at Different Re_τ

	Re_τ			
	100	180	395	590
f (based on τ_w)	0.0383	0.0325	0.0260	0.0232
f (based on present modeling)	0.0388	0.0324	0.0252	0.0225

on the production of turbulent kinetic energy, is within 1% of the newly formulated model. Although close agreement is achieved, the newly derived formulation of Eq. (2.44) includes additional mechanisms of turbulent entropy production, particularly involving dissipation terms. Figure 4.7 illustrates that past turbulence predictions with Moore's model give certain erroneous distributions of the mean entropy production. Moore's model under-predicts the entropy production closer to the wall and over-predicts entropy production away from the wall, before it decreases to zero in the middle of the channel. The additional curve in Fig. 4.7 shows that the viscous mean dissipation is the main component of entropy production near the wall, but other components become most significant at further distances away from the wall. In particular, the mean viscous dissipation accounts for more than 80% of the total entropy production at approximately $y^+ < 9$, where $y^+ = yu_\tau/\nu$. This percentage decreases to zero in the center of the channel.

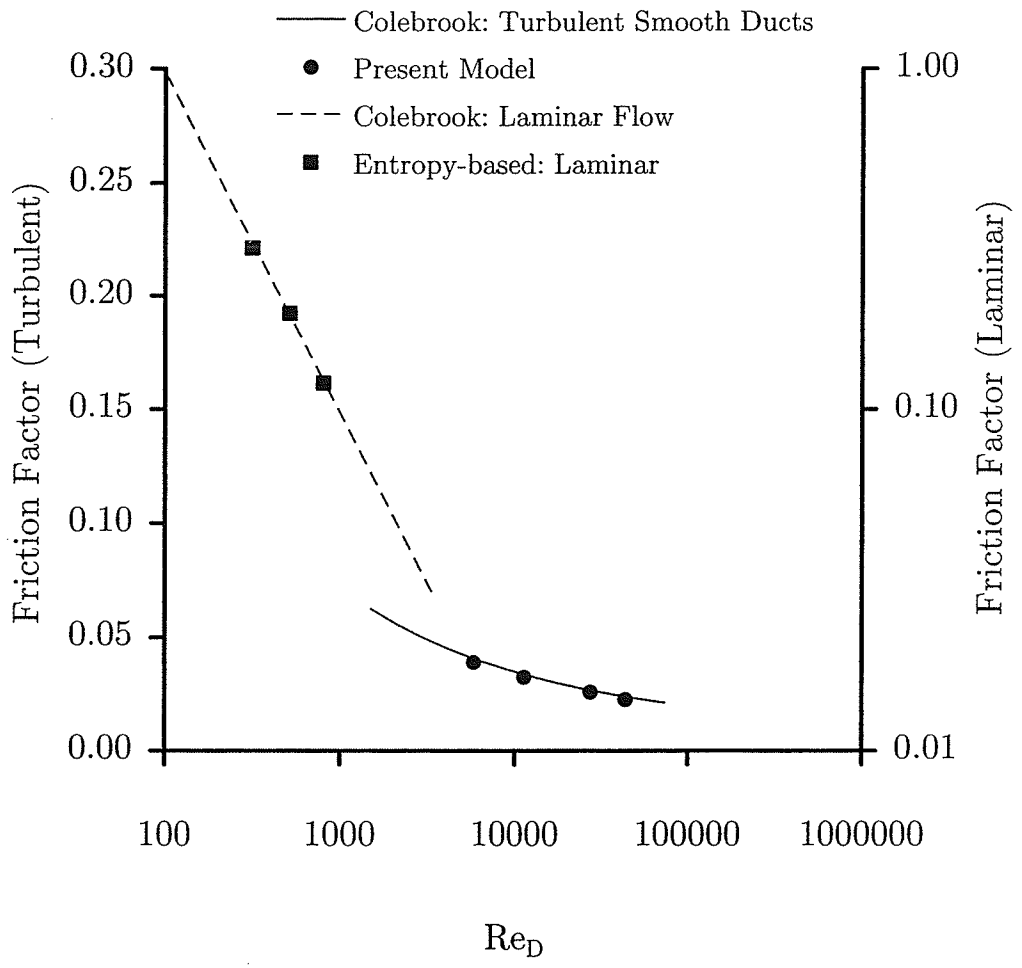

Figure 4.6: Friction factor based on present Entropy production Modeling

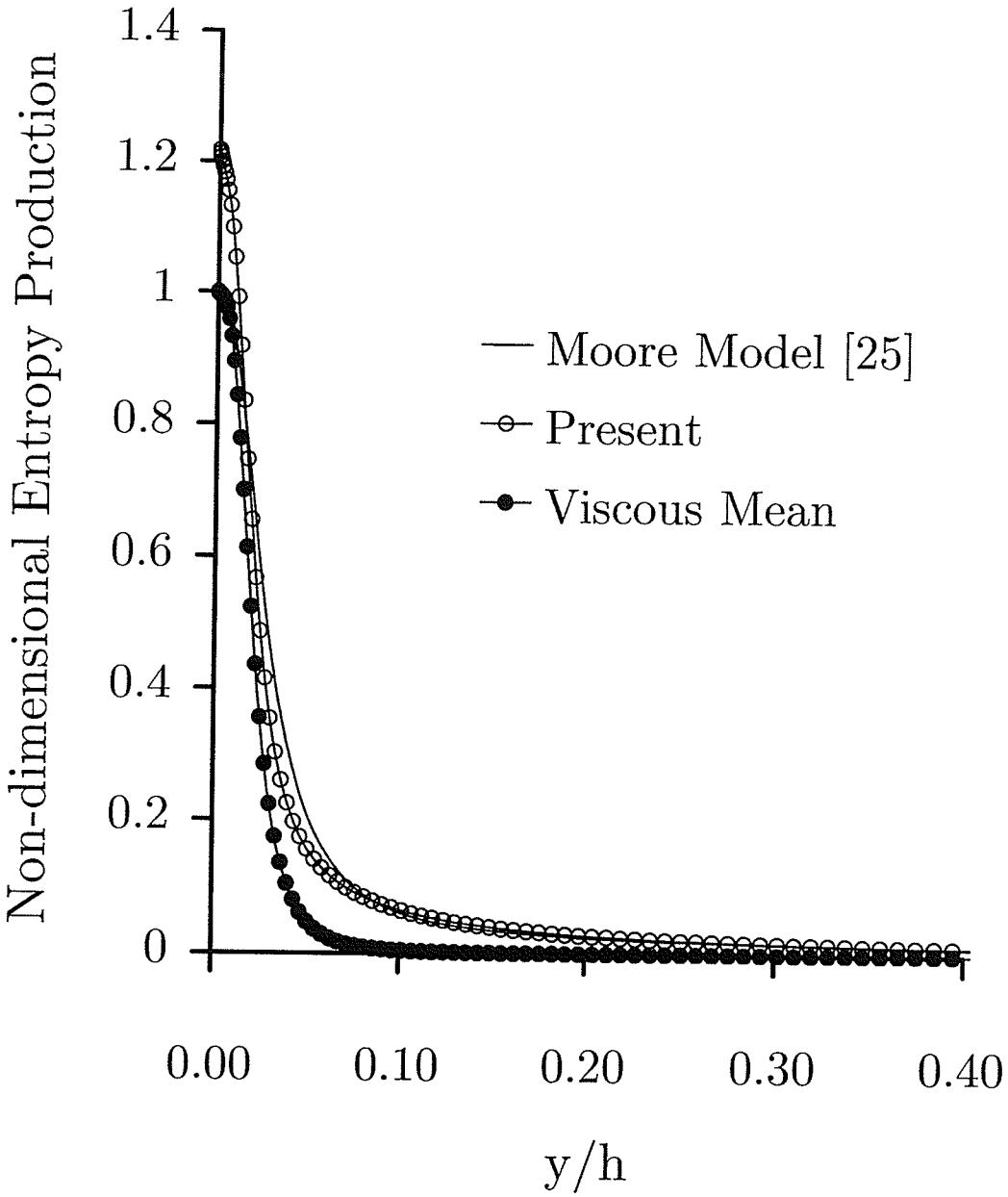

Figure 4.7: Local Distribution of Integrated Entropy Production in a Channel

II. Measurement Results

(i) Mean Velocities

In Fig. 4.8, the mean velocity profile obtained from 4000 instantaneous vectors at a cross section of the flow in the fully developed turbulent flow region is presented at $Re_\tau = 187$, 295 and 399. The velocity profiles (shown in the inset) at different transverse locations in the measurement region collapse on each another, due to fully developed conditions. The mean velocities are normalized with the centerline velocity in Fig. 4.8 and the y-coordinate was normalized with the half-channel height. Figure 4.9 shows the distribution of the mean velocity profiles in terms of wall variables. The wall shear stress was determined by the Clauser plot technique, which assumes a universal logarithmic profile in the overlap region. The experimental data confirms a stretch in the extent of the logarithmic layer, as the Reynolds number increases. The mean profiles in the $Re_\tau = 295$ and 399 cases agree out to $y^+ \approx 250$. At $Re_\tau = 187$, the standard constants ($k = 0.4$ and $B = 5.0$) give a logarithmic slope with a slight offset from a best fit ($k = 0.4$ and $B = 5.5$), in agreement with DNS data. These results are consistent with previous experimental measurements, which associate such flow behaviour with low Reynolds number effects. The spatial resolution of PIV is limited by the size of the interrogation area so measurements could not be made any closer to the wall than $y^+ = 8.18$. The data compares well with DNS results.

(ii) Turbulent Intensities

The turbulent fluctuating velocities are normalized by the friction velocity and they are plotted in Fig. 4.10 at three different cross-sections of the flow region. No systematic deviations among these profiles are observed. Figure 4.11 compares the distributions of u^+ and v^+ obtained at $Re_\tau = 187$ with the PIV results of Lui et al. [67] and

the DNS results of Kim et al. [68]. Good qualitative agreement is noted among the results. Compared with the DNS results, the peak value for the fluctuating streamwise velocity is under-predicted for the present results as 2.5 at $y^+ = 13$. The peak shows close agreement with previous PIV results of Lui et al. The present data also shows higher values that the DNS results in the channel core. This is attributed to the high background turbulence level in the water tunnel.

The fluctuating velocities are plotted against y/h in Fig. 4.12 at all Reynolds numbers investigated. Remarkably, the u^+ profiles collapse onto the $Re_\tau = 399$ curve away from the wall, at approximately $y/h > 0.36$ for $Re_\tau = 187$ and $y/h > 0.2$ for $Re_\tau = 295$. Essentially, all profiles vary linearly in Fig 4.12 for u^+ between $0.4 < y/h < 0.9$ at the three Reynolds numbers tested here and $0.2 < y/h < 0.9$ for v^+. The linear range for v^+ at $Re_\tau = 187$ is not immediately obvious. This observation is consistent with studies of Moser et al. that suggested that the collapse of the u^+ profiles to a high Reynolds number outer-layer limit appears to occur at $y^+ > 80$ [74]. No such collapse is observed when the inner variables are employed as the normalizing quantities. The qualitative trends of fluctuating velocities also compare well with the DNS data shown in the inset.

(iii) Turbulent Dissipation Rate and Entropy Production

The Kolmogorov length scale, η, estimated from its definitions and DNS data is between $6\mu m \sim 18\mu m$ at the highest Reynolds number measured and between $14\mu m \sim 33\mu m$ at $Re_\tau = 187$. The camera with extension rings captures an image approximately 9mm high. With the 32×32 interrogation, the spatial resolution of the PIV measurements is approximately 280 μm. Thus, the spatial resolution is about 16 times the Kolmogorov length scale at the channel core and 48 times close to the wall. The resolution of the velocity field is too small to accurately describe

spatial derivatives of the fluctuating velocity field and dissipation rate using the total dissipation method. Nevertheless, simplified expressions for ε and isotropic conditions can be used to estimate ε, while appreciating the effect of spatial resolution on the results. In this study, the dissipation rate has been estimated using the dimensional analysis relation (Eq. (3.16)) and the large eddy PIV approach. The SGS stress is obtained from the Smagorinsky and Gradient models. The accuracy of the estimation methods was assessed by comparisons with the DNS data of Moser et al. [74].

The measured dissipation rates are compared with the corresponding DNS solution at $Re_\tau = 187$, in Fig. 4.13. The dissipation rate in Fig. 4.13 and all subsequent figures is normalized by $(\dot{P}_s)_0 = u_\tau^4/\nu$. The estimation methods show close agreement with the numerical data and they give correct distributions of the turbulent kinetic energy in the channel. A high dissipation region is concentrated near the wall. The DNS data reveals an inflection point, not captured by PIV closer to the wall at $y^+ = 12$. The dissipation rate is minimum in the center of the channel and it becomes the only mechanism for energy loss in the channel centerline for turbulent flows. Greater deviation from the DNS result is noticed for all estimation methods closer to the wall, due to the anisotropic nature of the flow and smaller dissipation length scales in this region.

Dissipation rates computed from the DNS results of Kuroda et. al. [75] at $Re_\tau = 100$ and Moser et. al. [74] at $Re_\tau = 180$, 395 and 590 are plotted in Fig. 4.14. In Fig. 4.15, the dissipation rate has been estimated using the dimensional analysis relation at all Reynolds numbers investigated. The integral length scale, l, is defined as the distance from the wall to a point where the streamwise velocity is 99% of the centerline velocity. Also, A is taken to be 1.2. The DNS results suggest lower values of ε in the middle, with higher values at the wall and steeper gradients as the Reynolds number increases. The dissipation rate shows similar trends in the wall layer in Fig.

4.15. On the contrary, the core region shows higher dissipation rates with increasing Reynolds numbers. The dissipation rate is under-predicted closer to the wall at all Reynolds numbers.

The large eddy PIV dissipation estimates in Figs. 4.16 and 4.17 have a more regular distribution with values predicted by DNS as Re increases. The filter size for the correlation analysis is $\Delta = 280\mu m$ while the integral length scale, $l \approx 8mm$ at $Re_\tau = 187$. As stated earlier, the Kolmogorov length scale is $\eta = 18\mu m$ at the channel centerline. Thus $\Delta \ll l$ and the filter size is sufficiently larger than the Kolmogorov length scale to warrant the use of the large eddy PIV method. The dissipation rate closely agrees with the DNS result at low Reynolds numbers, but it is under-predicted at higher Reynolds numbers.

One would expect better performance with increasing Reynolds numbers, since the flow shows higher tendencies towards local isotropy as the Reynolds number increases. This discrepancy is partly due to the overall accuracy of the PIV measurement at high Reynolds numbers. At high Reynolds numbers, the PIV dynamic range required to accurately resolve the smaller Kolmogorov length scales becomes very high and the spatial resolution of the PIV fails to capture certain aspects of the flow structure. Better performance of all estimation methods at $Re_\tau = 187$ can be attributed to larger Kolmogorov length scales and a consequent higher flow resolution. The dissipation rate cannot be measured closer to the wall than $y/h \simeq 0.2$, due to reflections and poor accuracy of the velocity close to the wall at high Reynolds numbers. The two SGS models show similar predictions, suggesting a weak dependence of the large eddy PIV method on the SGS stress model.

Measured oscillations are effectively reduced through filtering of velocity data. In Fig. 4.18, a 3×3 average filter was used for smoothing of the validated velocity vectors, before calculating the viscous dissipation. The viscous dissipation has been

normalized by $(\dot{P}_s)_0$. A comparison of the experimental data with DNS results is presented in Fig. 4.19, in regards to the spatial distribution of the mean viscous dissipation and the total entropy production at $Re_\tau = 187$. All three estimation methods agree closely. The entropy production has been scaled by $\rho u_\tau^4 T/\nu$. A high entropy production region is evident close to the wall.

The distribution of turbulent kinetic energy dissipation is plotted as a percentage of the total mechanical energy loss in Fig. 4.20 to provide a Second Law insight into the energy requirement of turbulence in wall bounded flows. The measured results show close agreement with the DNS results at $Re_\tau = 187$. The percentage of turbulent kinetic energy decreases from a maximum at the channel centerline to approximately 14% of the total mechanical energy loss just outside of the logarithmic region, towards the wall. The percentage of ε^+ is fairly constant in the outer region and logarithmic layers. This distribution implies that the viscous stress due to the molecular viscosity dominates at the wall. Unlike laminar flow, where the viscous shear stress increases linearly across the fluid layer from the channel center to the wall and entropy production is distributed evenly over the entire channel, the viscous stress is concentrated to a region between the buffer layer and the wall in turbulent flows, thereby leading to a much higher mean shear and entropy production at the wall. Thus, this explains the need for higher pumping power in turbulent flows to drive fluid through a duct for the same laminar flow rate.

The equivalence of the local loss accounting approach with the traditional global loss characterization can also be demonstrated for turbulent flows, as with laminar flows. However, data extrapolation at the wall is avoided in this turbulent flow case, as the data holes at the wall consist of more than six interrogation areas and several Kolmogorov length scales apart. Such synthetic treatment of a complex turbulent structure may lead to an erroneous interpretation of data and dubious estimation

of the energy loss. It suffices to show that the PIV based loss mapping gives correct quantitative and qualitative trends of the energy losses in wall-bounded flow, as illustrated in Fig 4.19.

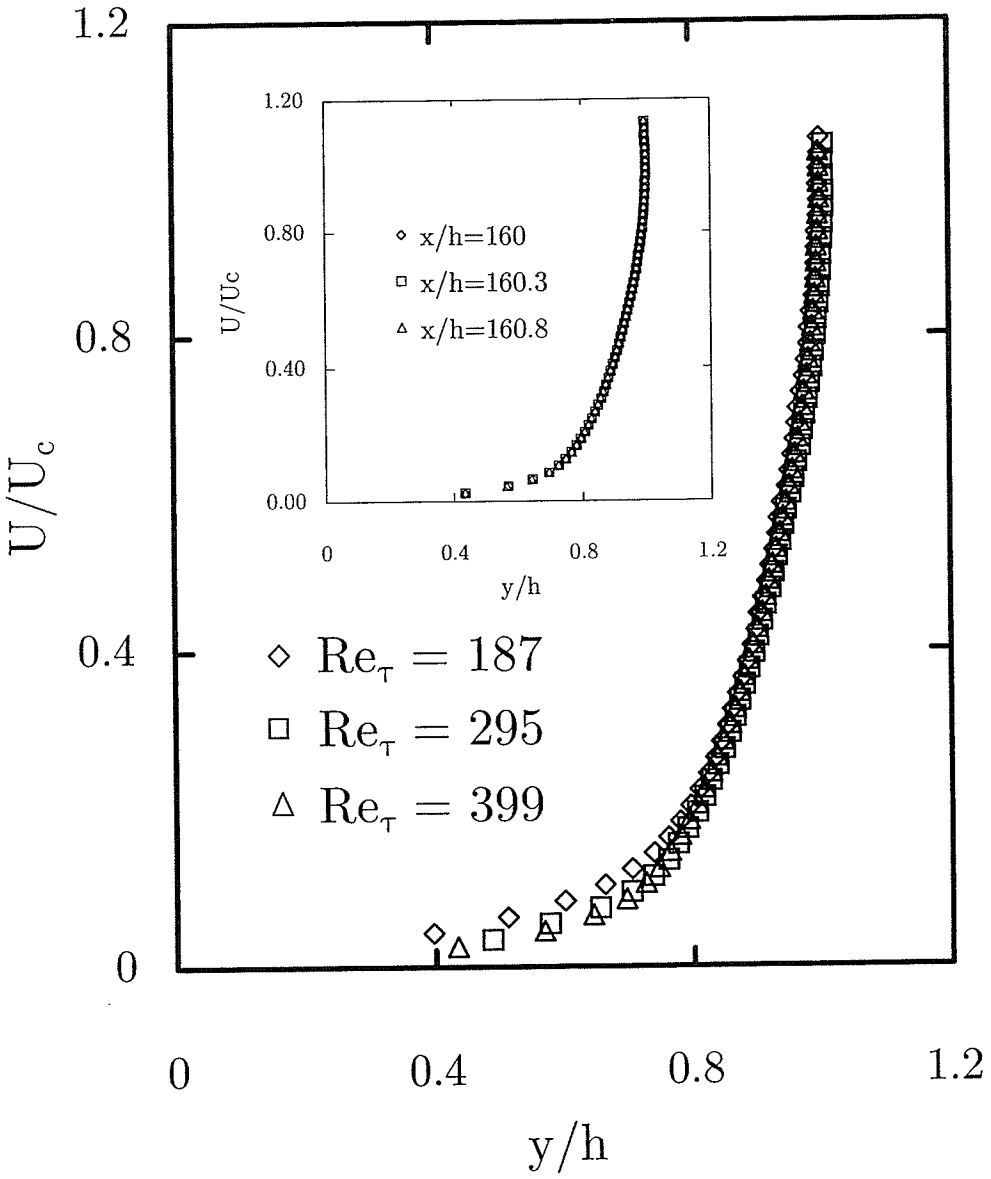

Figure 4.8: Mean velocities

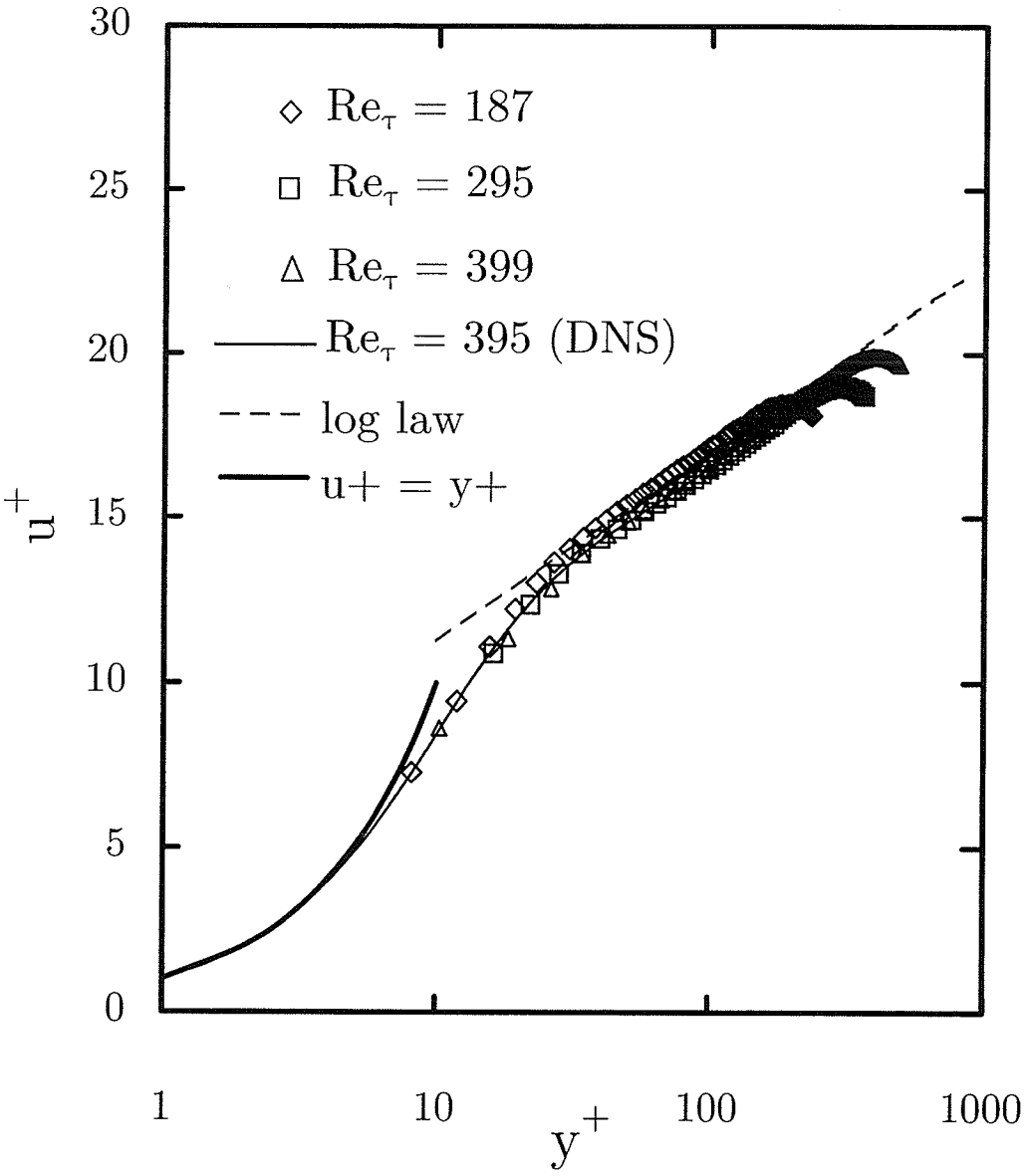

Figure 4.9: Mean velocities normalized by inner variables

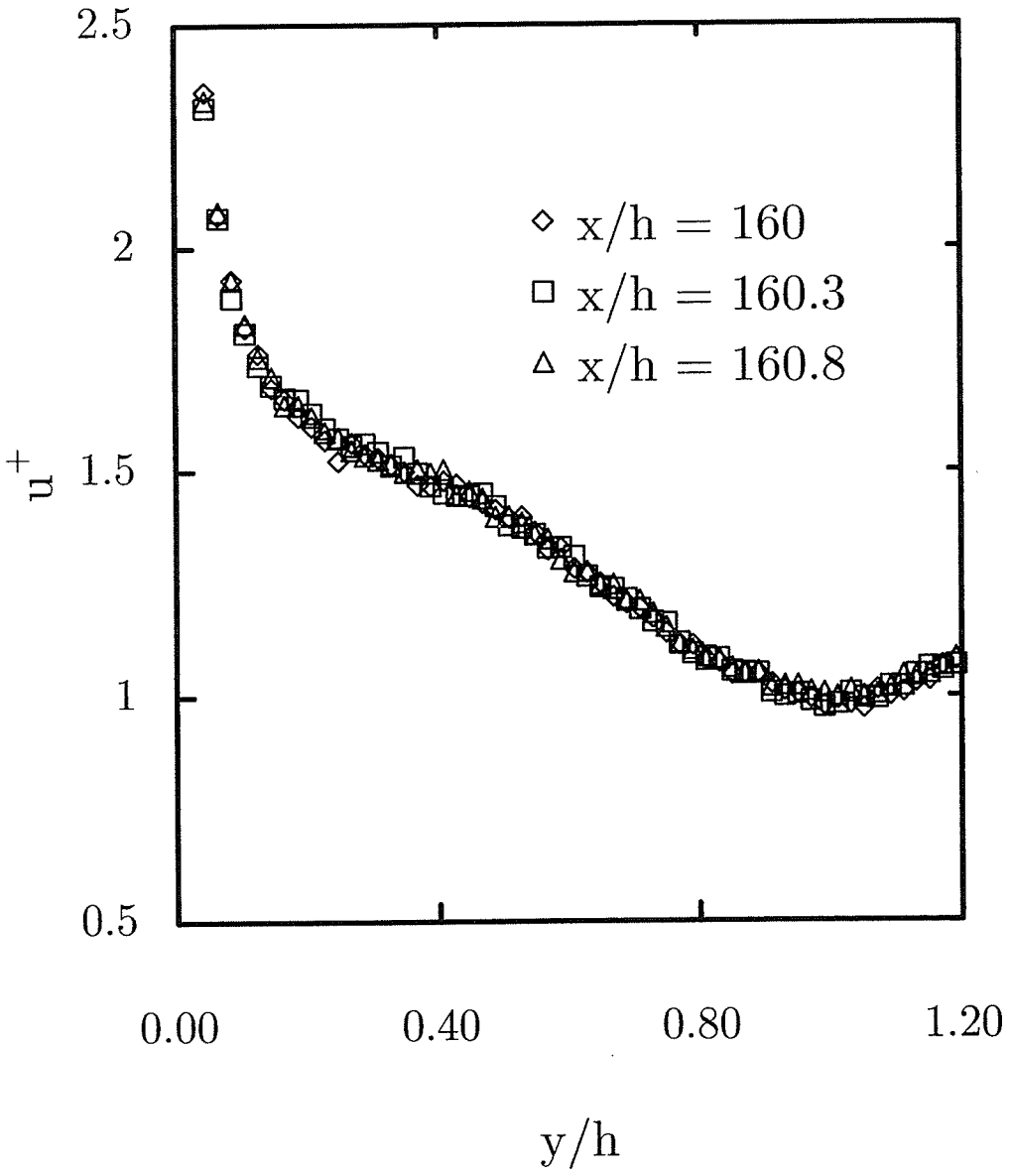

Figure 4.10: Turbulent Intensities at $Re_\tau = 399$

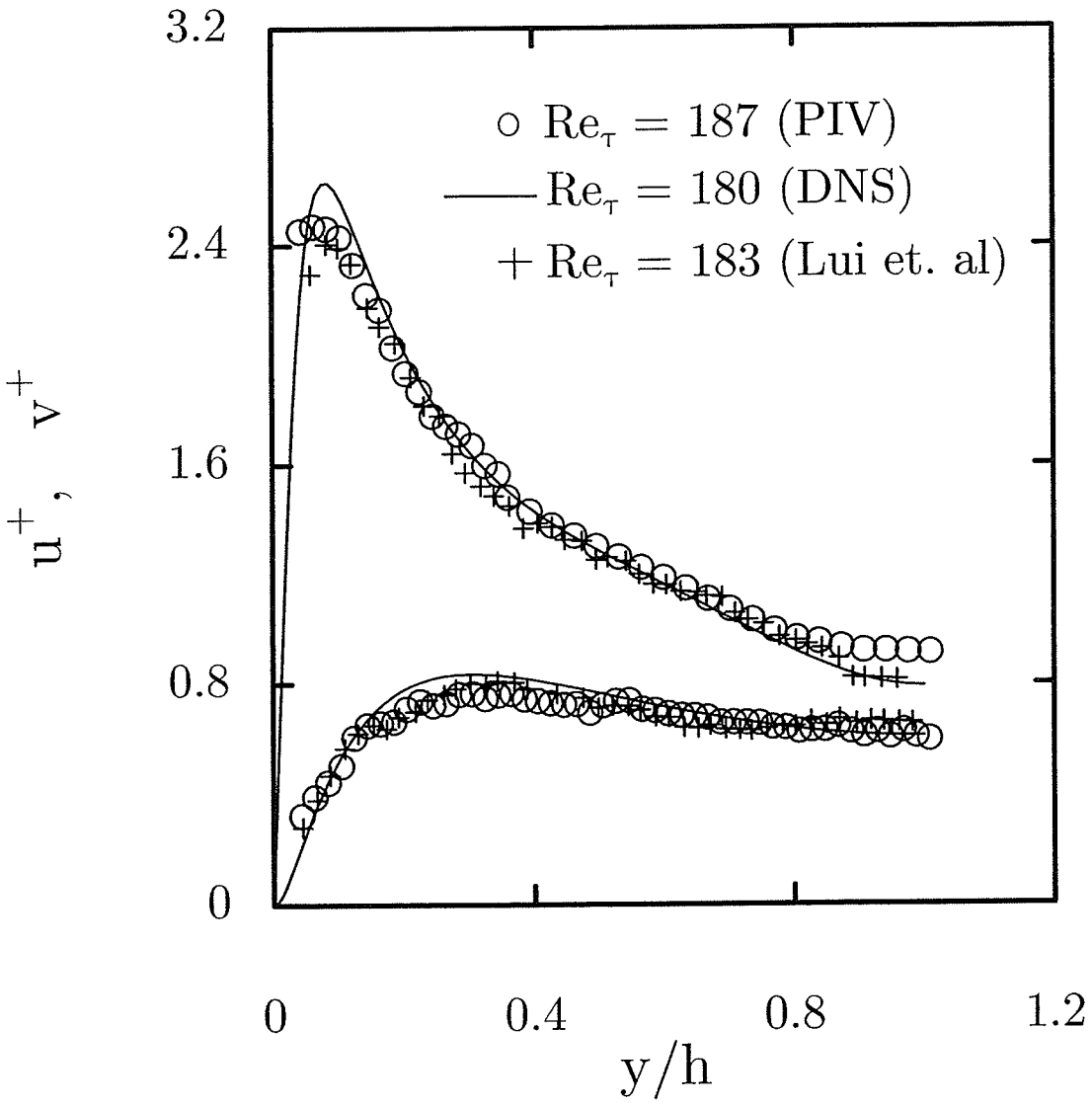

Figure 4.11: Turbulent Intensities at $Re_\tau = 187$

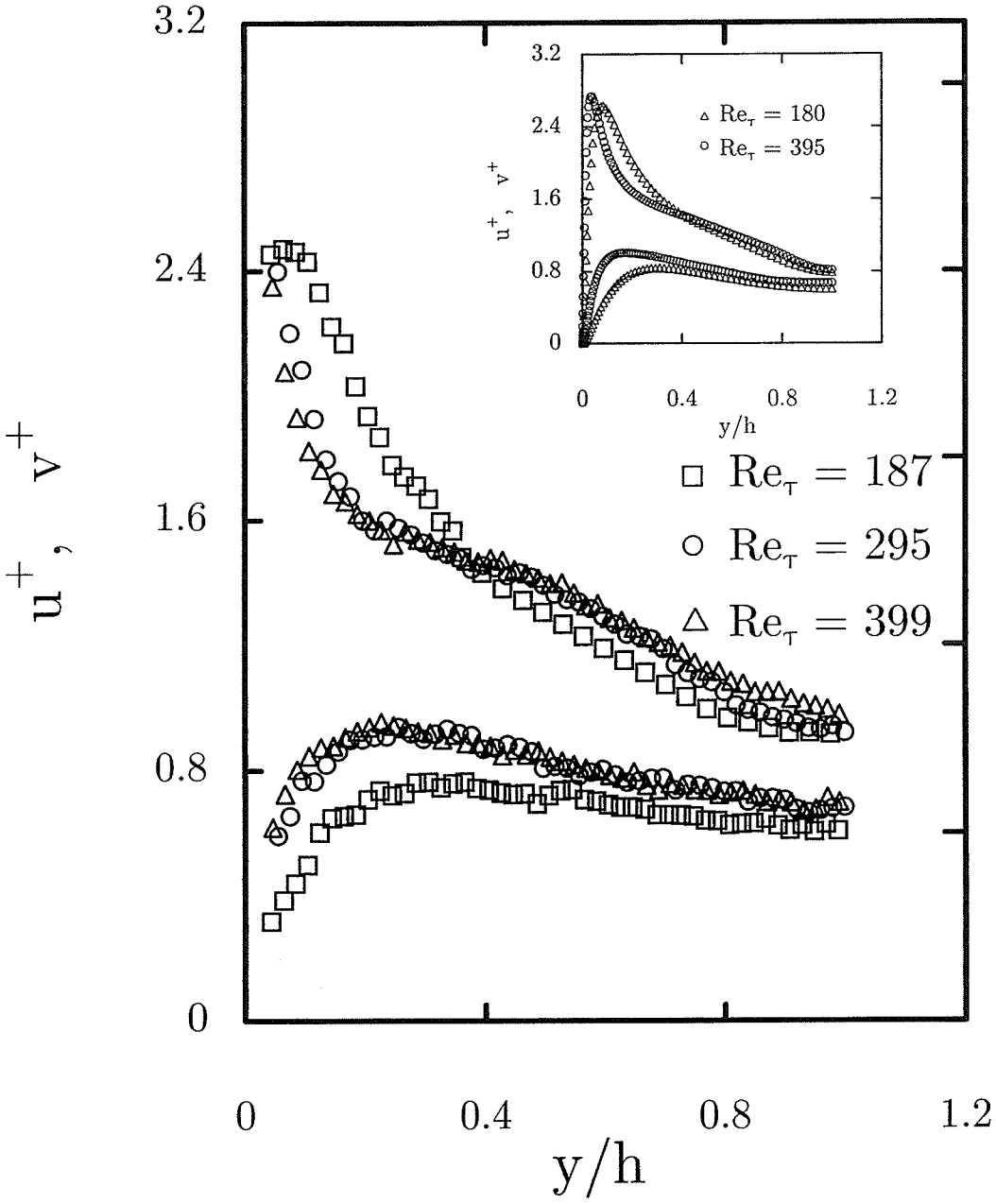

Figure 4.12: Turbulent Intensities plotted in outer variables

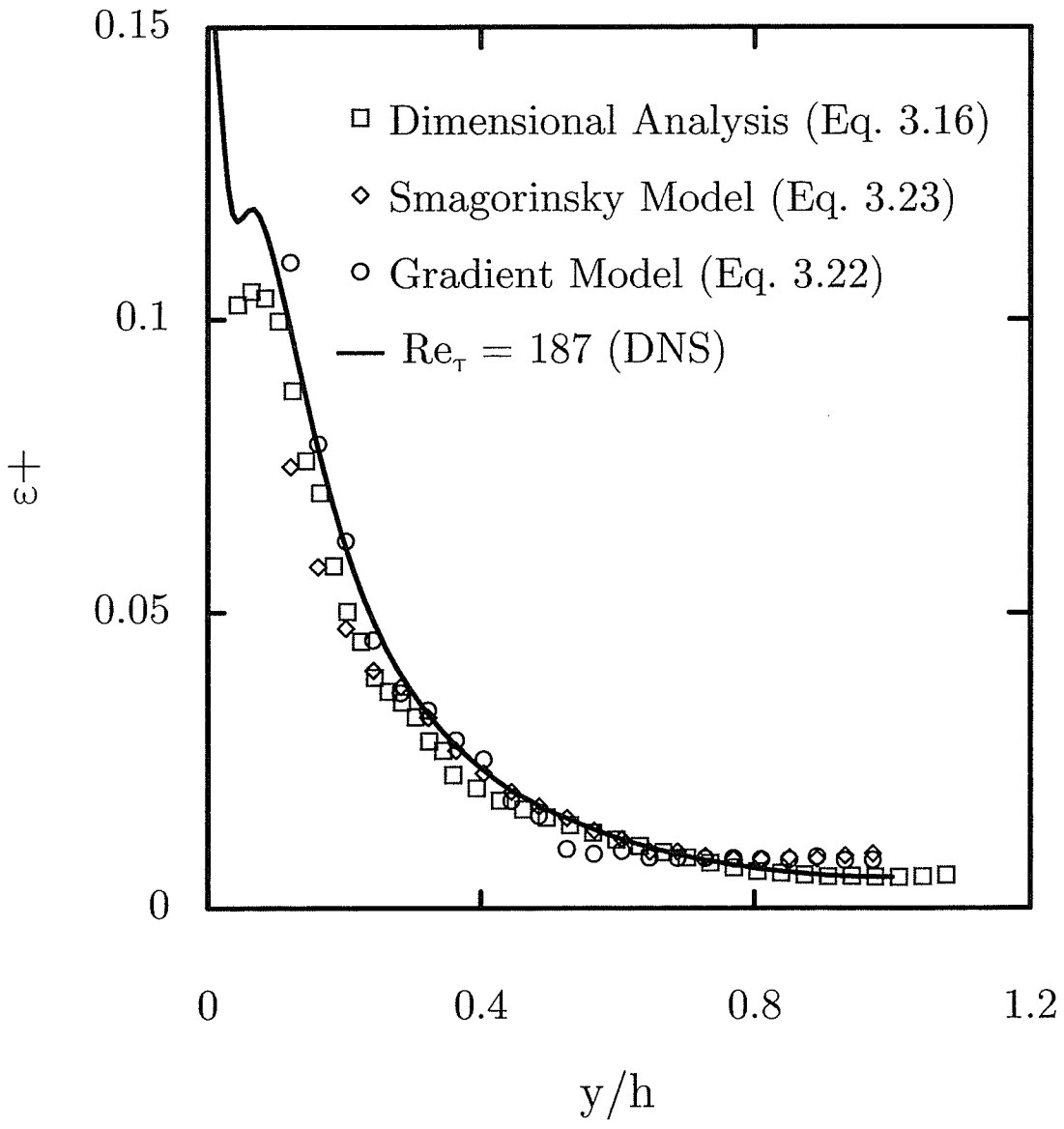

Figure 4.13: Dissipation of Turbulent Kinetic Energy at $Re_\tau = 187$

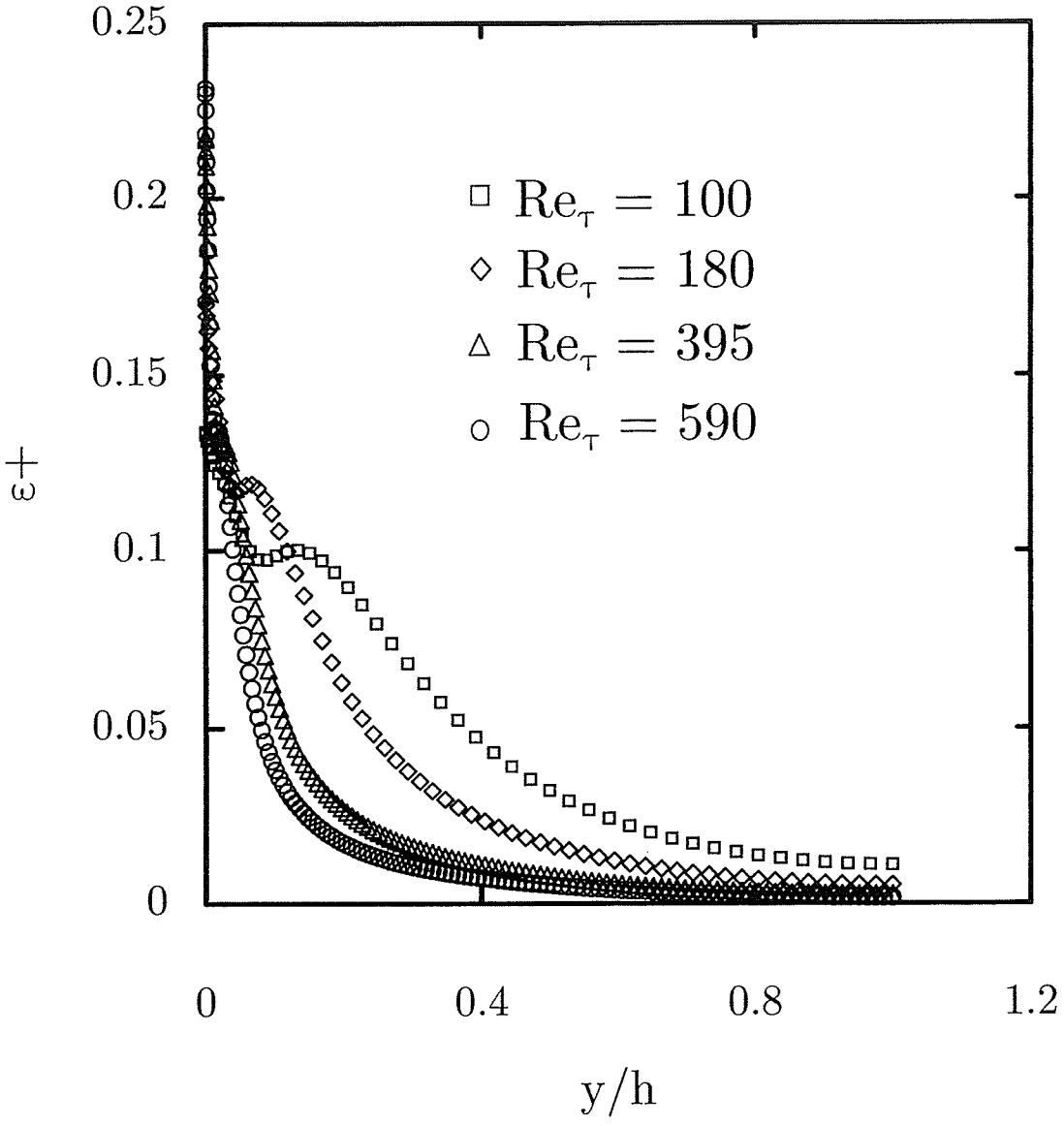

Figure 4.14: Direct Numerical Simulation Results

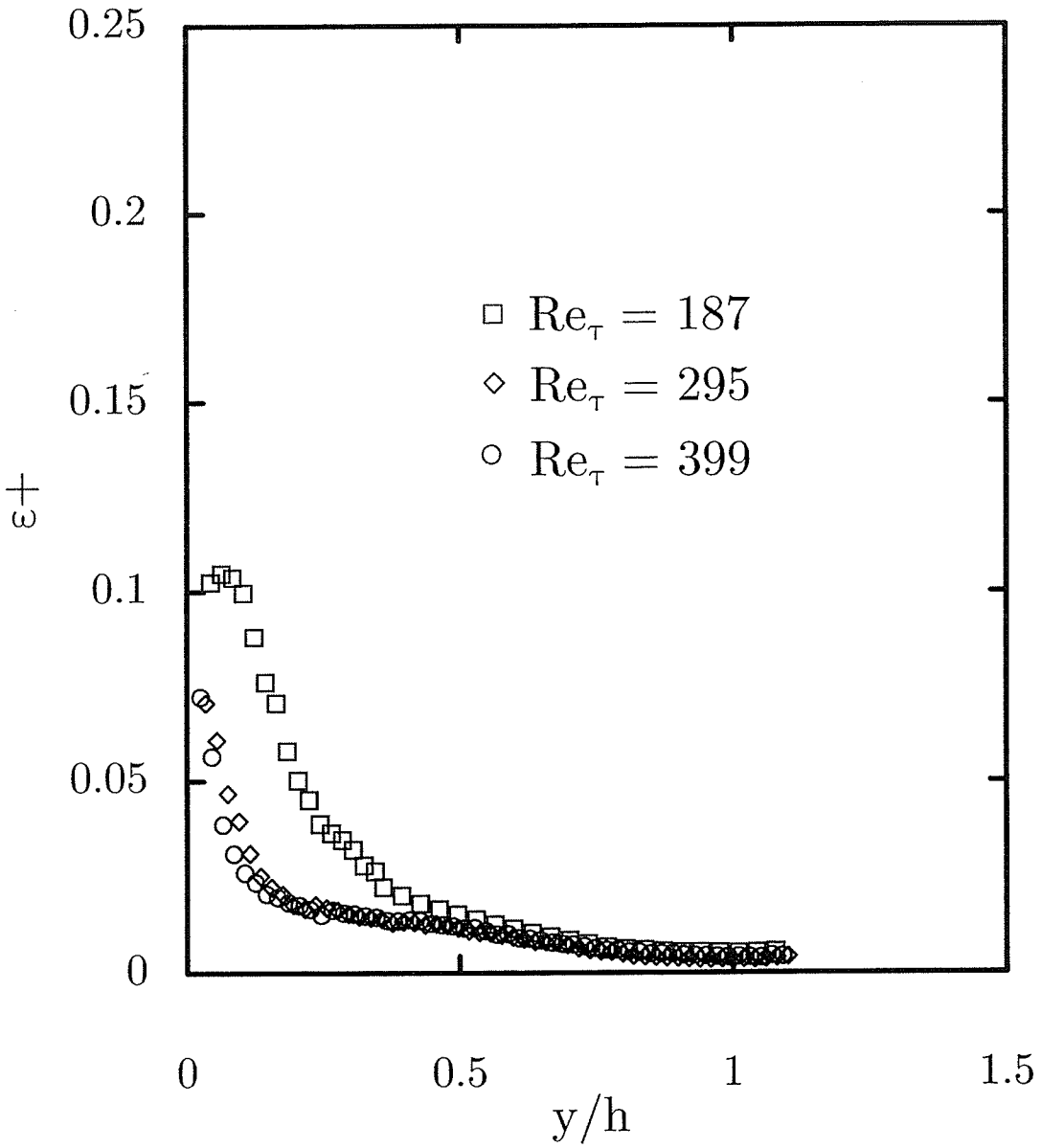

Figure 4.15: Dimensional analysis based ε estimation (Eq. 3.16)

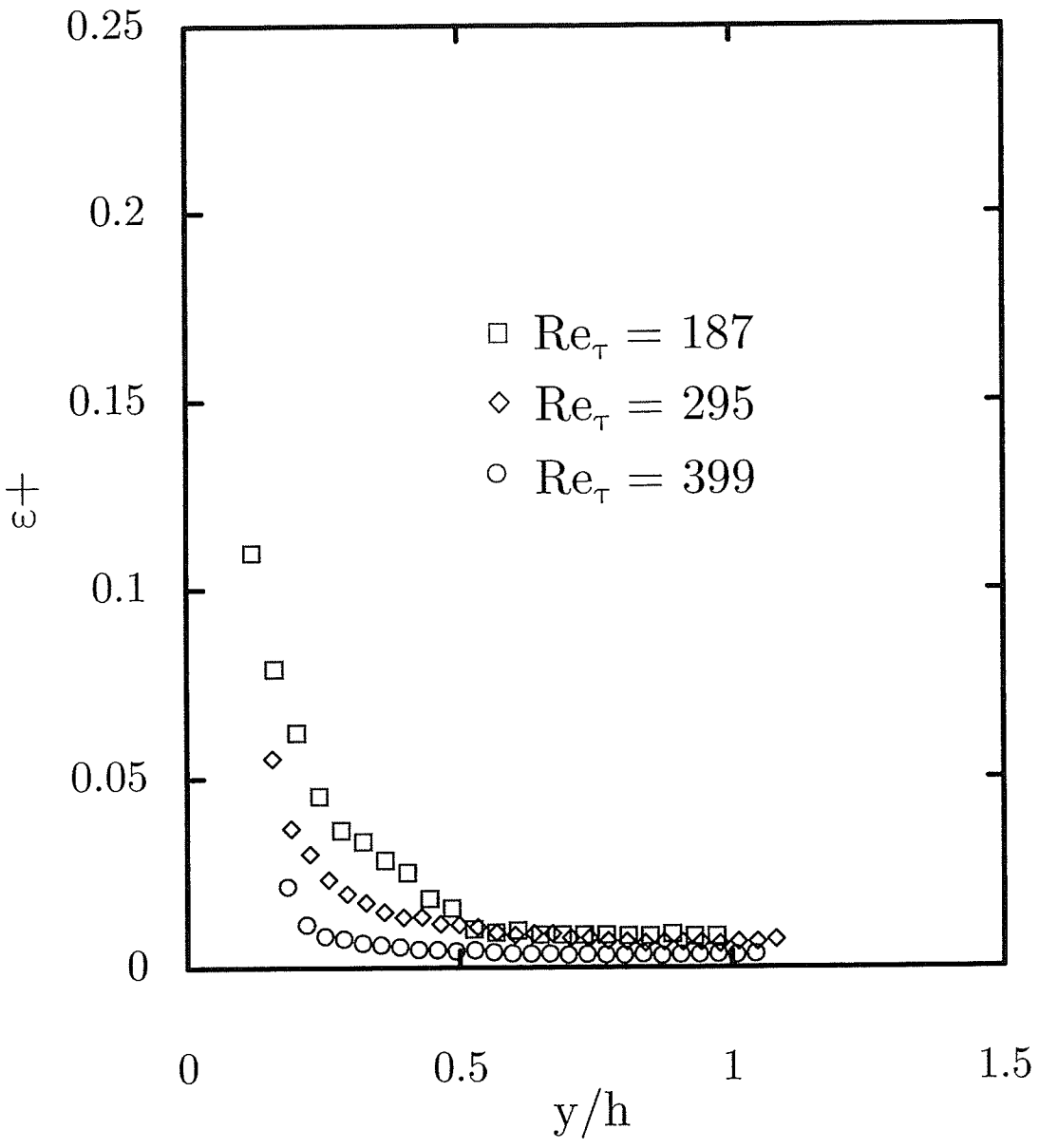

Figure 4.16: Large eddy PIV based ε estimation with Smagorinsky SGS Model (Eq. 3.19, 3.23)

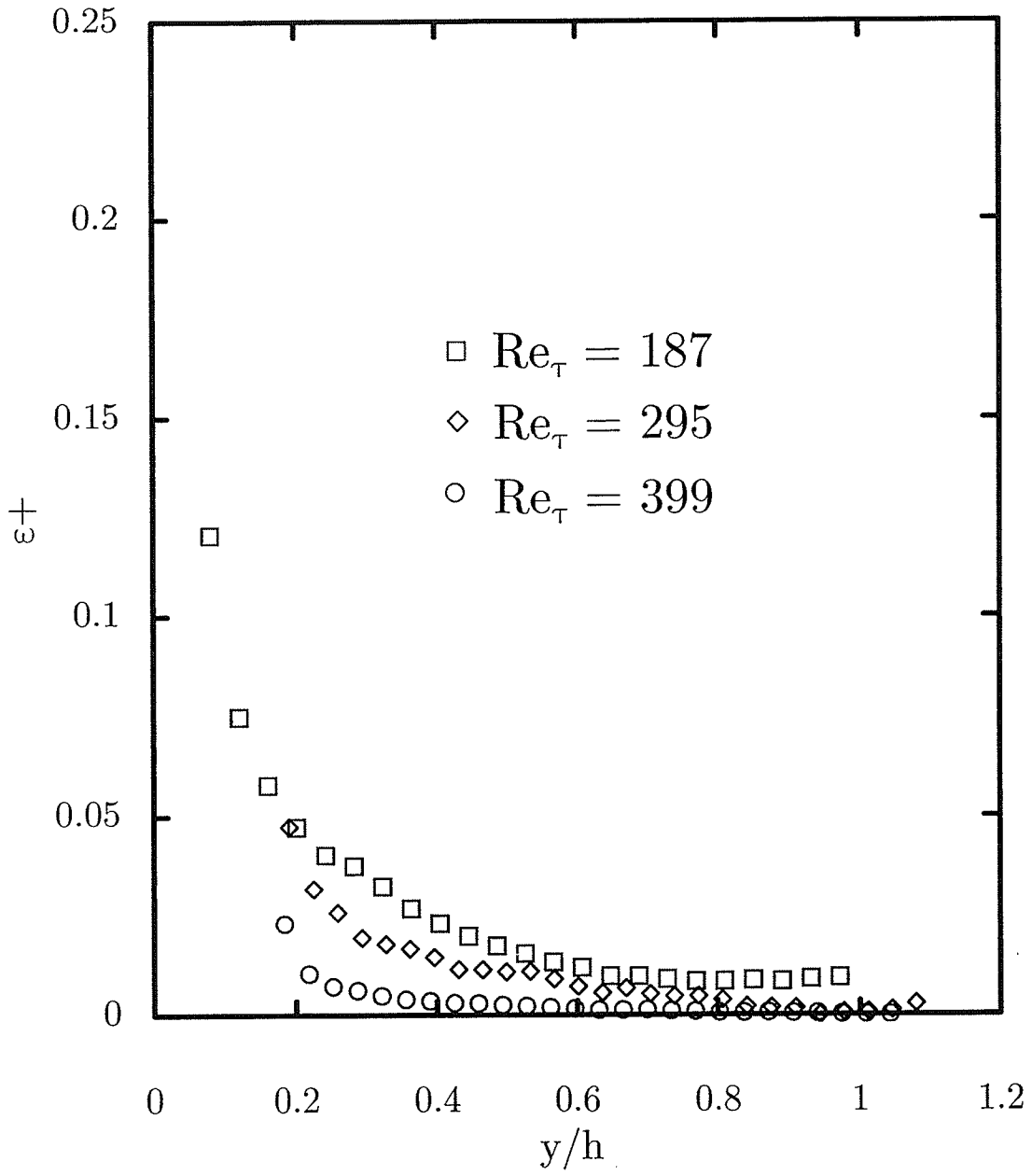

Figure 4.17: Large eddy PIV based ε estimation with Gradient SGS Model (Eq. 3.19, 3.22)

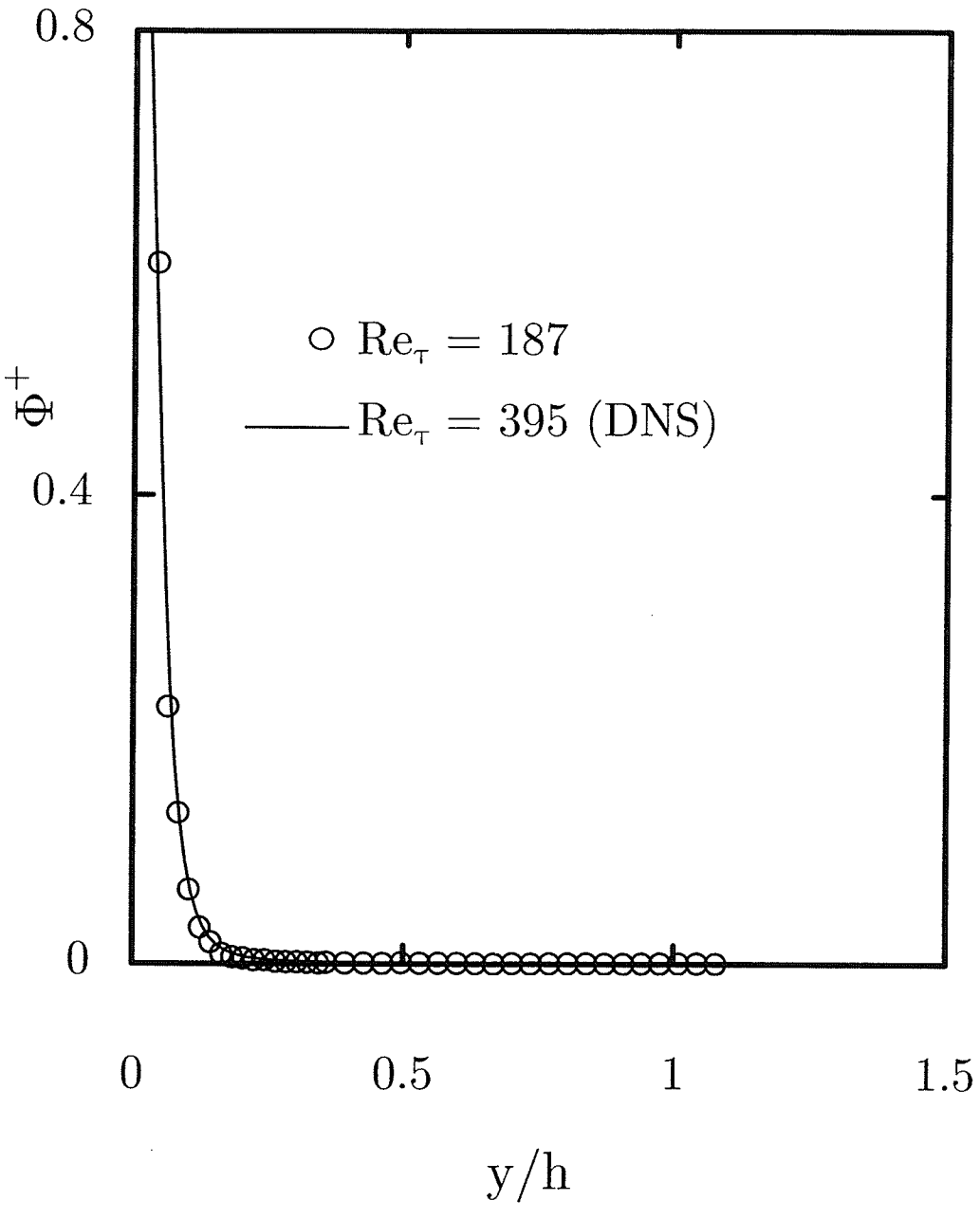

Figure 4.18: Viscous dissipation at $Re_\tau = 187$

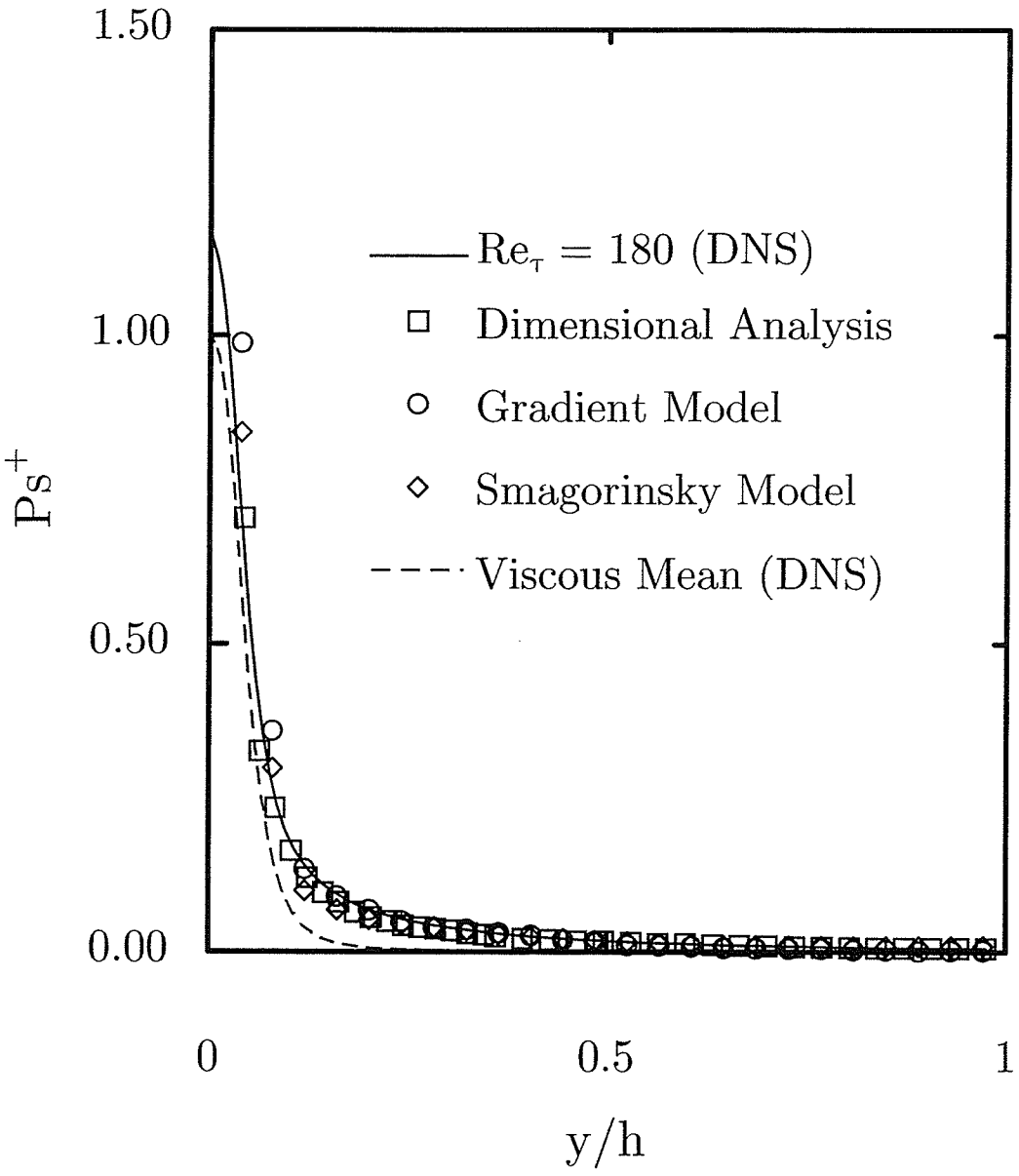

Figure 4.19: Turbulent Entropy Production at $Re_\tau = 187$

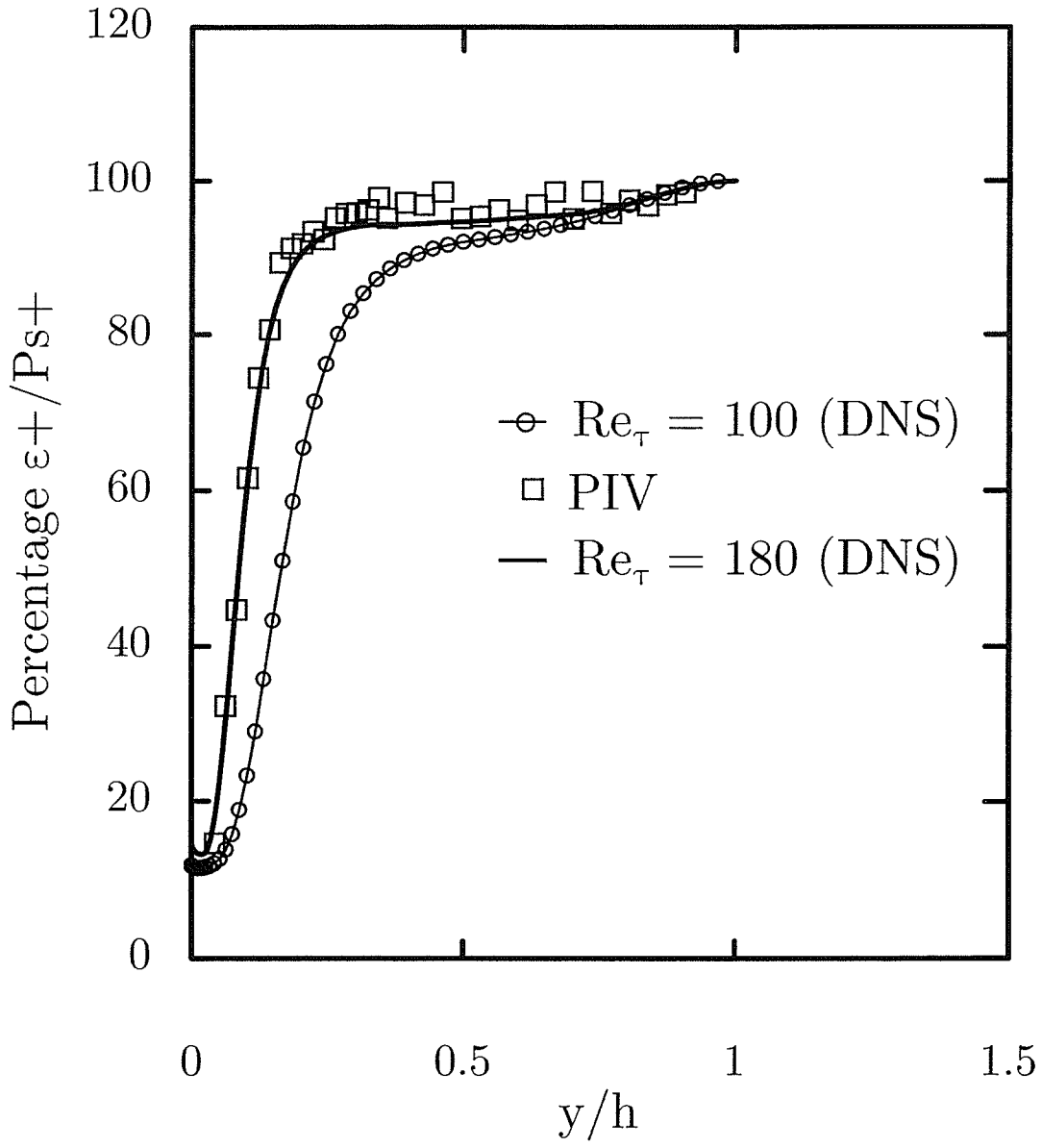

Figure 4.20: Percentage of ε^+ in total entropy production across the channel at $Re_\tau = 187$

Chapter 5

Case Study 2: Entropy Production with Free Convective Heat Transfer

Free convection heat transfer in enclosures occurs in various engineering systems. For example, cooling of microelectronic assemblies involves natural convection. Heating/ventilation in buildings, heat transfer between panes of glass in double-pane windows, solar collectors and gas-filled cavities surrounding a nuclear reactor core are other examples. Although the physical processes of free convection have been widely documented in the literature, fewer studies have considered the related importance of irreversibilities in such applications. A specified rate of heat transfer can be achieved, but with varying levels of fluid irreversibilities, depending on the surface area and temperature difference across which heat transfer occurs. For example, convective cooling of a microelectronic assembly entails free convection from the heat sink, but pressure losses occur with forced convection of air past internal components. In this instance, each unit of entropy produced (or exergy destroyed) leads to a corresponding unit of heat flow which is desired to be removed, but cannot be removed due to entropy production. This entropy production leads to pressure losses and kinetic energy dissipated to internal energy, which works against the desired objective of

component cooling.

5.1 Problem Formulation

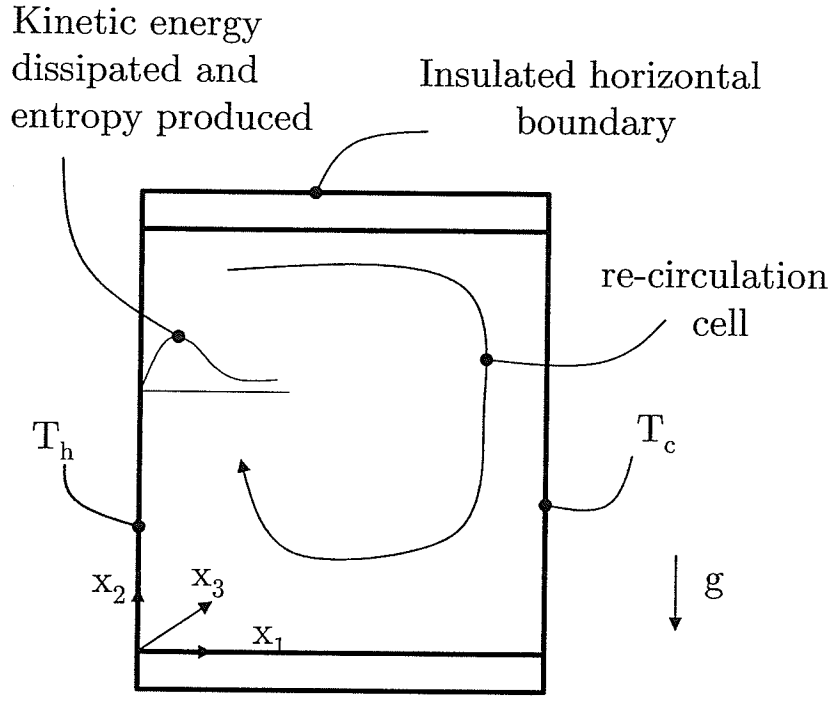

Figure 5.1: Problem Schematic

Consider free convection within a square enclosure, as depicted in Fig. 5.1. It is assumed that the cavity is sufficiently wide in the direction perpendicular to the plane of Fig. 5.1, so the buoyancy-induced fluid motion is considered to be two-dimensional. For steady-state free convection problems, Eqs. (2.2) - (2.4) become

$$\frac{\partial}{\partial x_j}(\rho u_j) = 0 \tag{5.1}$$

$$\frac{\partial}{\partial x_j}\left(\rho u_j u_i\right) = -\frac{\partial p}{\partial x_i} + \frac{\partial}{\partial x_j}\left(\mu \frac{\partial u_i}{\partial x_j}\right) + \left(\rho - \rho_0\right) g_i \tag{5.2}$$

$$\frac{\partial}{\partial x_j}\left(\rho u_j T\right) = \frac{\partial}{\partial x_j}\left(\frac{k}{c_p}\frac{\partial T}{\partial x_j}\right) \tag{5.3}$$

where ρ is the density and u_i and x_i are the Cartesian velocity components and coordinate directions, respectively. Also, g_i is the component of the gravity acceleration vector in the x_i-direction. The last term in Eq. (5.2) represents the buoyancy force, according to the Boussinesq approximation. The temperatures of the hot and cold vertical walls are T_h and T_c, respectively. The top and bottom walls are insulated. The thermophysical properties are assumed to be isotropic and independent of temperature.

Previous studies have shown that numerical solutions involving free convection in an enclosure can be successfully obtained by finite differences, finite volumes or finite elements [76, 77, 78, 79]. The buoyancy term depends on the local temperature, thereby requiring coupled flow solutions with the energy equation. Past benchmark solutions provide useful data regarding validation of predictive models for variations of flow patterns and heat transfer [76, 77]. Entropy based models have also been applied to optimization in applications involving natural convection in an inclined enclosure [80], irreversibilities at the onset of natural convection in a rectangular cavity [81] and laminar natural convection over a heated rotating cylinder [82]. In contrast to these past studies, this chapter develops a new procedure for measuring such local production rates, thereby providing a new useful tool for validating past numerical predictions and designing free convective systems.

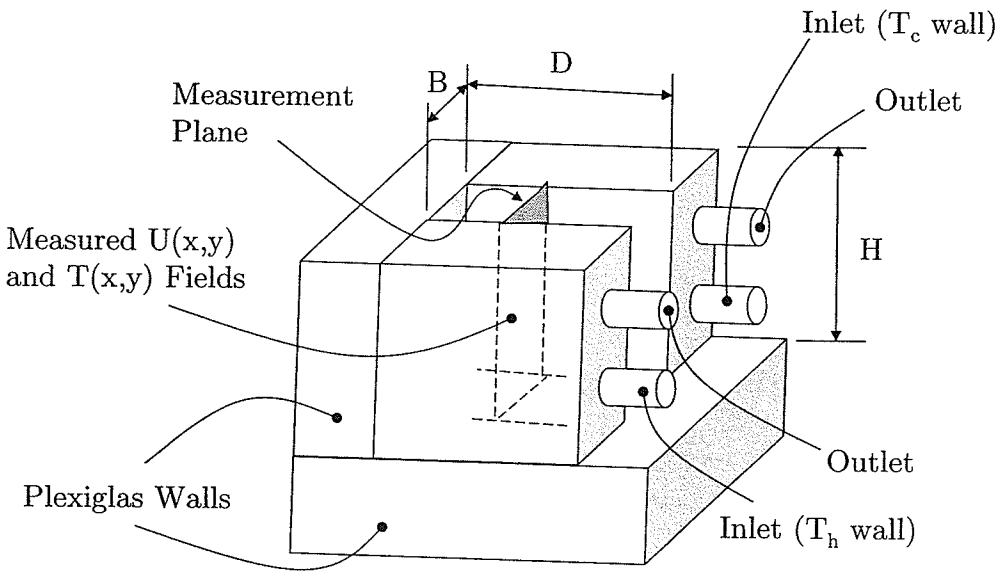

Figure 5.2: Test Cell (B = H = 39mm; D = 59mm)

5.2 Experimental Design and Measurement Procedure

(i) Experimental Setup

The experimental setup involves Planar Laser Induced Fluorescence (PLIF) for measuring temperatures within the test cell, as well as Particle Image Velocimetry (PIV) for velocity measurements (see Figs 5.2 - 5.3). The test cell in Figure 5.2 was constructed with two aluminum multi-pass heat exchangers at the side walls, connected to temperature control units (NESLAB RTE140 Bath/Circulator). Also, 17.5mm plexiglass windows were assembled on the bottom, top, back and front faces. The test cell cross-section (39 × 39 mm) was designed for laminar free convection. The test cell depth is 59 mm. Heat losses from front and back sides of the cavity may lead to velocity variations in the x_3-direction. However, the depth was designed to

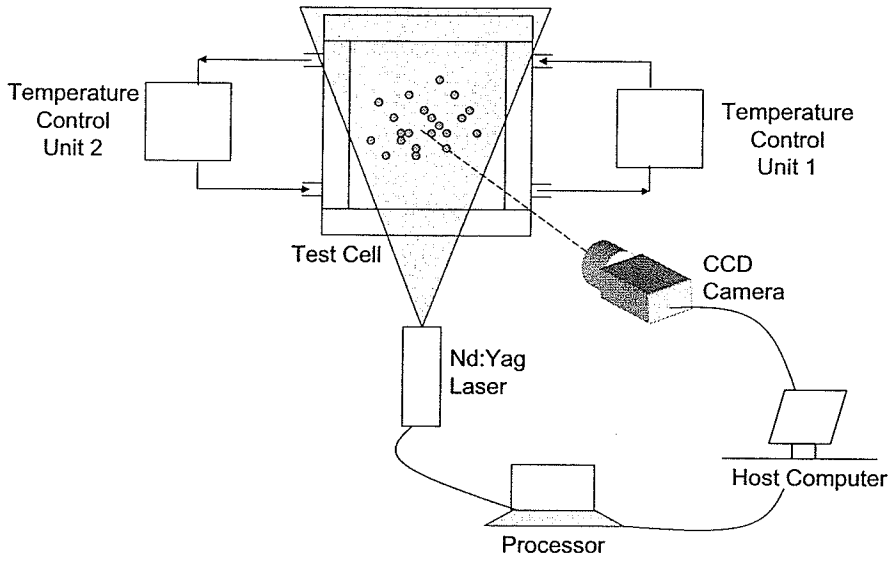

Figure 5.3: Experimental Setup

minimize these three-dimensional variations of thermal and flow fields along the plane of symmetry [83]. Two holes on the top walls were needed to fill and drain the liquid during experiments. Water at a known temperature was circulated between each aluminum heat exchanger from two NESLAB temperature baths. The temperature difference between the inlet and outlet of the aluminum cross-flow exchanger was approximately 0.3°C. In the flow loop, the cooling water was circulated by a pump between the water and heat exchangers. The temperature of the outer surface of the aluminum heat exchanger was approximately equal to the temperature of the circulating water.

(ii) PLIF Calibration

Calibration experiments for the PLIF method were performed in the cavity. Dis-

tilled water was circulated and seeded with a solution of Rhodamine B at a known concentration and temperature. Preliminary calibrations were carried out at a fixed energy levels to determine the optimum concentration, C_{max}, at which the resolution of the temperature field is maximum, while maintaining linearity between intensity and temperature. The variations of gray values in the preliminary experiments at various concentration levels are shown in Fig. 5.4. As expected, the calibration indicates that the intensity of the fluorescence decreases monotonically with temperature at a fixed rate. The spatial gradient of gray value with temperature represents the PLIF resolution.

In Figure 5.4, the temperature resolution is maximum for a concentration of $15\mu g/L$. In the final calibration shown in Fig. 5.5, the concentration was fixed at approximately 89% of the concentration at which the slope of the temperature vs. intensity resolution graph is maximum, i.e., $C_o = 0.89 \times C_{max} = 13.5\mu g/L$. Two energy levels were considered to account for the response of the camera to varying laser energy levels.

Values of temperature at discrete locations in the measurement domain are obtained using the final calibration map. The PLIF software (Dantec Dynamics) used in this thesis includes several methods for advanced analysis of the PLIF results. Statistical averages are available to establish whole-field statistics on the LIF data acquired. Optimization methods are used to enhance the signal to noise ratio and precision, thereby giving an absolute theoretical temperature accuracy of $\pm$ 0.6 ^{o} C.

(iii) Data Reduction and Processing

The cavity was illuminated from above at the vertical plane of symmetry by a Nd:Yag pulsed laser. A Dantec Hisense CCD camera captured the sequence of image maps.

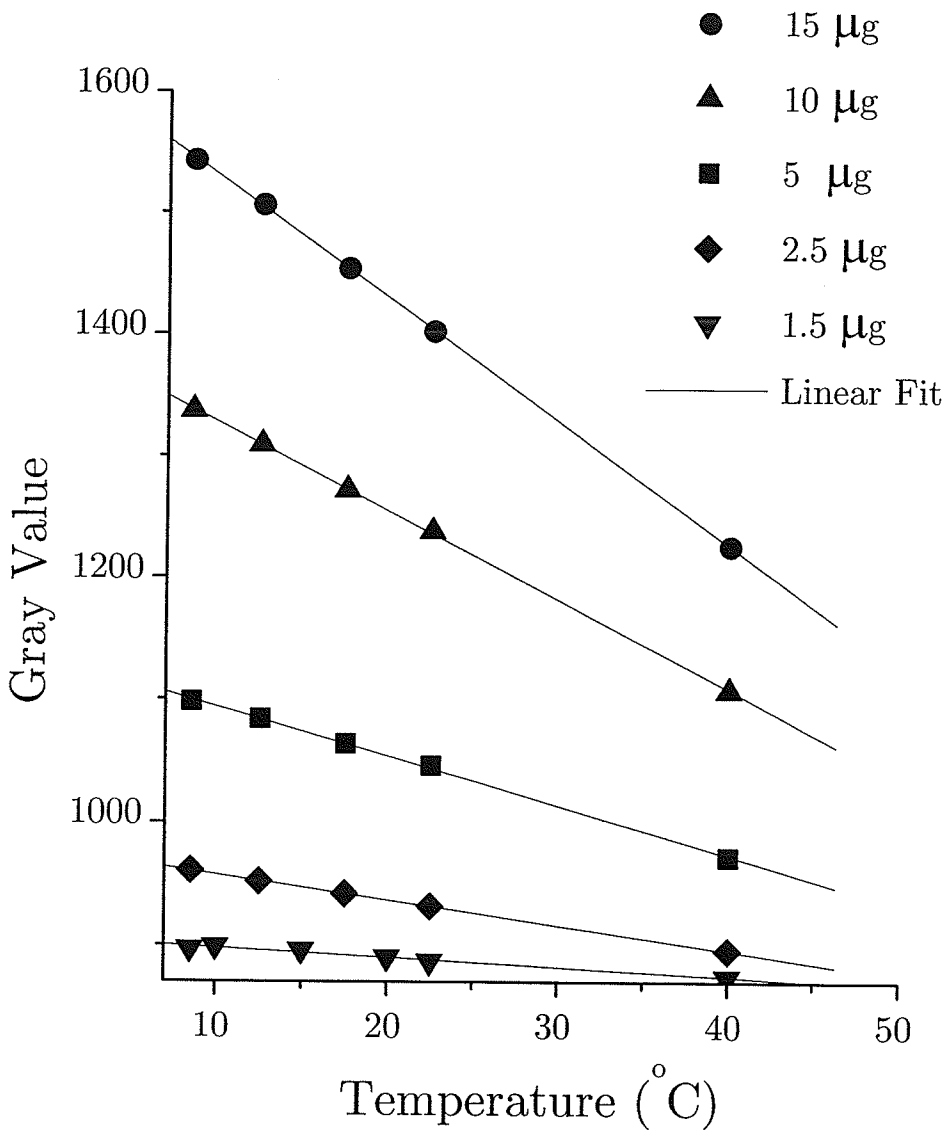

Figure 5.4: Preliminary Calibration: Gray values in PLIF Measurements

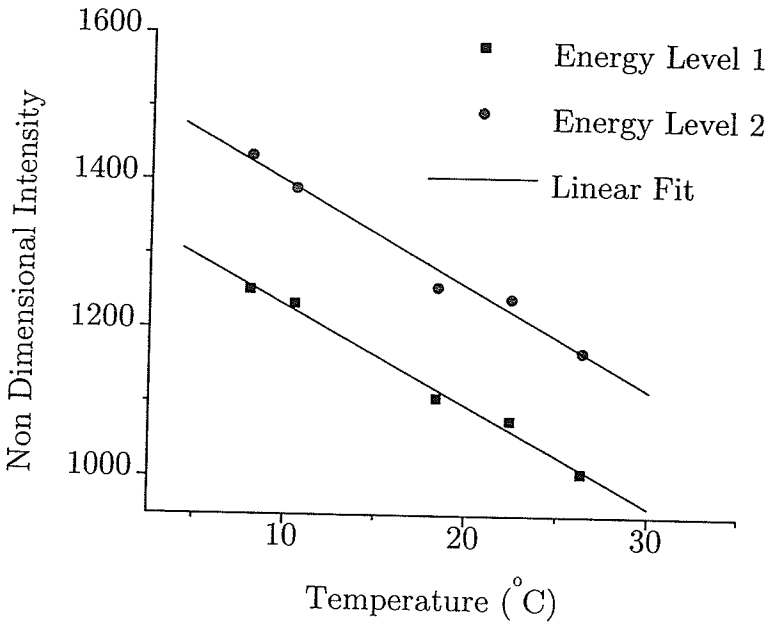

Figure 5.5: Final Calibration

The camera operated at 30Hz, while permitting measurements of about 20 frames per second. The temperatures were recorded after steady-state conditions were reached in both velocity and temperature fields. Temporal uncertainties were considered to have unnoticeable effects on the measurements. The Rayleigh number was controlled by adjusting fluid temperatures into the aluminum heat exchanger side walls. A single CCD camera was used to capture both PLIF and PIV images. The optical filters for each measurement were switched to permit sequential measurements. The PIV images were post-processed by a fast Fourier transform based cross-correlation scheme (FlowManager, Dantec Dynamics). The 1280 $\times$ 1024 pixel PIV image plane of the camera was divided into 32 $\times$ 32 pixel subregions with 50 % overlap, in order to give a spatial resolution of 0.7 mm, based on the whole cavity. The PIV processor was operated in a single frame mode with 100 ms delay time between successive frames to

yield optimal raw velocity data. The PLIF images were re-sampled by a calibration map with a spatial resolution corresponding to the velocity map. The measured velocity vectors are displayed by the PIV software over a discrete grid. Based on the velocity measurements and the PLIF temperature measurements, the conversion algorithm (described previously in Chapter 3) for functional entropy production was applied.

The PLIF measurements were performed to determine temperatures in the denominator of the entropy production in Eq. (3.7). For this buoyancy driven problem, the temperature field varies spatially, thereby affecting the frictional entropy production in Eq. (3.7). The non-intrusive technique of pulsed laser PIV was used for whole-field measurements of velocity, which were post-processed by spatial differencing in the frictional entropy generation. Thus, a similar whole-field non-intrusive technique (Planar Laser Induced Fluorescence) was used for the temperature measurements, rather than thermocouple or other intrusive probes. Constructing a grid with probe locations that match all (i, j) coordinates corresponding to the discrete PIV grid in Eq. (1) would be infeasible and it would lack flexibility over a useful range of applications

5.3 Results and Discussion

Accuracy of the numerical formulation for predicting entropy production has been tested previously with problems involving both heat transfer and fluid flow [32, 37, 84]. In this section, the algorithm is applied to a natural convection problem and compared with benchmark data [76] and measured data. Water was used as the working fluid in the experiments, while air was used in the numerical simulations for benchmarking purposes. The CVFEM formulation was validated against velocity and temperature

data of de Vahl Davies [76] and the entropy production results obtained for the natural convection of air are compared with previous studies.

(i) Case 1: Air (Pr = 0.71)

Figure 5.6 shows predicted velocity and isotherm patterns for Rayleigh numbers of 10^3, 10^4, 10^5 and 10^6. The velocity vectors are shown on a 40×40 grid for easy visualization. The flow structure shows close agreement with contour maps obtained in previous studies [76, 77]. At low Rayleigh numbers in Fig. 5.6, the flow is nearly symmetrical about the center point. As the Rayleigh number increases, the recirculation becomes more elliptical and eventually separates into two zones at $Ra = 10^5$. The boundary layer becomes thinner, with the recirculation zones moving closer to the wall at $Ra = 10^6$. The temperature profile is nearly linear at the lowest Rayleigh number (10^3). As the Rayleigh number increases, convection becomes increasingly significant and the profiles show a progressive departure from linearity. The contours flatten as Ra increases, with the highest temperature gradients closer to the wall. This characteristic arises due to increasing vertical buoyancy-induced motion of the fluid.

Predictions of the average Nusselt number, maximum horizontal velocity on the vertical mid-plane, U_{max}, and the maximum vertical velocity in the horizontal mid-plane of the cavity, V_{max}, and their locations are given in Table 5.3 for Rayleigh numbers of 10^3, 10^4, 10^5 and 10^6 with the 80×80 grid. The x and y coordinates are normalized with respect to the cavity width, L. Also, the velocities are normalized by a diffusion velocity, i.e., $k/(c_p L)$.

As illustrated in Fig 5.7, convergence towards the same grid independent value with the present numerical formulation and the finite difference formulation of de

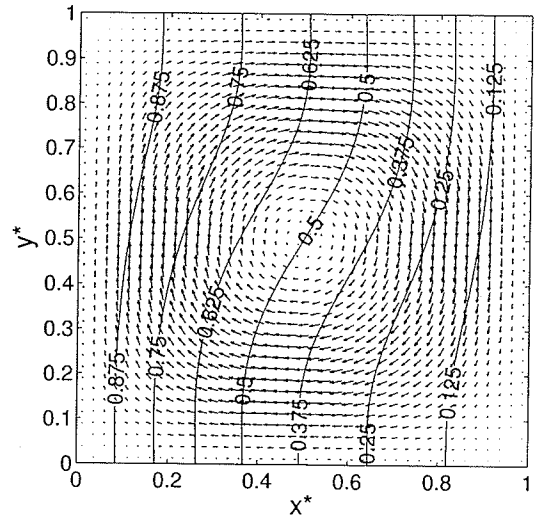

(a) $Ra = 10^3$

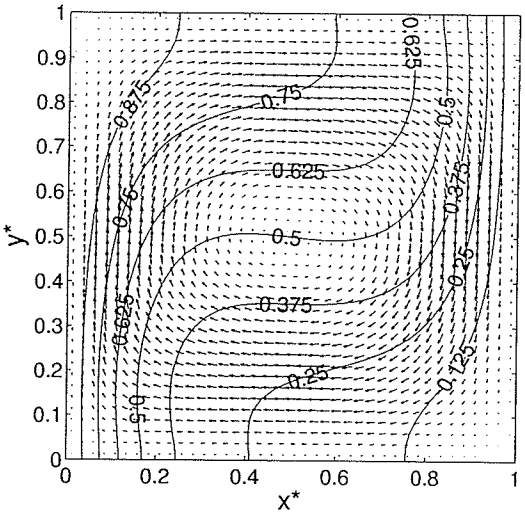

(b) $Ra = 10^4$

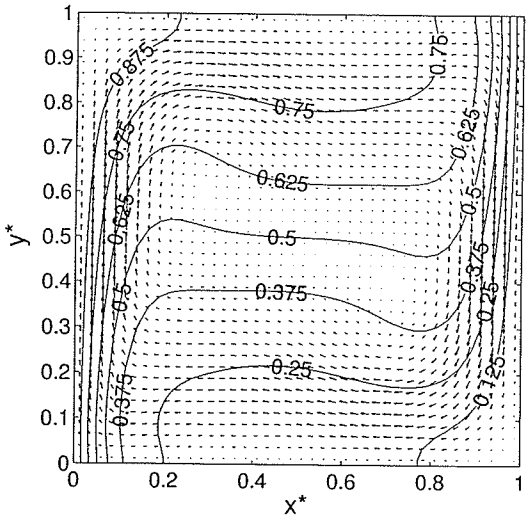

(c) $Ra = 10^5$

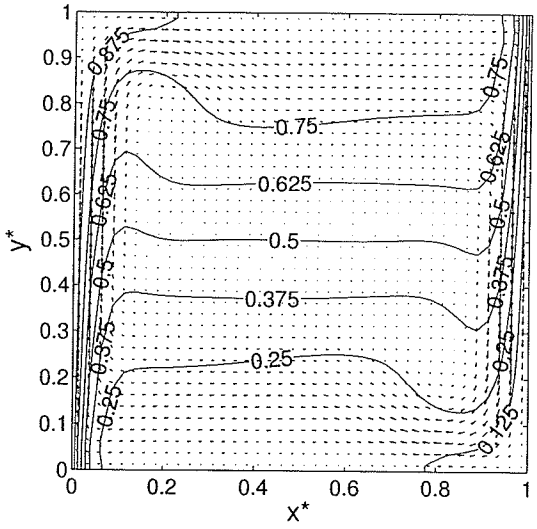

(d) $Ra = 10^6$

Figure 5.6: Predicted Temperatures and Velocities at Varying Rayleigh Numbers

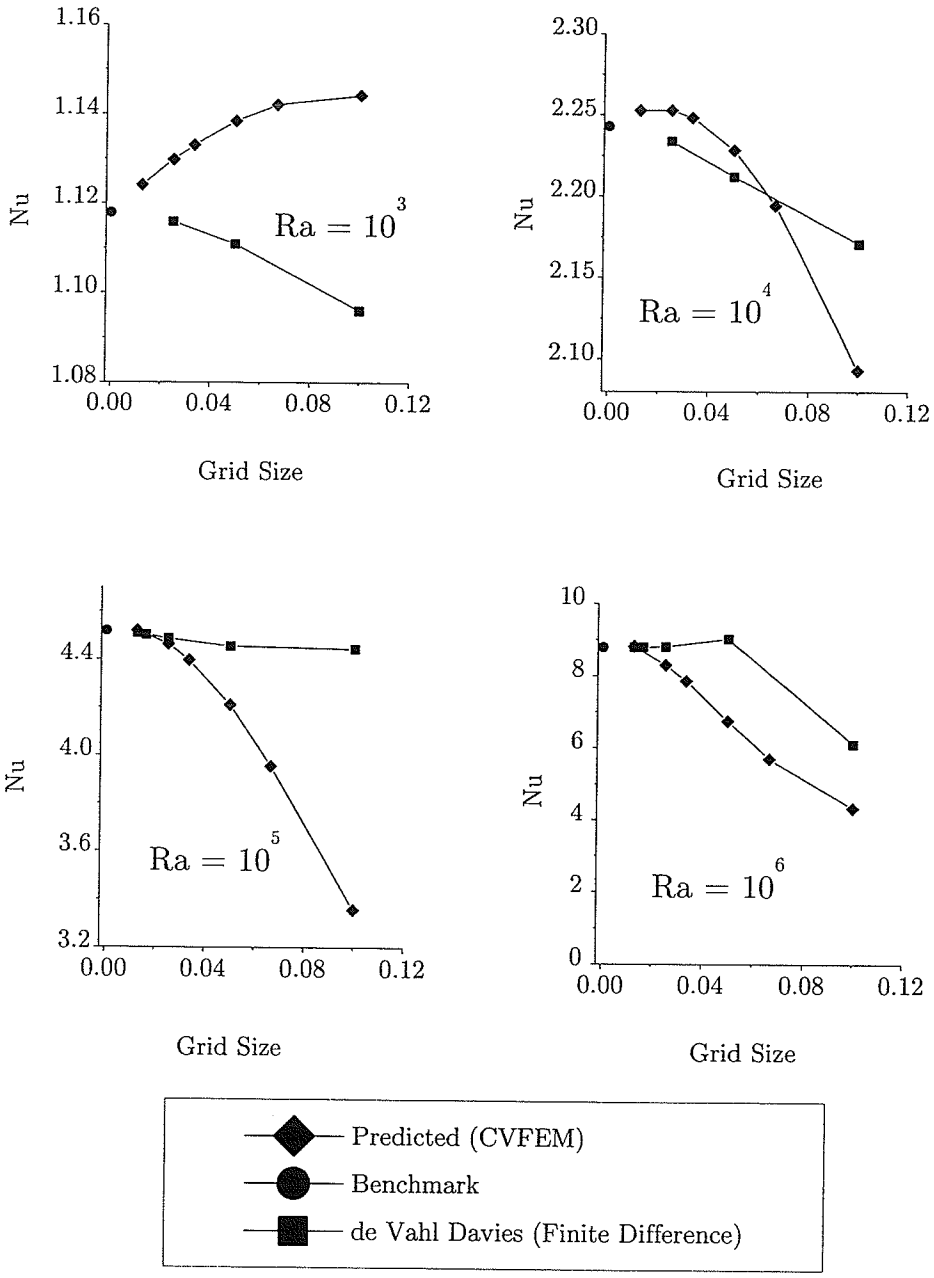

Figure 5.7: Predicted Average Nusselt Numbers at Varying Grid Sizes and Rayleigh Numbers

Table 5.1: Comparison with Benchmark Solution of de Vahl Davis

	U_{max}	y-position	V_{max}	x-position	Nu
	$Ra = 10^3$				
Predicted	3.63068	0.8125	3.69075	0.175	1.12411
Benchmark	3.649	0.813	3.697	0.178	1.118
	$Ra = 10^4$				
Predicted	16.2295	0.825	19.616	0.125	2.2527
Benchmark	16.178	0.823	19.617	0.119	2.243
	$Ra = 10^5$				
Predicted	35.1589	0.85	68.6567	0.0625	4.52037
Benchmark	34.73	0.855	68.59	0.066	4.519
	$Ra = 10^6$				
Predicted	64.805	0.85	220.016	0.0375	8.8312
Benchmark	64.63	0.85	219.36	0.0379	8.8

Vahl Davies [76] can be observed when the mesh is refined. The grid size has been normalized by the width of the cavity. The Nusselt number represents the ratio of the heat flux across the cavity to the heat flux that would result from pure conduction. Since the formulation is conservative, the heat flux across the cavity was determined as the average heat flux at the hot and cold walls of the cavity. The calculation of Nu is performed by finding temperature gradients at the sub-control volume level for all boundary elements. In order to ascertain the accuracy of the numerical formulation, velocity components and temperatures are monitored at a reference location ($x = 0.2$, $y = 0.4$) and recorded for different grid sizes at Rayleigh numbers of 10^3, 10^4 and 10^5. The velocities and temperatures converge towards the grid independent values as the mesh is refined. A Richardson extrapolation for second order schemes was used, i.e.,

$$\phi = \phi_i + \tfrac{1}{3}\left(\phi_i - \phi_{i-1}\right) \tag{5.4}$$

Based on this extrapolation, the grid independent value and the percentage error associated with each grid size were determined. When these errors are plotted against

the grid spacing on a logarithmic scale in Figure 5.8, all curves indicate a slope of 2, thereby suggesting second order accuracy of the numerical formulation. The flow field behavior as Ra increases shows close agreement with the benchmark solution of de Vahl Davis [76]. The results presented for comparison purposes in the remaining figures were obtained with the finest grid.

The predicted entropy generation due to friction irreversibilities at Rayleigh numbers of 10^3 and 10^6 (laminar regime; $Pr = 0.71$) is shown in Figs. 5.9 (a) and (b), respectively. The predicted results show close agreement with previous studies of Baytas [80]. At the low Rayleigh number ($Ra = 10^3$), the entire flow field contributes to entropy production. But at $Ra = 10^6$, these irreversibilities occur predominantly near the side walls. Also, the maximum values occur near the center points along the side walls. At these locations, the near-wall velocities and their spatial gradients are highest, while adverse pressure gradients contribute to flow deceleration when the fluid approaches the corners of the cavity. At the low Rayleigh number (10^3), comparable entropy production rates are observed along both horizontal and vertical walls, since comparable fluid accelerations are observed at those locations. But higher buoyancy along the side walls leads to greater differences of fluid acceleration and entropy production at the higher Rayleigh number (10^6). Entropy production depends on both temperature difference (between wall and fluid) and heat transfer rate. Thus, higher entropy production is often undesirable in free convection problems, since a higher temperature difference (i.e., additional input power to maintain this difference) is needed to maintain a fixed rate of heat transfer between the fluid and wall.

(ii) Case 2: Water (Pr = 8.06)

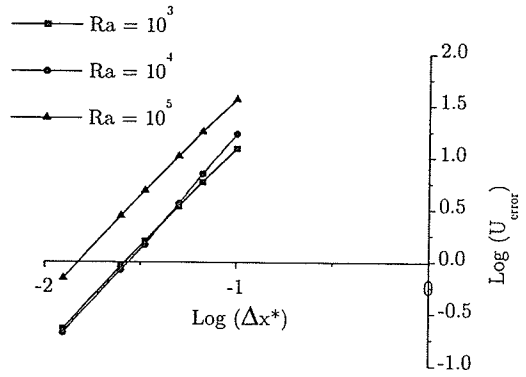

(a) U-velocity

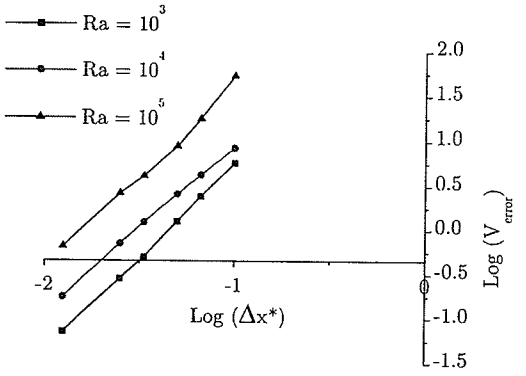

(b) V-Velocity

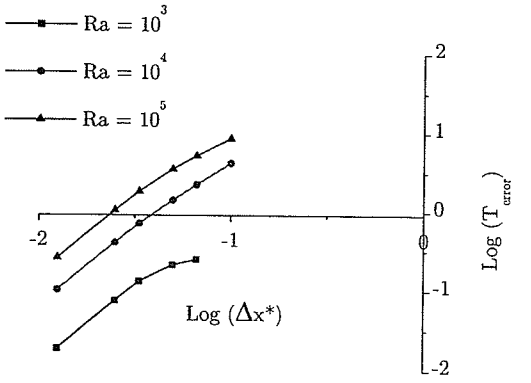

(c) Temperature

Figure 5.8: Error in Predicted Values at Varying Grid Sizes and Rayleigh Numbers

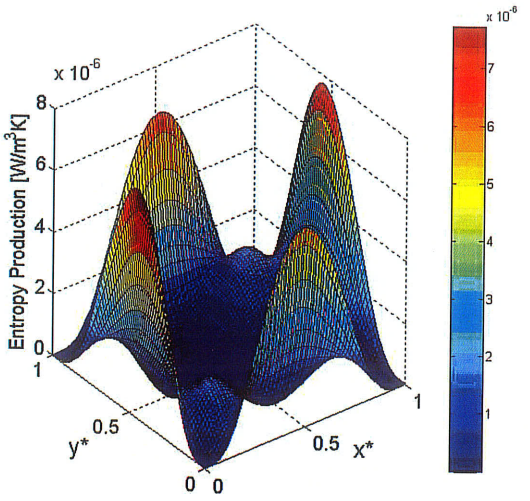

(a)

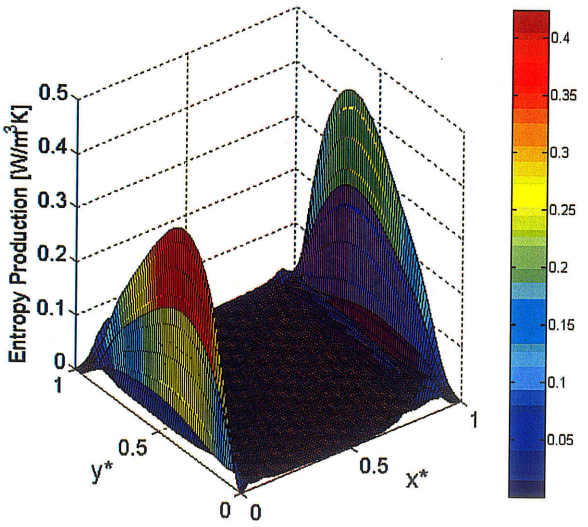

(b)

Figure 5.9: Predicted Entropy Production at Rayleigh Numbers of (a) 10^3 and (b) 10^6

In the remaining figures, a second case of free convection is considered with a working fluid of water ($Pr = 8.06$). The hot and cold walls are maintained at 20 ^{o}C and 10 ^{o}C, respectively, thereby yielding a Rayleigh number of 5.35×10^{6}. As shown in Fig. 5.10, the measured velocities indicate that a single clockwise re-circulation cell developed with highest velocities near the side walls. The fluid velocities diminish rapidly at locations further from the wall, so that velocities become too small for PIV vectors to be displayed in the central region of the cavity. In Figs. 5.11 - 5.12, the U-velocity and V-velocity along the vertical and horizontal mid-planes, respectively, are illustrated. In each case, the velocities are non-dimensionalized with respect to the maximum velocity, while the spatial coordinate is non-dimensionalized with respect to the cavity width.

Close agreement between predicted and measured results is achieved in Figs. 5.11 - 5.12. The measured velocity field is slightly skewed to the right side of the cavity, so some discrepancy between predicted and measured results is observed near the right wall. The numerical simulation assumes a perfectly insulated boundary on both horizontal walls of the cavity, which leads to complete symmetry without skewing of the velocity field. The experimental apparatus closely approaches this idealization, but any slight heat gains through the horizontal boundaries could potentially lead to asymmetry of the buoyancy-driven flow. Experimental uncertainties are considered to have contributed to the slight skewing of the measured velocity to the right in Fig. 5.11. In Fig. 5.12, very close agreement between measured and predicted results is obtained. Velocity measurements were obtained within 1 mm from the wall. However, due to their importance in subsequent spatial differencing for entropy production at the wall, additional measurements, obtained by resolving the velocity field closer to the wall, are presented below. Both Figs. 5.11 and 5.12 exhibit nearly symmetrical profiles of velocity along the mid-planes of the cavity.

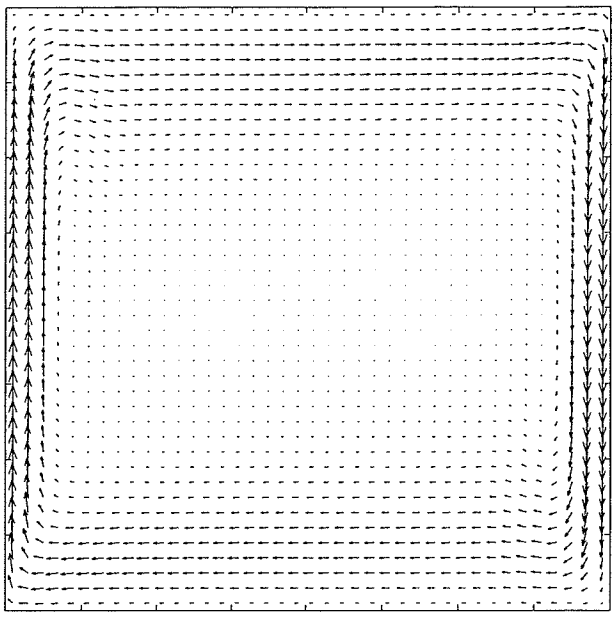

(a) Predicted

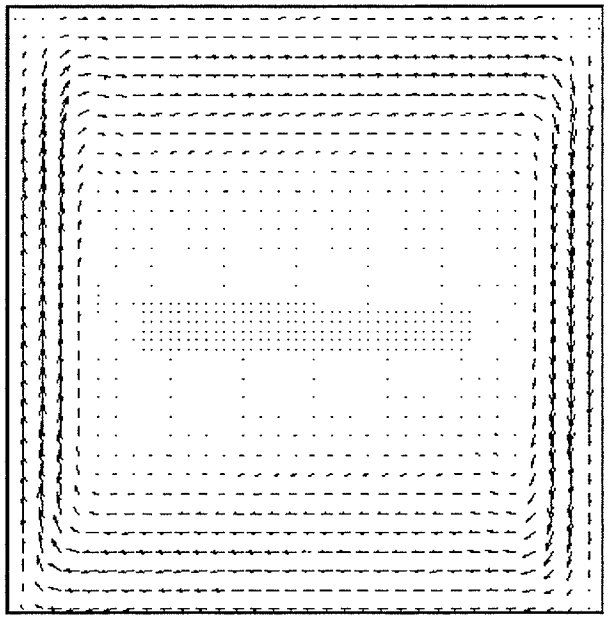

(b) Measured

Figure 5.10: Comparison between Predicted and Measured Velocity Field

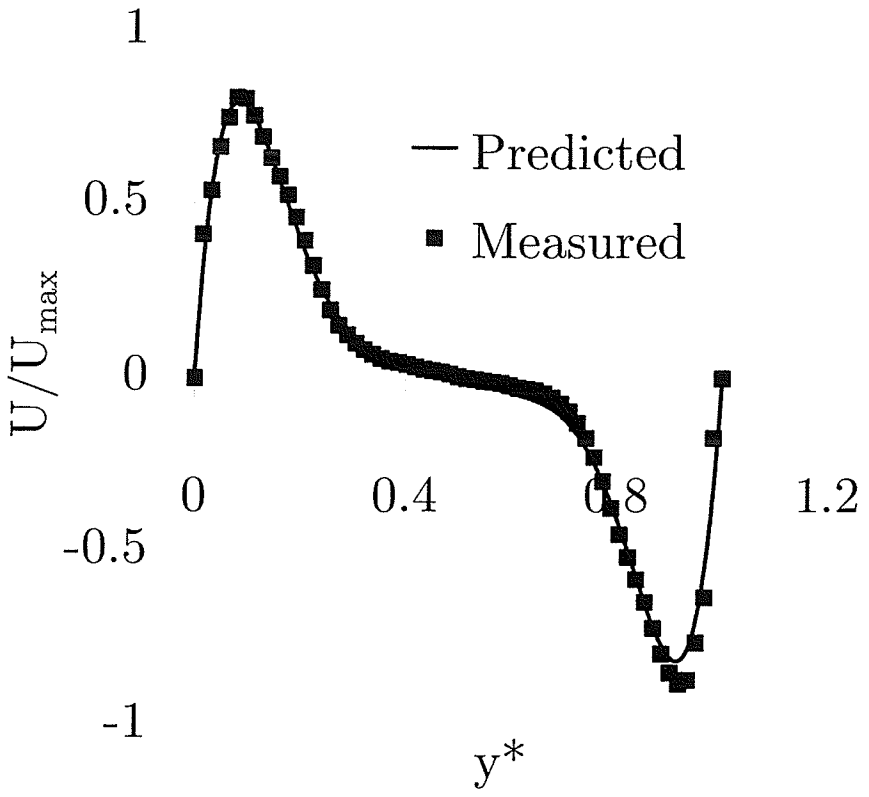

Figure 5.11: U-Velocity on the vertical mid-plane ($Ra = 5.35 \times 10^6$, $Pr = 8.06$)

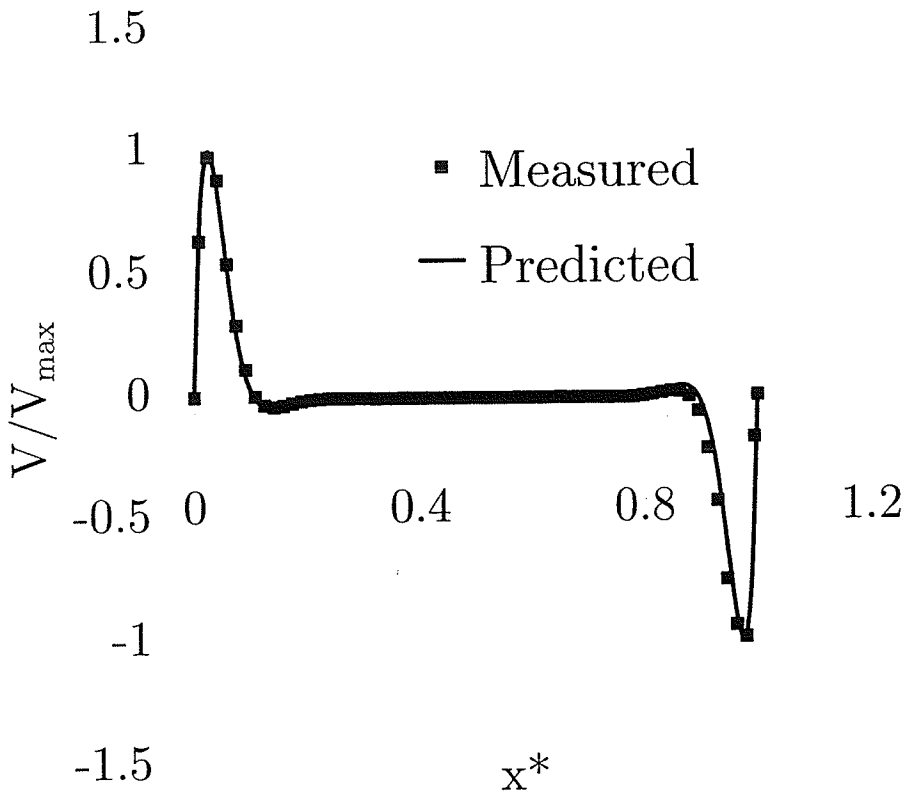

Figure 5.12: V-Velocity on the horizontal mid-plane ($Ra = 5.35 \times 10^6$, $Pr = 8.06$)

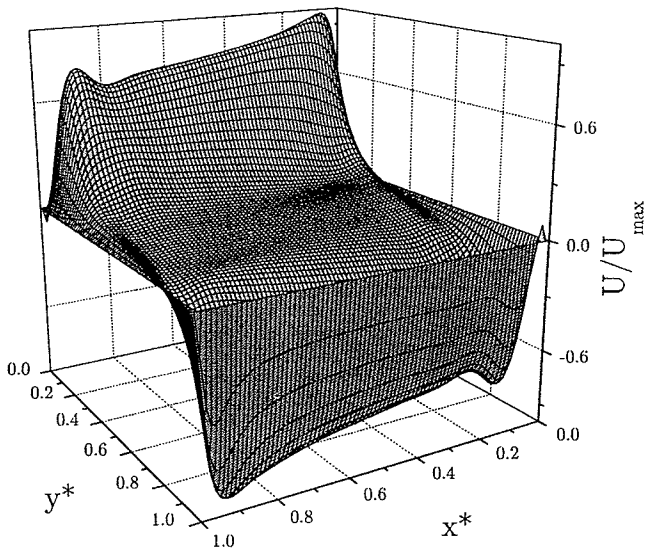

(a)

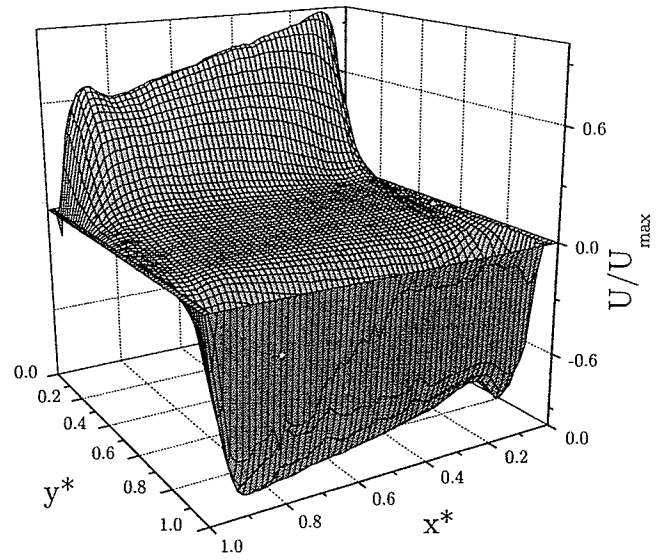

(b)

Figure 5.13: Surface Plot of U-Velocity ($Ra = 5.35 \times 10^6$, $Pr = 8.06$): (a)Predicted (b) Measured

Surface plots of U-velocity values across the entire cavity are shown in Fig. 5.13. These results also show close agreement between predicted and measured results. The maximum horizontal velocity occurs near the top corner of the cold wall. Unlike fluid flow of air at $Pr = 0.71$, where the maximum U-velocity is closer to the hot wall in the top corner of the cavity, the predicted and measured results in Fig. 5.13 ($Pr = 8.06$; water) exhibit a maximum magnitude closer to the top corner of the cold wall. Buoyancy induced acceleration of fluid up the hot wall leads to an adverse pressure gradient and velocity change, when the fluid is re-directed horizontally near that corner. This momentum exchange involves a balance between fluid inertia and forces imparted by pressure, friction and fluid buoyancy. The frictional resistance of the fluid along the wall increases, when the momentum diffusion rate exceeds the energy diffusion rate ($Pr > 1$). This affects the overall momentum balance on the fluid, thereby altering pressure gradients near the top corners of the cavity and changing the trends of maximum fluid velocity for air ($Pr < 1$) and water ($Pr > 1$). Also, the distance of this maximum velocity point from the wall changes at different Prandtl numbers. Past similarity solutions of free convection along a vertical wall have confirmed that the point of maximum velocity moves closer to the wall at higher Prandtl numbers (see Ref. [1]).

In Fig. 5.14 at higher Rayleigh numbers, the temperature field is skewed about the center of the cavity with hot fluid drifting closer to the cold wall. The temperature field is flattened with the hottest fluid at the top left region of the cavity. This temperature distribution suggests an increasing magnitude of buoyancy effects along the vertical cold surface of the enclosure. Stronger convection closer to this wall leads to higher velocities. This observation is consistent with results obtained previously by Hamady and Lloyd [85]. Comparisons show similar temperature stratification in both numerical and experimental data.

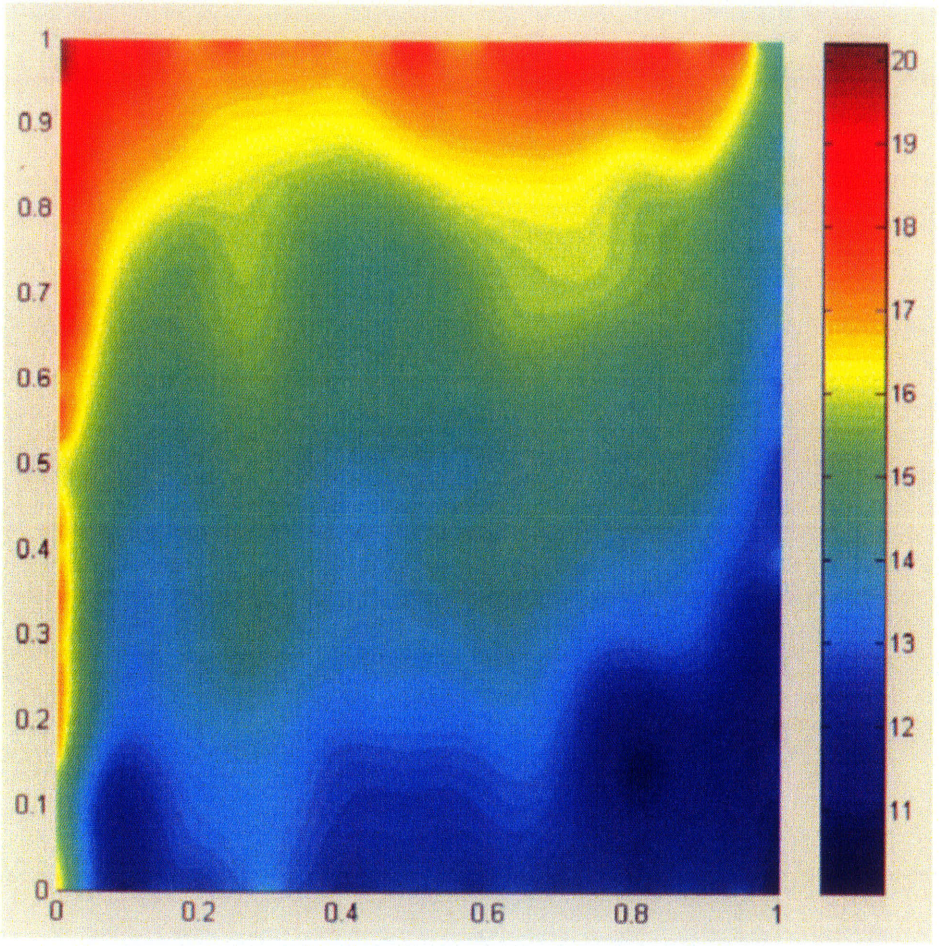

Figure 5.14: Measured Temperatures

Post-processing of the measured velocity results yields the spatial variation of entropy production throughout the cavity. Figure 5.15 shows the predicted and measured entropy production along the horizontal mid-plane. The peak values occur at the vertical walls, corresponding to the locations of largest spatial gradients of velocity. Away from these points, entropy production decreases sharply to approximately zero close to the wall, which corresponds to the local maximum and zero gradient of V-velocity near the wall in Fig. 5.12. Beyond this local maximum of velocity, entropy production increases to a local maximum and decreases back to nearly zero in the central region of the enclosure. The result presented in Fig. 5.15 has been normalized with a reference entropy production, $P_s(ref)$ at this local maximum. The entropy production reaches a minimum value in the center of the cavity, where the stagnation point of the re-circulation cell is observed. Close agreement between qualitative trends of predicted results and measured entropy production is observed in Fig. 5.15. But greater oscillations of measured entropy production are observed closer to the wall, when the whole cavity is captured, due to limitations of camera resolution. Due to the importance of these near-wall irreversibilities, additional velocity and entropy production measurements, obtained by resolving the velocity field closer to the wall, are shown in Fig. 5.16.

Figures 5.16 - 5.19 show near-wall measurements of v-velocity and entropy production in the mid-region of the cavity at the cold wall. In Fig. 5.16, the measured maximum U and V components of velocity are 0.611 mm/s and 1.69 mm/s, respectively. The predicted maximum U and V components of velocity are 0.632 mm/s and 1.89 mm/s, respectively. Although efforts were taken to minimize heat losses from the top, bottom, front and back walls, any losses may have affected thermal buoyancy, thereby yielding lower measured velocities, as compared with the numerical predictions. Close agreement between predicted and measured velocities near the wall are

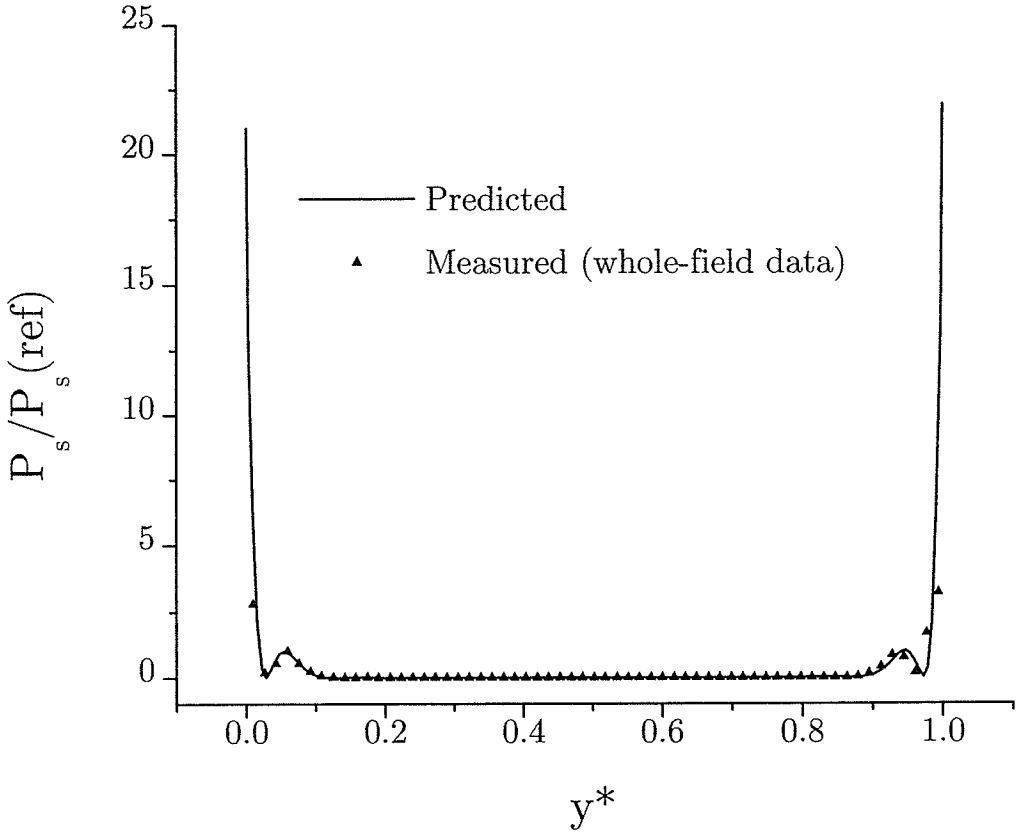

Figure 5.15: Entropy Production on the horizontal mid-plane ($Ra = 5.35 \times 10^6$, $Pr = 8.06$)

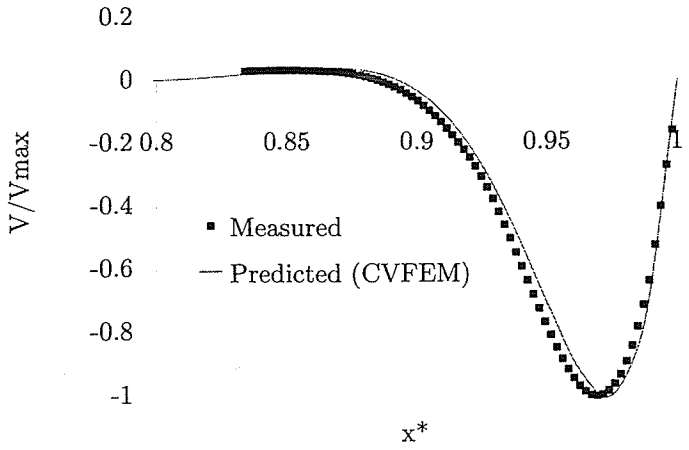

(a)

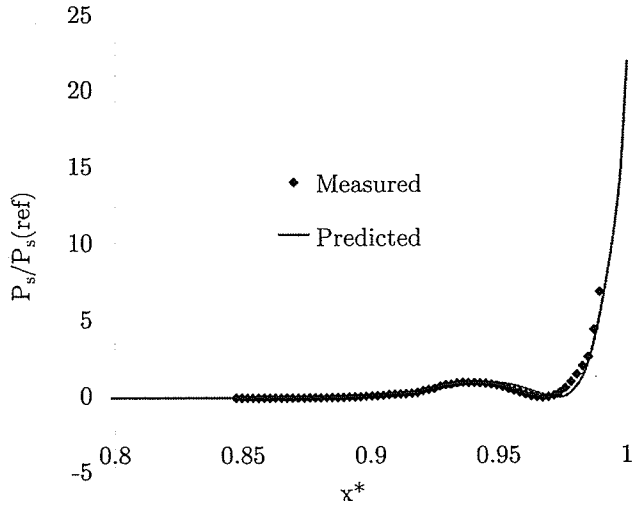

(b)

Figure 5.16: Near- Wall Measurements on Horizontal Mid-plane ($Ra = 5.35 \times 10^6$, $Pr = 8.06$): (a) V-velocity (b) Entropy Production

important, since near-wall spatial gradients of velocity are needed for the entropy production calculations. Although PIV technology is limited by camera resolution and particle tracing of small-scale structures near the wall, the experiments successfully measured velocity and derived entropy production at very close proximity to the wall (see Figures 5.16 (a) and (b)). In particular, a resolution of 0.2mm was achieved in the wall region between $0.65 \leq x* \leq 1$ and $0.35 \leq y* \leq 0.7$. Such near-wall accuracy becomes particularly significant for turbulent flows.

Measured oscillations of entropy production can be effectively reduced through filtering of velocity data. In Fig. 5.17, a 3×3 average filter was used for smoothing of the raw velocity vectors, before calculating entropy production. Previous PIV studies [86] have shown that filtering does not introduce additional error into the measured velocity, but it serves to mitigate uncertainty by averaging velocities at surrounding grid points. Figure 5.17 shows the measured velocity distribution with the corresponding filtered profile at the horizontal mid-plane. The results illustrate the benefit of filtering, particularly for the near-wall raw data points and removing random uncertainty in the measured velocity gradients.

Figures 5.18 and 5.19 illustrate the quality of the experimental data in a representative sub-region of the cavity. These figures confirm the capability of local mapping of entropy production, and consequently, exergy losses in fluid systems for design optimization purposes. This measurement procedure is considered to be a useful diagnostic tool for identifying local flow losses, so that energy conversion devices can be re-designed locally around regions of highest entropy production. It is viewed that the current developments provide a useful basis, from which future advances can extend the method to more complex flows, such as turbomachinery, heat exchangers or microelectronics cooling problems.

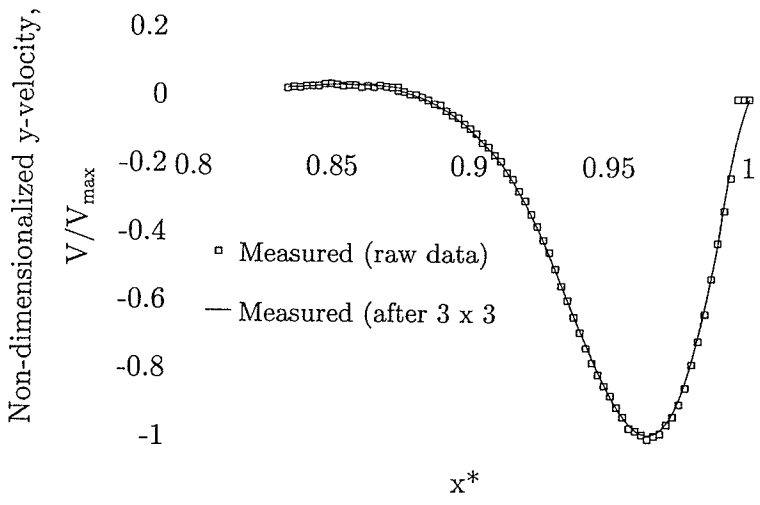

Figure 5.17: Filtering of Velocity Profile ($Ra = 5.35 \times 10^6$, $Pr = 8.06$)

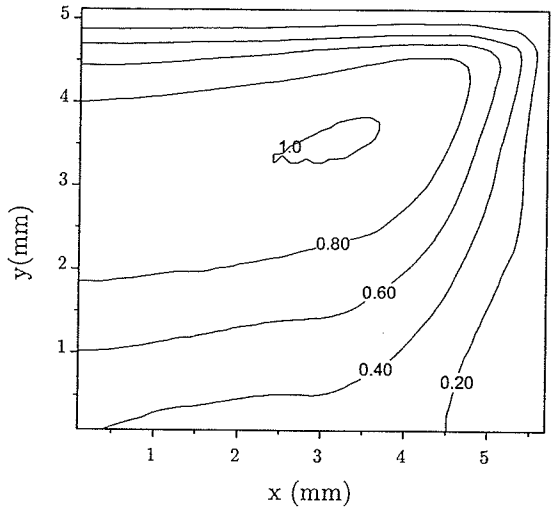

(a)

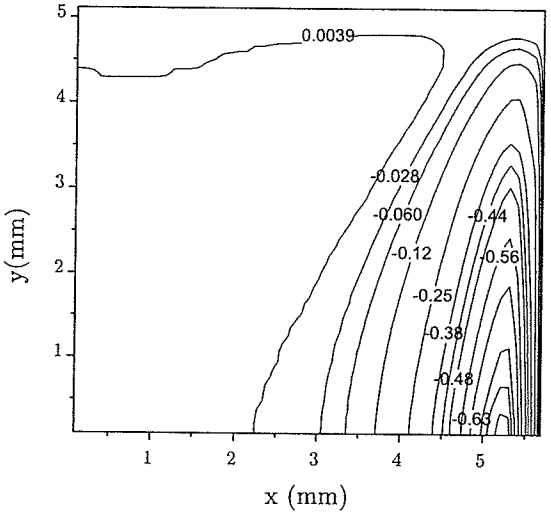

(b)

Figure 5.18: Measurements in the top right corner ($Ra = 5.35 \times 10^6$, $Pr = 8.06$): (a) U-velocity (b) V- Velocity

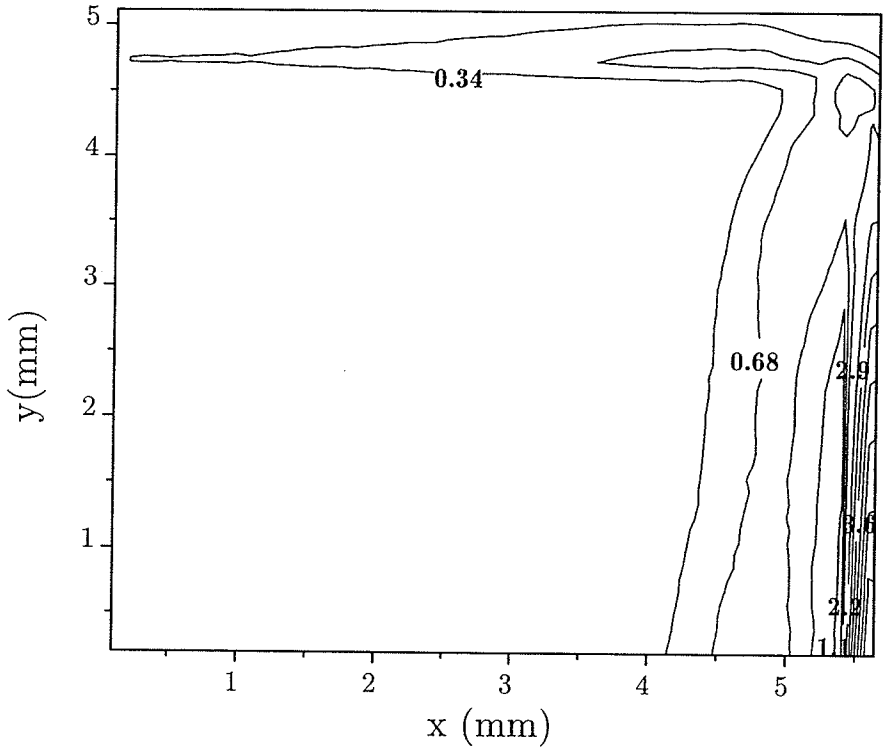

Figure 5.19: Measurements in the top right corner ($Ra = 5.35 \times 10^6$, $Pr = 8.06$) for Non-dimensional Entropy Production

Chapter 6

Uncertainty Analysis

6.1 Bias and Precision Errors

Uncertainty analysis involves systematic procedures for calculating error estimates for experimental data. When estimating errors in heat transfer experiments, it is usually assumed that data is gathered under fixed (known) conditions and detailed knowledge of all system components is available. Measurement errors arise from various sources, but they can be broadly classified as bias errors and precision (or random) errors. Bias errors remain constant during a set of measurements. They are often estimated from calibration procedures or past experience. Alternatively, different methods of estimating the same variable can be used, so that comparisons between those results would indicate the bias error.

Elemental bias errors arise from calibration procedures or curve-fitting of calibrated data. Also, "fossilized" bias errors arise when measuring and tabulating thermophysical properties. Although such errors are usually less than 1 %, Coleman and Steele [87] describe cases involving much higher levels of fossilized bias errors. Moffat [88] outlines a "conceptual bias", which includes a residual uncertainty due to variability arising in the true definition of the measured variable. For example, if point measurements are used to approximate bulk temperatures at the inlet and

exit of a duct, then the difference between these temperatures and the bulk mean temperature contributes to a conceptual bias error, since point measurements cannot fully capture the spatially averaged bulk value.

In contrast to bias errors, precision errors appear through scattering of measured data. Such errors are affected by the measurement system (i.e., repeatability, resolution) or spatial / temporal variations of the measured quantity. Also, the procedure itself may lead to precision errors arising from variations in operating conditions. If an error can be estimated statistically, then it is usually considered to be a precision error. Otherwise, it is generally assumed to be a bias error. Anticipated precision errors are often used to guide experimental designs and procedures, in view of collecting data within a desired range of measurement uncertainty. Gui et al. [89] outline precision errors and other PIV measurement uncertainties in a towing tank experiment. Precision errors are reduced by increasing the number of measurement samples.

Alekseeva and Navon [90] found temperature uncertainties based on first and second order adjoint equations. An adjoint formulation of an inverse heat transfer problem leads to uncertainty indicators for the corresponding direct problem. Hessian maximum eigenvalues from the second order adjoint equations can be used to evaluate the uncertainty indicators [90]. Pelletier et al. [91] show how sensitivity equations provide useful information regarding which parameters affect the flow response. Uncertainties are estimated with flow sensitivities, which are used to propagate parameter uncertainties throughout the domain. Applications to turbulent flow in an annular duct and conjugate free convection were considered [91].

Measurement uncertainties of flow parameters depending on input data errors (such as initial and boundary conditions) can be effectively calculated with adjoint equations. Alekseeva and Navon [92] use adjoint temperatures to calculate the transfer of uncertainties from such input data. Spatial propagation of errors affects the

overall experimental uncertainties. An individual error within an experiment combines with other errors, thereby leading to added uncertainty. Contributions can be evaluated separately with sensitivity coefficients involving the measured quantities and post-processed results, based on propagation equations [93]. Propagated uncertainties are often classified according to zero-order or higher-order uncertainties. In the former case, all parameters affecting the measurements are assumed to be fixed, except for the procedure of the experiment. Thus, data scattering arises from instrumentation resolution alone. In the latter case (higher-order uncertainty), control of the experimental operating conditions is considered, so factors such as time are included. The degree of variability of operating conditions can be expressed by the standard deviation. The standard error of the mean describes how much variation of operating conditions is expected, when repeated samples from the same experiment are taken. It is the standard deviation of the mean, divided by a number characterizing the size of the sample. If this value is small, then there is large confidence in the measurement. But if the standard error of the mean is large, then either significant variations arise in the measurements, or the sample size was too small.

6.2 Uncertainty of Measured Entropy Production

Measurement uncertainties of primary variables (such as fluid velocity) with various experimental techniques have been widely reported previously, i.e., Lassahn [94], Moffat [95], Kline [96] and others. Post-processing of measured data, such as measured vorticity from post-processed PIV data [86], entails additional uncertainties in the conversion algorithm. Unlike the primary variables with their governing conservation equations (equalities), entropy cannot be measured directly and it is governed by an inequality (Second Law of Thermodynamics). The purpose of this section is to

determine how accurately entropy production can be measured with whole-field laser techniques involving PIV and PLIF. In particular, conventional error indicators [97] are extended to the scalar variable of entropy production. Bias errors are related to sensitivity coefficients of the measured entropy production.

The friction irreversibility of entropy production can be expressed by the viscous dissipation divided by temperature. In the previous chapters, the local entropy production rate, $\dot{P}_s$, was determined from

$$\dot{P}_s = \frac{\mu}{T(i,j)}\left(\frac{u(i,j+1)-u(i,j-1)}{\Delta y}+\frac{v(i+1,j)-v(i-1,j)}{\Delta x}\right)^2 + 2\frac{\mu}{T(i,j)}\left[\left(\frac{u(i+1,j)-u(i-1,j)}{\Delta x}\right)^2+\left(\frac{v(i,j+1)-v(i,j-1)}{\Delta y}\right)^2\right] \quad (6.1)$$

where Δx and Δy refer to twice the grid spacing in the x and y directions, respectively.

This procedure was presented previously for whole-field measurements of velocity. In the following sections, an uncertainty assessment of entropy production will be presented for laminar channel flow and the free convective heat transfer problems.

6.3 Case 1: Laminar Channel Flow

Since measured entropy production is a post-processed variable, the first step is assessing the experimental uncertainties of measured velocities. Pulsed laser illumination and PIV incur certain errors from statistical correlations of the interrogation areas, when determining the fluid velocities. For the problem of laminar channel flow (see Fig. 4.1), the average fluid velocity for an interrogation area at any instant is reduced by the following equation,

$$U = \frac{\Delta s L_o}{\Delta t L_I} \quad (6.2)$$

where t is the time interval between laser pulses, Δs is the particle displacement from the correlation algorithm, L_o is the width of the camera view in the object plane and L_I is the width of the digital image. The total error, ϵ, in a measured quantity is a sum of the bias component, B, and a precision component, P. The bias error of the measured velocity is related to the elementary bias errors based on the sensitivity coefficients, i.e.,

$$B_u^2 = \eta_{\Delta s}^2 B_{\Delta s}^2 + \eta_{\Delta t}^2 B_{\Delta t}^2 + \eta_{L_o}^2 B_{L_o}^2 + \eta_{L_I}^2 B_{L_I}^2 \tag{6.3}$$

where the sensitivity coefficients are defined as

$$\eta_\chi = \partial u / \partial \chi \tag{6.4}$$

The manufacturer's specifications of the elementary bias limits (t, Δs) are shown in Table 6.1. The width of the camera view in the object plane, L_o, depends on distances and configurations related to the experimental setup, so the bias limit for L_o is determined from calibration procedures, not manufacturer's specifications. In this calibration, the physical dimensions and spatial resolution of the camera view in the measurement plane are determined. Then the width of the digital image is determined by the number of pixels corresponding to these dimensions. In this problem, the width of the camera view in the object plane and bias limit for L_o are 0.0126 m and 0.0001, respectively. The uncertainty associated with this bias limit can be reduced with a more refined procedure for measurement of L_o. As mentioned in Chapter 3, the PIV image pairs are cross-correlated with a 32 $\times$ 32 interrogation window and 50% overlap. This yielded a Δs value of 6.4 pixels in the centerline. The measurement plane is 12.9 mm $\times$ 15.9 mm. Therefore, L_I and L_o are 1024 pixels and 12.9 mm, respectively. By combining the contributions of each bias error and the sensitivity coefficient, a velocity error of 0.76% is obtained for the full scale. The major source of velocity uncertainty occurs from locating the image displacement

Table 6.1: Bias Errors (case 1)

Variable, χ	Magnitude	B_χ	η_χ	$B_\chi\eta_\chi$	$\frac{B_\chi\eta_\chi}{\Sigma B_\chi\eta_\chi}$	$(B_\chi\eta_\chi)^2$
$L_o(m)$	1.26E-02	0.0001	4.13	4.13e-04	58.8	1.71E-07
$L_I(pixel)$	1024	0.5	-5.09E-05	2.54E-05	3.6	6.47E-10
$\Delta t(s)$	1.50E-03	1.0E-07	-3.47E+01	3.47E-06	0.5	1.21E-11
$\Delta s(pixel)$	6.35	0.03175	8.20E-03	2.60E-04	37.1	6.78E-08
				$\sum B_\chi\eta_\chi$ = 7.03E-04		$B_U = 0.0005$
					Bias Error = 0.0645 $\pm$ 0.7586%	

peak, s.

The precision error (P) of an average value, $\bar{\chi}$, measured from N samples is given by

$$P = \frac{t\sigma}{N} \tag{6.5}$$

where t is the confidence coefficient and σ is the standard deviation of the sample of N images. Also, t equals 2 for a 95% confidence level [98]. The standard deviation is defined as follows,

$$\sigma = \sqrt{\frac{1}{N-1}\sum_{k=1}^{N}(\chi_k - \bar{\chi})^2} \tag{6.6}$$

where the average quantity is defined by the following equation,

$$\bar{\chi} = \frac{1}{N}\sum_{k=1}^{N}\chi_k \tag{6.7}$$

Typical values of the standard deviation along the centerline and the near-wall region are 15% and 33%, respectively. These values give precision limits of 0.67% and 1.55% for those regions. Therefore, the total uncertainty of measured velocity in the middle of the channel and the near-wall region become 1.4% and 2.2%, respectively.

Based on these results, the errors of measured entropy production can be estimated. A data reduction equation for entropy production is given by

$$\dot{P}_s = \frac{\mu}{T}\left(\frac{\Delta u}{\Delta y}\right)^2 + \frac{k}{T}\left(\frac{\Delta T}{\Delta y}\right)^2 \tag{6.8}$$

The total uncertainties $(B + P)$ for the U, T and y variables are

$$\begin{aligned} U_i &= \bar{U}_i \pm \varepsilon_{U_i} \\ T_i &= \bar{T}_i \pm \varepsilon_{T_i} \\ y_i &= \bar{y}_i \pm \varepsilon_{y_i} \end{aligned}$$

The uncertainty in ΔU is obtained as follows,

$$\varepsilon_{\Delta u} = \pm\sqrt{(\theta'_{u,i+1}\varepsilon_{u,i+1})^2 + (\theta'_{u,i-1}\varepsilon_{u,i-1})^2} \tag{6.9}$$

where

$$\theta'_{u,i-1} = \frac{\partial(\Delta u)}{\partial u_i} \tag{6.10}$$

Note that $\theta'_{u,i-1} = -1$ and $\theta'_{u,i+1} = 1$ or vice versa. The uncertainty of ΔT is calculated in the same manner as Eqs. (6.9) and (6.10), except that the velocity component, U, is replaced by temperature, T. In the upcoming results, the analytical solution of entropy production is derived from differentiation of the Poiseuille velocity profile for laminar channel flows, thereby leading to the frictional irreversibility in the first term on the right side of Eq. (6.8). This solution neglects temperature variations, since the experiment was conducted between unheated plexiglass plates in an essentially isothermal water tunnel. However, the frictional irreversibility dissipates kinetic energy to internal energy, which produces a small temperature change in the boundary layer near the walls. The uncertainty corresponding to this measured

Table 6.2: Bias and Precision Error of Entropy production at y=1.7mm (case 1)

Variable, χ	Magnitude	ε_χ	η_χ	$\varepsilon_\chi\eta_\chi$	$\frac{\varepsilon_\chi\eta_\chi}{\Sigma\varepsilon_\chi\eta_\chi}$	$(\varepsilon_\chi\eta_\chi)^2$
$U(m/s)$	0.0345	0.00013453	0	0	0.0	0
$y(m)$	0.0126	0.000001	0	0	0.0	0
$T(K)$	295	2	-3.3466E-06	6.7E-06	5.3	4.4799E-11
$\mu(kg/ms)$	0.001003	0	3.1459E-03	0	0.0	0
$k(W/mK)$	0.5996	0	0	0	0.0	0
$\Delta U(m/s)$	0.00336544	0.00019026	5.8670E-01	0.00011	89.0	1.246E-08
$\Delta y(m)$	0.0001975	1.4142E-06	-4.9987E+00	7.1E-06	5.6	4.9975E-11
$\Delta T(K)$	0	2.828427	0	0	0.0	0
				$\sum\varepsilon_\chi\eta_\chi$ = 1.25E-04		ε = 0.000112
					Error = 0.00095268 ± 11.76%	

temperature change is reported in Table 6.2, based on the procedure outlined in Eqs. (6.9) and (6.10).

Similarly,

$$\varepsilon_{\Delta y} = \pm\sqrt{(\theta'_{y,i+1}\varepsilon_{y,i+1})^2 + (\theta'_{y,i-1}\varepsilon_{y,i-1})^2} \tag{6.11}$$

where

$$\theta'_{y,i-1} = \frac{\partial(\Delta y)}{\partial y_i} \tag{6.12}$$

Neglecting the error in reported thermophysical properties,

$$\varepsilon^2_{P_s} = \eta^2_T\varepsilon^2_T + \eta^2_{\Delta u}\varepsilon^2_{\Delta u} + \eta^2_{\Delta y}\varepsilon^2_{\Delta y} + \eta^2_{\Delta T}\varepsilon^2_{\Delta T} \tag{6.13}$$

Based on this equation and the previous procedure of individual uncertainties, it was determined that the experimental uncertainty of entropy production was 11.67%

at a point of 3mm from the bottom wall. But less error was observed when analytical results were compared with measured data (agreement within ± 6.6 % close to the wall). The measurement uncertainties represent a maximum error bound within the 95% confidence interval. Detailed calculations of the experimental uncertainties are summarized in Tables 6.1 - 6.2.

The accuracy of the entropy production algorithm was validated by comparing the measured values of velocity and entropy production to an analytical solution for laminar channel flow. The differences between analytical and measured results are generally less than 1.2 %. A maximum difference of 6.6 % between the measured entropy production and the analytical result occurs close to the wall. The location of this maximum error is not unexpected, in view of PIV limitations due to particle tracking, camera resolution and a reduced number of seeding particles in each interrogation region near the wall.

6.4 Case 2: Free Convective Heat Transfer

A similar procedure for free convection in an enclosure (as section 6.3; near-isothermal channel flow) was adopted for the bias and precision errors, but with certain differences due to variations of temperature within the enclosure (see Fig. 5.1). Unlike the previous channel flow problem, friction irreversibilities in this problem vary spatially due to both velocity and temperature variations across the flow field. For this problem, the bias error of the measured velocity is related to the elementary bias errors and sensitivity coefficients as follows,

$$B_u^2 = \eta_{\Delta s}^2 B_{\Delta s}^2 + \eta_{\Delta t}^2 B_{\Delta t}^2 + \eta_{L_o}^2 B_{L_o}^2 + \eta_{L_I}^2 B_{L_I}^2 \tag{6.14}$$

where the same definition of sensitivity coefficients is used, i.e. $\eta_\chi = \partial U/\partial \chi$. By

combining the contributions from each source of bias and the sensitivity coefficient, a full-scale velocity bias error of 0.45% is obtained. Similarly as previously described, the precision error (P) of an average value, $\bar{\chi}$, measured from N samples and the standard deviation are given by Eqs. (6.5) and (6.6), respectively.

Typical values of the standard deviation at the points of maximum velocity and near the wall are 0.5% and 1.2%, respectively. These values yield precision limits of 0.005% and 0.012%, respectively. Therefore, the total uncertainties of measured velocity at these points are 0.45% and 0.5%, respectively.

For this free convection problem, the data reduction equation for friction irreversibility of entropy production becomes

$$P_s = \frac{\mu}{T}\left\{\left(\frac{\Delta u_y}{\Delta y}\right)^2 + \left(\frac{\Delta v_x}{\Delta x}\right)^2 + \left(\frac{\Delta u_x}{\Delta x}\right)^2 + \left(\frac{\Delta v_x}{\Delta y}\right)^2\right\} \tag{6.15}$$

The same definitions are applied from the previous problem, including the total uncertainties for the U, T, y, ΔU and Δy variables. Then, the total uncertainty of entropy production becomes

$$\varepsilon_{P_s}^2 = \eta_T^2\varepsilon_T^2 + \eta_{\Delta U}^2\varepsilon_{\Delta U}^2 + \eta_{\Delta V}^2\varepsilon_{\Delta V}^2 + \eta_{\Delta y}^2\varepsilon_{\Delta y}^2 \tag{6.16}$$

For this problem of free convection, the total uncertainty of measured entropy production was estimated to be 9.34% at $x = 0.985L$ and $y = 0.46L$, where L refers to the cavity height. This estimate represents a maximum error bound within the 95% confidence interval. Tables 6.3 - 6.4 show the summarized calculations of the experimental uncertainties for this problem of free convection in an enclosure. The uncertainty of temperature measurements is included in the overall uncertainty of entropy production. This total uncertainty is represented in terms of precision and bias components, with sensitivity coefficients involving the PLIF temperature measurements (see Table 6.4).

Table 6.3: Bias Error (case 2)

Variable, χ	Magnitude	B_χ	η_χ	$B_\chi \eta_\chi$	$\frac{B_\chi \eta_\chi}{\Sigma B_\chi \eta_\chi}$	$(B_\chi \eta_\chi)^2$
$L_o(m)$	7.00E-03	0.0001	6.51E-02	6.51E-06	61.8	4.24E-11
$L_I(pixel)$	1024	0.5	-4.45E-07	2.23E-07	2.1	4.95E-14
$\Delta t(s)$	9.00E-02	1.0E-07	-5.06E-03	5.06E-10	0.0	2.56E-19
$\Delta s(pixel)$	6.00	0.05	7.60E-05	3.80E-06	36.1	1.44E-11
			$\sum B_\chi \eta_\chi$ = 1.05E-05		B_U = 7.5404E-06	
				Bias Error = 1.67E-03 ± 0.4515%		

Although the total entropy production includes friction and thermal irreversibilities, this study focuses on the friction irreversibility component. This component includes velocity gradients and measured temperatures in the denominator, while the thermal component involves temperature gradients in the flow field. Since the uncertainties of measured temperatures are small compared to the magnitude of the absolute temperature in the denominator, the sensitivity coefficient of temperature in the uncertainty analysis is small. Based on parameters outlined in Table 6.4, the sensitivity coefficient for temperature is 5.0 $\times 10^{-9}$. The maximum error in the PLIF temperature measurements (ε_T) becomes $\pm 5^o C$. This error is combined with others in the total uncertainty of entropy production, including measured velocity gradients in the flow field. The dynamic viscosity has been evaluated at a uniform temperature (288 K). Variations of the dynamic viscosity, due to changes or errors in the measured temperatures, have been neglected in the uncertainty analysis.

In summary, this section has presented an uncertainty assessment of entropy production. Measurement uncertainties involve total bias, elementary bias contributions

Table 6.4: Bias and precision Error for Case 2 (Entropy Production; $x = 0.985L, y = 0.46L$)

Variable, χ	Magnitude	ε_χ	η_χ	$\varepsilon_\chi \eta_\chi$	$\frac{\varepsilon_\chi \eta_\chi}{\Sigma \varepsilon_\chi \eta_\chi}$	$(\varepsilon_\chi \eta_\chi)^2$
$U(m/s)$	-4.56E-05	-2.06E-07	0	0	0.0	0
$V(m/s)$	-1.37E-03	-6.20E-06	0	0	0.0	0
$x(m)$	7.00E-03	0.0000001	0	0	0.0	0
$y(m)$	6.80E-03	0.0000001	0	0	0.0	0
$T(K)$	288	5	-5.00E-09	2.5016E-08	0.0	6.26E-16
$\mu(kg/ms)$	1.14E-03	0	1.27E-03	0	0.0	0
$k(W/mK)$	0.5911	0	0	0	0.0	0
$\Delta U_x(m/s)$	-2.6033E-06	2.90905E-07	0.17365	5.0515E-08	0.1	2.55E-15
$\Delta V_x(m/s)$	0.00191341	8.76872E-06	6.38156	5.5958E-05	79.6	3.13E-09
$\Delta U_y(m/s)$	-1.3016E-06	2.90905E-07	0.04341	1.2629E-08	0.0	1.59E-16
$\Delta V_y(m/s)$	-5.2065E-06	8.76872E-06	-0.34730	3.0453E-06	4.3	9.27E-12
$\Delta x(m)$	0.0000154	1.41421E-07	-79.31843	1.1217E-05	16.0	1.26E-10
$\Delta y(m)$	0.0000154	1.41421E-07	0.12109	1.7124E-08	0.0	2.93E-16
				$\sum \varepsilon_\chi \eta_\chi = 7.03\text{E-}05$		$\varepsilon = 0.000057$
						Error $= 6.1168\text{E-}04 \pm 9.34\%$

and precision errors. For laminar channel flow between parallel plates, the values of standard deviation along the centerline and near-wall region are 15% and 33%, respectively. Near the wall, a precision limit of 1.55% and total uncertainty of 1.55% are reported. For the problem of free convection in an enclosure, the measurement uncertainty of entropy production is 9.34%, based on a maximum error bound within the 95% confidence interval.

Chapter 7

Closure

7.1 Summary and Conclusions

In this thesis, a new entropy based approach for flow loss characterization was developed with a non-intrusive experimental technique and computational fluid dynamics. Unlike past methods of global loss characterization, this thesis outlined a new approach of predicting local losses of available energy. The entropy production distribution can be effectively found for any geometry representing a physical application, either numerically or experimentally. The numerical analysis used a hybrid finite element / volume method for discretization of the conservation laws as well as the Second Law of Thermodynamics. The experimental procedure combines methods of Particle Image Velocimetry and Planar Laser Induced Fluorescence for measured velocity and temperature fields.

New modelling of turbulence correlations for the entropy transport equation was outlined in this thesis. Closure of the correlations involving fluctuating temperature and entropy production was accomplished through Reynolds averaging. An alternative model, which used the Small Thermal Turbulence Assumption, was proposed for calculating the mean entropy production. With an eddy viscosity closure, the model resembles the corresponding laminar flow formulation, except for the eddy dif-

fusivity added to the effective diffusivity in the diffusion component of the entropy transport equation. Also, γk_t appears in the effective diffusivity of the positive definite entropy equation, as well as T'^2 terms. In contrast to conventional modeling of the dissipation rate equation, an alternative algebraic balance method was suggested, which involves both transport and positive definite forms of the turbulent entropy production equation.

The equivalence of the proposed local flow characterization based on flow exergy to conventional loss analysis is demonstrated in an analytical relation between head loss and exergy destruction. Available energy losses were found to be volumetric phenomena involving exergy destruction. This assertion and the formulation for mean turbulent entropy production was validated against DNS data and Darcy's friction factor. Close agreement between the two approaches suggested that the present turbulence modelling of entropy production has been formulated correctly for near-isothermal flows.

The entropy production algorithm was implemented through MatLab scripts and other externally developed C++ functions linked to a commercial software (Dantec Dynamics, FlowManager). Smoothing algorithms were applied to the mean velocity and temperature fields to mitigate against error in spatial derivatives. The rate of dissipation of turbulent kinetic energy was needed to compute losses in turbulent flows. The dissipation rate was estimated in the conversion algorithm with dimensional analysis based on equilibrium turbulence and a large eddy PIV method. The Clark gradient model and the Smagorinsky model were employed for the SGS stress.

The newly developed procedures were applied for whole-field measurements of flow irreversibility in a parallel channel and free convective heat transfer in a cavity. The channel flow experiments were carried out in a water tunnel seeded with polyamide particles. Measurements were recorded sufficiently downstream of the channel inlet

so that fully developed conditions were obtained. Measured entropy production and resulting exergy based friction factors in laminar flow showed close agreement with analytical solutions. Measured dissipation of turbulent kinetic energy in the turbulent channel flow problem also compared well with DNS solutions at $Re_\tau = 187$, but some deviation at higher Reynolds numbers were observed, due to limitations imposed by the spatial resolution of the CCD camera. Overall, the PIV based loss mapping gives correct qualitative and qualitative trends of losses in wall-bounded flows.

An experimental apparatus for free convection was constructed with water contained between differentially heated walls of a square cavity. A pulsed laser light sheet illuminates a cross-sectional plane of the cavity, so that two-dimensional profiles of velocity and temperature can be obtained. The peak value of entropy production occurs at the wall. A local maximum is measured close to the wall, due to a local velocity peak and zero spatial gradient of the streamwise velocity component. The measurement procedure and data are considered to be the first documented studies of whole-field entropy production measurement. Measurement uncertainties involve total bias, elementary bias contributions and precision errors. For laminar channel flow between parallel plates, the values of standard deviation along the centerline and near-wall region are 15% and 33%, respectively. Near the wall, a precision limit of 1.55% and total uncertainty of 1.55% were reported. For the problem of free convection in an enclosure, the measurement uncertainty of entropy production is 9.34%, based on a maximum error bound within the 95% confidence interval.

Measured entropy production is considered to have considerable practical utility as a diagnostic tool. The designer can use the entropy production map to detect locations in which entropy production is higher that its integrated value over the entire flow field, and thus assess the effect of a design change on the local and global distribution of losses. Since the local entropy production can be converted to local

loss parameters, its calculation can open the door to improved thermal and fluids system design.

7.2 Recommendations for Future Research

The following areas should be researched further.

- Multi-disciplinary Design Optimization (MDO) with the Second Law. The possibility of a systematic optimization is implied in this thesis. Since the newly developed technique can provide measured data for tracking spatial variations of friction irreversibility and local exergy losses, a numerical design procedure can be developed to find an optimal configuration. Iterative changes to a given profile, using an objective function based on entropy production, can be utilized until the optimum is achieved.

- Heat transfer irreversibility measurement. Attention was focussed on entropy production due to fluid friction in this thesis. The measurement procedure could be developed in a general context to fully include heat transfer irreversibilities. This will require an optimized PLIF or a more precise interferometric measurement technique.

- Entropy based loss prediction in turbulent and external flows. Local losses have been successfully characterized in a wall-bounded laminar flow (channel flow). The implementation of the conversion algorithm to loss prediction in turbulent internal flows and drag prediction in external flows will further demonstrate the applicability of the Second Law tool for loss analysis.

- Numerical turbulent dissipation modeling using the Second Law. In contrast to conventional dissipation of turbulent kinetic energy modeling, this thesis sug-

gested an alternative method based on combined transport and positive definite forms of the entropy production equation. Additional validation studies would yield useful benefits in subsequent modeling of turbulent entropy transport.

Bibliography

[1] Naterer, G. F., *Heat Transfer in Single and Multiphase Systems*, CRC Press, Boca Raton, FL, Boca Raton, 2002.

[2] Bejan, A., *Entropy Generation Minimization: The Method of Thermodynamic Optimization of Finite-Time Systems and Finite-Time Processes*, CRC Press, Inc., Boca Raton, Florida, 1996.

[3] Camberos, J. A., "Revised Interpretation of Work Potential in Thermophysical Processes," *AIAA Journal of Thermophysics and Heat Transfer*, Vol. 14, No. 2, 2000, pp. 177–185.

[4] Roth, B. and Mavris, D., "A Method for Propulsion Technology Impact Evaluation Via Thermodynamic Work Potential," *8th AIAA / USAF / NASA/ ISSMO Symposium on Multidisciplinary Analysis and Optimization*, Vol. AIAA Paper 2000-4854, Long Beach, CA, 2000.

[5] Moorhouse, D. J. and Suchomel, C. F., "Exergy methods Applied to the Hypersonic Vehicle Challenge," *32nd AIAA Plasmadynamics and laser Conference, 4th Weakly Ionized Gases Workshops*, Vol. AIAA paper 2001-3063, AIAA, Anaheim, CA, 2001.

[6] Azar, K. and Russell, E. T., "Effect of Component Layout and Geometry on the Flow Distribution in Electronics Circuit Packs," *ASME Journal of Electronic Packaging*, Vol. 113, 1991, pp. 50–57.

[7] Bejan, A. and Ledezma, G. A., "Thermodynamic Optimization of Cooling Techniques for Electronic Packages," *International Journal of Heat and Mass Transfer*, Vol. 39, No. 6, 1996, pp. 1213–1221.

[8] Landauer, R., "Irreversibility and Heat Generation in the Computing Process," *IBM Journal*, 1961, pp. 183–191.

[9] Bejan, A., *Advanced Engineering Thermodynamics*, John Willey and Son, Inc., USA, 2nd ed., 1997.

[10] Rosen, M. A. and Dincer, I., "Effect of Varying Dead-State Properties on Energy and Exergy Analyses of Thermal Systems," *International Journal of Thermal Sciences*, Vol. 43, No. 2, 2004, pp. 121–133.

[11] Dincer, I. and Sahin, A. Z., "A New Model for Thermodynamic Analysis of a Drying Process," *International Journal of Heat and Mass Transfer*, Vol. 47, No. 4, 2004, pp. 645–652.

[12] Poulikakos, D. and Bejan, A., "A Fin Geometry for Minimum Entropy Generation in Forced Convection," *Transactions of the ASME*, Vol. 104, 1982, pp. 616–623.

[13] Zubair, S. M., Kadaba, P. V., and Evans, R. B., "Second-Law-Based Thermoeconomic Optimization of Two-phase Heat Exchangers," *Journal of Heat Transfer*, Vol. 109, 1987, pp. 287–294.

[14] Adeyinka, O. B. and Naterer, G. F., "Optimization Correlation For Entropy Production and Energy Availability in Film Condensation Heat Transfer," *International Communication in Heat and Mass Transfer*, Vol. 31, No. 4, 2004, pp. 513–524.

[15] Sciubba, E., "Calculating Entropy with CFD," *Mech. Eng.*, Vol. 119, No. 10, 1997, pp. 86–88.

[16] Natalini, G. and Sciubba, E., "Minimization of the Local Rates of Entropy Production in the Design of Air-Cooled Gas Turbine Blades," *ASME Journal of Engineering for Gas Turbine and Power*, Vol. 121, 1999, pp. 466 – 475.

[17] Kresta, S. M. and Wood, P. E., "The Flow Field Produced by a Pitched Blade Turbine: characterization of the Turbulence and Estimation of the Dissipation Rate," *Chemical Engineering Science*, Vol. 48, 1993, pp. 1761–1774.

[18] Baytas, A. C., "Entropy Generation for Natural Convection in an Inclined Porous Cavity," *International Journal Heat and Mass Transfer*, Vol. 43, 2000, pp. 2089–2099.

[19] Cheng, C. H., Ma, W. P., and Huang, W. H., "Numerical Predictions of Entropy Generation for Mixed Convective Flows in a Vertical Channel with Transverse Fin Arrays," *International Journal of Heat and Mass Transfer*, Vol. 21, 1994, pp. 519–530.

[20] Sahin, A. Z., "Entropy Generation in Turbulent Liquid Flow Through a Smooth Duct Subjected to Constant Wall Temperature," *Int. Journal of Heat and Mass Transfer*, Vol. 43, 2000, pp. 1469–1478.

[21] Sahin, A. Z., "Entropy Generation and Pumping Power in a Turbulent Fluid Flow Through a Smooth Pipe Subjected to Constant Heat Flux," *Exergy, an International Journal*, Vol. 2, 2002, pp. 314–321.

[22] Demirel, Y., "Irreversibility Profiles in a Circular Couette Flow of Temperature Dependence Materials," *International Communications in Heat Mass Transfer*, Vol. 26, 1999, pp. 75–83.

[23] Mahmud, S. and Fraser, R. A., "Analysis of Entropy Generation Inside Concentric Cylinder Annuli With Relative Rotation," *International Journal of Thermal Sciences*, Vol. 42, 2002, pp. 513–521.

[24] Adeyinka, O. B. and Naterer, G. F., "Entropy Based Metric for Component Level Energy Management: Application to Diffuser Performance," *International Journal of Energy Research*, 2004 (to appear).

[25] Moore, J. and Moore, J. G., "Entropy Production Rates from Viscous Flow Calculations Part I-A Turbulent Boundary Layer Flow," *ASME Gas Turbine Conference*, Vol. ASME Paper 83-GT-70, Phoenix, 1983.

[26] Moore, J. and Moore, J. G., "Entropy Production Rates from Viscous Flow Calculations Part II - Flow in a Rectangular Elbow," *ASME Gas Turbine Conference*, ASME Paper 83-GT-71, Phoenix, 1983.

[27] Cervantes, J. and Soloris, F., "Entropy Generation in a Plane Oscillating Jet," *International Journal Heat and Mass Transfer*, Vol. 45, 2002, pp. 3125–3129.

[28] Drost, M. K. and White, M. D., "Numerical Predictions of Local Entropy Generation in an Impinging Jet," *ASME Journal of Heat Transfer*, Vol. 113, 1991, pp. 823 – 829.

[29] Kramer-Bevan, J. S., *A Tool for Analysing Fluid Flow Losses*, M.sc., University of Waterloo, 1992.

[30] Naterer, G. F., "Constructing an Entropy-Stable Upwind Scheme for Compressible Fluid Flow Computations," *AIAA Journal*, Vol. 37, No. 3, 1999, pp. 303–312.

[31] Cox, R. A. and Argrow, B. M., "Entropy Production in Finite-Difference Schemes," *AIAA Journal*, Vol. 31, No. 1, 1992, pp. 210–211.

[32] Adeyinka, O. B., *Entropy and Second Law Optimization in Computational Thermofluids with Laser Based Measurements.*, M.sc. thesis, University of Manitoba, 2002.

[33] Hughes, T. J. R., Mallet, M., and Franca, L. P., "Entropy Stable Finite Element Methods for Compressible Fluids: Application to High Mach Number Flows with Shocks," *Finite Element Methods for Nonlinear Problem Europe-US Symposium*, Trondheim, Norway, 1985, pp. 762–773.

[34] Jansen, K. E., *The Role of Entropy in Turbulence and Stabilized Finite Element Methods*, Ph. d., Stanford University, CA, USA, 1993.

[35] Hauke, G. A., *A Unified Approach to Compressible and Incompressible Flows and a New Entropy-Consistent Formulation for the K-Epsilon Model*, Ph.d., Stanford University, 1995.

[36] Naterer, G. F. and Camberos, J. A., "Entropy and the Second Law in Fluid Flow and Heat Transfer Simulation," *AIAA Journal of Thermophysics and Heat Transfer*, Vol. 17, No. 3, 2003, pp. 360–371.

[37] Adeyinka, O. B. and Naterer, G. F., "Predictive Entropy Production and Measurement with Particle Image Velocimetry (PIV) for Recirculating Flows," *AIAA*

/ *ASME 8th Joint Thermophysics and Heat Transfer Conference*, Vol. AIAA Paper-2002-3090, St. Louis, Missouri, USA, 2002.

[38] Meyer, K. E., Larsen, P. S., Guillard, F., and Westergaard, C. H., "Temperature and Velocity Fields in Natural Convection by PIV and LIF," *11th International Symposium on Application of Laser Techniques to Fluid Mechanics*, Lisbon, Portugal, 2002.

[39] Coolen, M. C. J., Kieft, R. N., Rindt, C. C. M., and Van Steenhoven, A. A., "Application of 2-D LIF Temperature Measurement in Water using a Nd:YAG Laser," *Experiments in Fluids*, Vol. 27, 1999, pp. 420 – 426.

[40] Saarenrinne, P. and Piirto, M., "Turbulent kinetic energy dissipation rate estimation from PIV velocity vector fields," *Experiments in Fluids*, Vol. 29, No. 7, 2000, pp. S300 – S307.

[41] Sheng, J., Meng, H., and Fox, R., "A Large Eddy PIV Method for Turbulence Dissipation Rate Estimation," *Chemical Engineering Science*, Vol. 55, 2000, pp. 4423–4434.

[42] Hanjalic, K. and Jakirilic, S., "Second-moment Turbulence Closure Modelling," *Closure Strategies for Turbulent and Transitional Flows , Part A*, edited by B. Launder and N. Sandham, Cambridge University Press, 2002.

[43] Tennekes, H. and Lumley, J. L., *A First Course in Turbulence*, MIT Press, 1972.

[44] Willert, C. E. and Gharib, M., "Digital Particle Image Velocimetry," *Experiments in Fluids*, Vol. 10, 1991, pp. 181–193.

[45] Westerweel, J., "Fundamentals of Digital Particle Image Velocimetry," *Measurement Science and Technology*, Vol. 8, 1997, pp. 1379 – 1392.

[46] Adrian, R. J., "Particle-Imaging Techniques for Experimental Fluid Mechanics," *Annual Review of Fluid Mechanics*, Vol. 23, 1991, pp. 261–304.

[47] *FlowMap Particle Image Velocimetry Instrumentation: Installation and User Guide*, Dantec Dynamics, Demark, 1998.

[48] Adrian, R. J., "Dynamic Ranges of Velocity and Spatial Resolution of Particle Image Velocimetry," *Measurement Science and Technology*, Vol. 8, 1997, pp. 1393 – 1398.

[49] Hinze, J. O., *Turbulence*, McGraw-Hill, 2nd ed., 1975.

[50] Batchelor, G. K., *The theory of homogeneous turbulence*, Cambridge University Press, 1982.

[51] Smagorinsky, J., "General Circulation Experiments with the Primitive Equations: I. The Basic Equations," *Monthly Weather Review*, Vol. 91, 1963, pp. 99 –164.

[52] Germano, M., Piomelli, U., Moin, P., and Cabot, W. H., "A Dynamic Subgrid-scale Eddy Viscosity Model." *Physics of Fluids A*, Vol. 3, 1991, pp. 1760–1765.

[53] Lilly, D. K., "A Proposed Modification of the Germano Subgrid-scale Closure Method." *Physics of Fluids A*, Vol. 4, 1992, pp. 633–635.

[54] Meneveau, c., Lund, T., and Cabot, W. H., "A Lagrangian Dynamic Subgrid-scale Model of Turbulence," *Journal of Fluid Mechanics*, Vol. 319, 1996, pp. 353–385.

[55] Bardina, J., Ferziger, J. H., and Reynolds, W. C., "Improved Subgrid-Scale Models for Large-Eddy Simulation," *AIAA Paper 80 - 1357*, 1980, pp. 9 –.

[56] Clark, R. A., Ferziger, J. H., and Reynolds, W. C., "Evaluation of Subgrid-scale Models using an Accurately Simulated Turbulent Flow." *Journal of Fluid Mechanics*, Vol. 91, 1979, pp. 1–16.

[57] Métais, O. and Lesieur, M., "Spectral Large-eddy Simulation of Isotropic and Stably Stratified Turbulence." *Journal of Fluid Mechanics*, Vol. 239, No. 157-194, 1992.

[58] Mason, P., "Large-eddy Simulation of the Convective Atmospheric Boundary Layer," *Journal of Atmospheric Science*, Vol. 46, 1989, pp. 1492–1516.

[59] Sullivan, P. P., McWilliams, J., and Moeng, C.-H., "A Subgrid-scale Model for Large-Eddy Simulation of Planetary Boundary-Layer Flows," *Boundary Layer Meteorology*, Vol. 71, 1994, pp. 247–276.

[60] Saarenrinne, P., Piirto, M., and Eloranta, H., "Experiences of Turbulence Measurement with PIV," *Measurement Science and Technology*, Vol. 12, 2001, pp. 1904 – 1910, 4.

[61] Browne, L. W. B., Antonia, R. A., and Shah, D. A., "Turbulent Energy Dissipation in a Wake," *Journal of Fluid Mechanics*, Vol. 179, 1987, pp. 307 – 326.

[62] Elsner, J. and Elsner, W., "On the measurement of turbulence energy dissipation," *Measurement Science and Technology*, Vol. 7, No. 10, 1996, pp. 1334 – 1348.

[63] Piirto, M., Saarenrinne, P., Eloranta, H., and Karvinen, R., "Measuring turbulence energy with PIV in a backward-facing step flow," *Experiments in Fluids*, Vol. 35, No. 3, 2003, pp. 219 – 236.

[64] Kit, E., Tsinober, A., and Dracos, T., "Velocity Gradients in a Turbulent Jet Flow," *Applied Scientific Research (The Hague)*, Vol. 51, No. 1-2, 1993, pp. 185 – 190.

[65] Kresta, S., "Turbulence in stirred tanks: Anisotropic, approximate, and applied," *Canadian Journal of Chemical Engineering*, Vol. 76, No. 3, 1998, pp. 563 – 575.

[66] Turan, O. and Azad, R., "Effect of hot-wire probe defects on a new method of evaluating turbulence dissipation," *Journal of Physics E: Scientific Instruments*, Vol. 22, No. 4, 1989, pp. 254 – 261.

[67] Liu, Z. C., Landreth, C. C., Adrain, R. J., and Hanratty, T. J., "High Resolution Measurement of Turbulent Structure in a Channel with Particle Image velocimetry," *Experiments in Fluids*, Vol. 10, 1991, pp. 301–312.

[68] Kim, J., Moin, P., and Moser, R., "Turbulence Statistics in Fully Developed Channel Flow at Low Reynolds Number," *Journal of Fluid Mechanics*, Vol. 177, 1987, pp. 133–166.

[69] White, F. M., *Viscous Fluid Flow*, McGraw Hill, Inc., 2nd ed., 1991.

[70] Clark, J., "Study of incompressible turbulent boundary layers in channel flow," *ASME Meeting FE-26, May 6-9 1968*, American Society of Mechanical Engineers – Papers, American Society of Mechanical Engineers (ASME), New York, NY, United States, 1968, p. 13.

[71] Johansson, A. V. and Alfredsson, P. H., "On the Structure of Turbulent Channel Flow," *Journal of Fluid Mechanics*, Vol. 122, 1982, pp. 295 – 314.

[72] Eckelmann, H., "Structure of the Viscous Sublayer and the Adjacent Wall Region in a Turbulent Channel Flow," *Journal of Fluid Mechanics*, Vol. 65, No. Part 3, 1974, pp. 439 – 459.

[73] Zhou, J., Meinhart, C., Balachandar, S., and Adrian, R., "Formation of coherent hairpin packets in wall turbulence Self-Sustaining Mechanisms of Wall Turbulence," Advances in Fluid Mechanics, Computational Mechanics Inc, Billerica, MA, USA, 15th ed., 1997, pp. 109–134.

[74] Moser, R. D., Kim, J., and Mansour, N. N., "Direct Numerical Simulation of Turbulent Flow up to $Re_\tau = 590$," *Physics of Fluids*, Vol. 11, No. 4, 1999, pp. 943–945.

[75] Kuroda, A., Kasagi, N., and Hirata, M., "A Direct Numerical Simulation of the Fully Developed Turbulent Channel Flow," *International Symposium on Computational Fluid Dynamics*, Nagoya, Japan, 1989, pp. 1174 – 1179.

[76] De Vahl Davis, G., "Natural Convection of Air in a Square Cavity: A Benchmark Solution," *International Journal of Numerical Methods in Fluids*, Vol. 3, 1983, pp. 249–264.

[77] Hortmann, M., Peric, M., and Scheuerer, G., "Finite Volume Multigrid Predictions for Laminar Natural Convection: Benchmark Solution," *International Journal of Numerical Methods in Fluids*, Vol. 11, 1990, pp. 189–207.

[78] Lightstone, M. F. and Collins, W. M., "Simulation of Natural Convection of Air in a Square Cavity Using the GOTHIC Thermohydraulic Code," *Proceedings of the CNA / CNS Annual Conference*, Montreal, Canada, 1994.

[79] Ismail, K. A. R. and Scalon, V. L., "A Finite Element Free Convection Model for the Side Wall Heated Cavity," *International Journal of Heat and Mass Transfer*, Vol. 43, 2000, pp. 1373 – 1389.

[80] Baytas, A. C., "Optimization in an Enclosure for Minimum Entropy Generation in Natural Convection," *Journal of Non-Equilib. Thermodynamics*, Vol. 22, No. 2, 1997, pp. 145–155.

[81] Megherbi, M., Abbassi, H., and Brahim, A. B., "Entropy Generation at the Onset of Natural Convection," *International Journal Heat and Mass Transfer*, Vol. 46, No. 18, 2003, pp. 3441–3450.

[82] Abu-Hijleh, B. A. and Heilen, W. N., "Entropy Generation Due to Laminar Natural Convection Over a Heated Rotating Cylinder," *International Journal Heat and Mass Transfer*, Vol. 42, 1999, pp. 4225–4233.

[83] Mallinson, G. D. and De Vahl Davis, G., "Three Dimensional Natural Convection in a Box: A Numerical Study," *Journal of Fluid Mechanics*, Vol. 83, No. 1, 1977, pp. 1–31.

[84] Adeyinka, O. B. and Naterer, G. F., "Apparent Entropy Difference with Heat and Fluid Flow Irreversibilities," *Numerical Heat Transfer B*, Vol. 42, 2002, pp. 411–436.

[85] Hamady, F. J. and Lloyd, J. R., "Study of Local Convection Heat Transfer in an Inclined Enclosure," *Int. Journal of Heat and Mass Transfer*, Vol. 32, No. 9, 1989, pp. 1697–1708.

[86] Luff, J. D., Drouillard, T., Rompage, A. M., Linne, M. A., and Hertzberg, J. R., "Experimental Uncertainties Associated with Particle Image Velocimetry (PIV) Based Vorticity Algorithms," *Experiments in Fluids*, Vol. 26, 1999, pp. 36–54.

[87] Coleman, H. W. and Steele, W. G., *Experimentation and Uncertainty Analysis for Engineers*, Wiley, New York, 1989.

[88] Moffat, R. J., "Describing the Uncertainties in Experimental Results," *Experimental Thermal and Fluid Science*, Vol. 1, 1988, pp. 3–17.

[89] Gui, L., Longo, J., and Stern, F., "Towing Tank PIV Measurement System, Data and Uncertainty Assessment for DTMB Model 5512," *Experiments in Fluids*, Vol. 31, 2001, pp. 336–346.

[90] Alekseeva, A. K. and Navon, M. I., "On Estimation of Temperature Uncertainty Using the Second Order Adjoint Algorithm," *International Journal of Computational Fluid Dynamics*, Vol. 16, No. 2, 2002, pp. 113–117.

[91] Pelletier, D., Turgeon, E., Lacasse, D., and Borggaard, J., "Adaptivity, Sensitivity and Uncertainty: Toward Standards of Good Practice in Computational Fluid Dynasmics," *AIAA Journal*, Vol. 41, No. 10, 2003, pp. 1925–1933.

[92] Alekseeva, A. K. and Navon, I. M., "Calculation of Uncertainty Propagation Using Adjoint Equations," *International Journal of Computational Fluid Dynamics*, Vol. 17, No. 4, 2003, pp. 283–288.

[93] Kline, S. J. and McClintock, F. A., "Describing Uncertainties in Single-Sample Experiments,," *Mechanical Engineering*, Vol. 75, 1953, pp. 3–8.

[94] Lassahn, G. D., "Uncertainty Definition," *ASME Journal of Fluids Engineering*, Vol. 107, 1985, pp. 179.

[95] Moffat, R. J., "Contributions to the Theory of Single-Sample Uncertainty Analysis," *ASME Journal of Fluids Engineering*, Vol. 104, 1982, pp. 250–260.

[96] Kline, S. J., "The Purpose of Uncertainty Analysis," *ASME Journal of Fluids Engineering*, Vol. 107, No. 153-160, 1985.

[97] AIAA-Standard-S017-1995, *Assessment of Experimental Uncertainty with Application to Wind Tunnel Testing*, American Institute of Aeronautics and Astronautics, Washington, DC, 1995.

[98] Coleman, H. W. and Steele, W. G., "Engineering Application of Experimental Uncertainty Analysis," *AIAA Journal*, Vol. 33, 1995, pp. 1888–1896.

Appendix A

Derivation of Linear Eddy Viscosity Closure

The fluctuating component of the specific entropy is given by

$$s' \approx c_v \frac{T'}{\bar{T}} - R\frac{\rho'}{\bar{\rho}} \tag{A.1}$$

By the Reynolds analogy,

$$\overline{T'u'} = -\frac{k_t}{\rho c_p}\frac{\partial \bar{T}}{\partial x_i} \tag{A.2}$$

Also, based on the STT Assumption,

$$\frac{\partial \bar{s}}{\partial x_i} = \frac{c_v}{\bar{T}}\frac{\partial \bar{T}}{\partial x_i} \tag{A.3}$$

Using Eqs. (A.1) - (A.3) in the first term on the right side of Eq. (2.33) gives

$$\rho\overline{T'u_i'}\frac{\partial \bar{s}}{\partial x_i} = -\gamma k_t \left(\frac{\partial \bar{T}}{\partial x_i}\right)^2 \tag{A.4}$$

where $\gamma = c_v/c_p = 1$ for incompressible fluids.

The second term in Eq. (2.33), under the STT Assumption, becomes

$$T'\frac{\partial s'}{\partial x_i} \approx T'\frac{\partial}{\partial x_i}\left(c_v\frac{T'}{\bar{T}}\right) = c_v\left(T'\right)^2\frac{\partial}{\partial x_i}\left(\frac{1}{\bar{T}}\right) + \frac{c_v}{\bar{T}}\left[T'\frac{\partial T'}{\partial x_i}\right] \tag{A.5}$$

After time averaging,

$$\overline{T'\frac{\partial s'}{\partial x_i}} \approx c_v\overline{\left(T'\right)^2}\frac{\partial}{\partial x_i}\left(\frac{1}{\bar{T}}\right) + \frac{c_v}{\bar{T}}\left[\frac{1}{2}\frac{\overline{\partial (T')^2}}{\partial x_i}\right] \tag{A.6}$$

The third term in Eq. (2.33), under the STT Assumption, becomes

$$T'\frac{\partial}{\partial x_i}(\rho u_i' s') \approx T'\frac{\partial}{\partial x_i}\left(\rho\frac{c_v}{\bar{T}}T'u_i'\right) = \rho c_v u_i'\left(T'\right)^2\frac{\partial}{\partial x_i}\left(\frac{1}{\bar{T}}\right) + \rho\frac{c_v}{\bar{T}}T'\frac{\partial}{\partial x_i}(T'u_i') \quad \text{(A.7)}$$

The last term in Eq. (A.7) can be written as

$$T'\frac{\partial}{\partial x_i}(T'u_i') = T'\left[T'\frac{\partial u_i'}{\partial x_i} + u_i'\frac{\partial T'}{\partial x_i}\right] \quad \text{(A.8)}$$

where $\overline{T'(\partial u_i'/\partial x_i)} = 0$ due to the continuity equation. The time averaged form of Eq. (A.8) becomes

$$\overline{T'\frac{\partial}{\partial x_i}(T'u_i')} = \frac{1}{2}\overline{\frac{\partial}{\partial x_i}\left(u_i'T'^2\right)} \quad \text{(A.9)}$$

Substituting this result back into Eq. (A.7) gives

$$\overline{T'\frac{\partial}{\partial x_i}(\rho u_i' s')} \approx \rho c_v\overline{u_i'\left(T'\right)^2}\frac{\partial}{\partial x_i}\left(\frac{1}{\bar{T}}\right) + \frac{\rho c_v}{2\bar{T}}\overline{\left(u_i'T'^2\right)} \quad \text{(A.10)}$$

The final form of the $\overline{T'\dot{P}_s'}$ correlation, under the Small Thermal Turbulence Assumption, becomes

$$\begin{aligned}\overline{T'\dot{P}_s'} &= -\gamma k_t\left(\frac{\partial\bar{T}}{\partial x_i}\right)^2 + \rho c_v\frac{\partial}{\partial x_i}\left(\frac{\overline{u_i'T'^2}}{\bar{T}}\right) + \rho c_v\bar{u}_i\frac{\partial}{\partial x_i}\left(\frac{\overline{T'^2}}{\bar{T}}\right) \\ &- \frac{\rho c_v}{2\bar{T}}\frac{\partial\left(\overline{u_i'T'^2}\right)}{\partial x_i} - \frac{\rho c_v\bar{u}_i}{2\bar{T}}\frac{\partial\left(\overline{T'^2}\right)}{\partial x_i}\end{aligned} \quad \text{(A.11)}$$

Equations (2.28), (2.39) and (A.11) can be combined under the STT Assumption. After several algebraic manipulations,

$$\begin{aligned}\frac{\partial}{\partial t}(\rho\bar{s}) &+ \frac{\partial}{\partial x_i}\left[\rho\bar{u}_i\bar{s} - \frac{1}{\bar{T}}\left(\frac{c_v\mu_t}{Pr_t} + k\right)\frac{\partial\bar{T}}{\partial x_i}\right] = \frac{1}{\bar{T}^2}\left[\left(k+\gamma k_t\right)\left(\frac{\partial\bar{T}}{\partial x_i}\right)^2\right] + \frac{\bar{\tau}_{ij}}{\bar{T}}\frac{\partial\bar{u}_i}{\partial x_j} + \\ \frac{\tilde{\epsilon}}{\bar{T}} &+ \left\{k\left(\frac{\partial T'}{\partial x_i}\right)^2 + \frac{k}{2}\frac{\partial}{\partial x_i}\left(\frac{1}{\bar{T}}\right)\frac{\partial}{\partial x_i}\overline{\left(T'^2\right)} - \frac{\rho c_v}{\bar{T}}\left[\frac{\partial}{\partial x_i}\left(\frac{\overline{u_i'T'^2}}{\bar{T}}\right) + \bar{u}_i\frac{\partial}{\partial x_i}\left(\frac{\overline{T'^2}}{\bar{T}}\right)\right]\right. \\ &+ \left.\frac{\rho c_v}{2\bar{T}^2}\left[\frac{\partial}{\partial x_i}\left(\overline{u_i'T'^2}\right) + \bar{u}_i\frac{\partial}{\partial x_i}\left(\overline{T'^2}\right)\right]\right\}\end{aligned} \quad \text{(A.12)}$$

This result represents the turbulent entropy transport equation, based on a linear eddy viscosity closure.